Octupole collectivity in ^{220}Rn and ^{224}Ra

Thesis submitted in accordance with the requirements of the

University of Liverpool for the degree of

Doctor in Philosophy

by

Liam Paul Gaffney

September 2012

Acknowledgments

First of all, I would like to pay my huge gratitude to Prof. Peter Butler for giving me the opportunity to work on such an exciting project. I thank him for his unquantifiable guidance and supervision during my formative years as a scientific researcher.

I follow this closely with a massive "danksche" to my friend and sensei, Dr. Marcus Scheck. I am in his debt for the knowledge, culture and beer he has handed down to me over the past 4 years. A special thanks for reading and correcting this thesis on too many occasions and for his direction throughout.

I thank Andrew Petts for getting me started in those early days, I'd have been out of my depth without his help.

Thanks must also go to the Liverpool Nuclear Physics group for putting up with me and facilitating football, intense discussions, laughs, crosswords and drinks. Most of all the drinks. Dr. Dave O'Donnell, Mark Drummond, Dr. Rob Carroll, John Revill, Joe Rees, Baha Sayğı and the rest... thank you.

It would be remiss of me not to recognise the STFC for their financial support and for allowing me the freedom to travel to so many places to conduct my research and disseminate my findings. I pay gratitude to them also for funding my long-term attachment to ISOLDE and to Dr. Janne Pakarinen and Dr. Nigel Warr for the supervision and training.

Finally, I want to give my appreciation to Jen Kenworthy for her support and understanding throughout, and especially for the KFC deliveries when I was writing up. The biggest thanks of them all is reserved for my Mum and Dad and even that isn't enough. Their unwavering support and confidence has enabled me to achieve more than they ever demanded of me.

Abstract

Collective properties of the radioactive nuclei ^{220}Rn and ^{224}Ra have been studied via Coulomb excitation of a 2.8 A.MeV radioactive ion beam (RIB) incident upon ^{60}Ni, ^{112,114}Cd and ^{120}Sn targets. The experiments took place at the REX-ISOLDE RIB facility, CERN. De-excitation γ-ray yields following multiple-step Coulomb excitation were detected in coincidence with recoiling target nuclei in the Miniball spectrometer.

For the first time, $B(E3; 3^+ \rightarrow 0^+)$ values have been directly measured with a radioactive ion beam. In the process, ^{224}Ra becomes the heaviest post-accelerated RIB to date at ISOLDE (with the possible exception of the quasi-stable ^{238}U). The measurements presented in this thesis represent a tripling of the number of nuclei around $Z \simeq 88$ and $N \simeq 134$, for which direct measurements of the octupole collectivity have been performed. The only previous measurements being for the relatively long-lived ^{226}Ra.

The γ-ray yields, in conjunction with previously measured spectroscopic data, were used to determine electromagnetic matrix elements using the least-squares search code, GOSIA. In total, nine $E1$, $E2$ and $E3$ matrix elements were measured in ^{220}Rn (plus six upper limits) and 12 (plus four upper limits) in ^{224}Ra. The measured $B(E3; 3^+ \rightarrow 0^+)$ values in ^{220}Rn and ^{224}Ra are 32$\pm$4 W.u. and 42$\pm$3 W.u., respectively. A new state has been observed at 937.8(8) keV in ^{220}Rn and is proposed to be the 2^+ member of the $K = 2$, γ-vibrational band.

The results are interpreted in terms of the collectivity and deformation, and are compared with the predictions of self-consistent mean-field theory and cluster model calculations.

Contents

List of Figures

List of Tables

Chapter 1

Introduction

The notion that collectivity due to the octupole ($\lambda = 3$) degree of freedom can occur in atomic nuclei is supported by a large base of experimental evidence and theoretical work [1]. For a long time, quadrupole ($\lambda = 2$) collectivity has been established and features such as rotational bands, described consistently by a wide variety of collective models. The introduction of an octupole degree of freedom into the Nilsson-Strutinsky model predicted a gain in binding energy of 1–2 MeV in nuclei around ^{224}Ra [2]. A systematic review recognised octupole correlations as an essential contribution to the mean field interaction just above closed shells, where (N, j, l) intruder orbitals interact strongly with the $(N-1, j-3, l-3)$ natural parity states. In these regions, when the Fermi level is situated between these orbitals, the strongest interactions occur. The corresponding particle numbers are Z or $N \simeq 34$, 56, 88 and 134.

Collective parameters, such as multipole moments, Q_λ, and transition strengths, $B(E\lambda)$, are used to describe the shape of deformed nuclei and can be directly or indirectly accessed through various experimental techniques. Measurements of these parameters in the actinide region, where correlations are expected to be strongest, are scarce due to various experimental limitations, such as the unstable nature of these nuclei. An indirect measurement of $B(E3; 3^- \rightarrow 0^+)$, for example, can be

achieved with knowledge of the lifetime of the 3^- state and the relative $E3$ decay branch to the ground state. However, since there are usually lower-lying 2^+ and 1^- states, with the exception of only ^{146}Gd and ^{208}Pb, possessing an observed first excited state of $I^\pi = 3^-$ to date, $E1$ and $E2$ transitions dominate and the $E3$ branch is almost impossible to observe. Coulomb excitation however, is able to populate the 3^- state directly from the ground state via an $E3$ transition, giving access to the all important matrix elements which define the collective parameters. The argument of whether any of these nuclei truly possess stable octupole deformation in the ground state, or whether their properties can be described as vibrational excitation, continues to rage.

Since the nuclei in the neutron-deficient actinide region are unstable, studying them via Coulomb excitation required the production of radioactive target materials until the advent of high-intensity radioactive ion beams. It was possible to measure $E3$ matrix elements in ^{226}Ra with the former technique [3] coupled with the advancement of Coulomb excitation analysis codes such as GOSIA [4]. It is clearly desirable to extend this technique and utilise the unique capability of CERN's Isotope Separator On-Line Detector (ISOLDE) to produce intense radioactive ion beams to three-fold increase our knowledge of octupole collectivity in the region of the nuclear chart, where it is expected to be strongest.

1.1 Collectivity and deformation in nuclei

When a nucleus deviates from sphericity, its surface can be parameterised in terms of spherical harmonics:

$$R(\theta,\phi) = c(\alpha_{\lambda\mu})R_0\left[1 + \sum_{\lambda=0}^{\infty}\sum_{\mu=-\lambda}^{\lambda}\alpha_{\lambda\mu}Y_{\lambda\mu}(\theta,\phi)\right]. \tag{1.1}$$

The factor $c(\alpha_{\lambda\mu})$ is required to conserve volume since the spherical harmonic $Y_{\lambda\mu}(\theta,\phi)$

does not average to zero for $0 \leq \theta < 180$ and $0 \leq \phi < 360$. Terms in $\lambda = 0, 1$ describe a shift in volume (the breathing mode) and centre of mass respectively, and therefore give no information on the nuclear shape. When assuming axial symmetry, $\mu = 0$ and Equation 1.1 can be reduced to the following:

$$R(\theta) = c(\beta_\lambda) R_0 \left[1 + \sum_{\lambda=2}^{\infty} \sqrt{\frac{2\lambda+1}{4\pi}} \beta_\lambda P_{\lambda 0}(\cos\theta) \right]. \tag{1.2}$$

The deformation parameters, β_λ, can be calculated from the intrinsic multipole moments, Q_λ, given in Equation 1.7. It is first useful to define an expression for the first-order term in an expansion of deformation co-ordinates,

$$Q_\lambda = \frac{3}{\sqrt{(2\lambda+1)\,\pi}} Z R_0^\lambda \bar{\beta}_\lambda \ , \quad \lambda \geq 2. \tag{1.3}$$

The full expansion, from two to six multipoles, can be given by the following intrinsic relations [5]:

$$\bar{\beta}_2 = \beta_2 + \sqrt{\frac{5}{\pi}} \left(\frac{2}{7}\beta_2^2 + \frac{4}{15}\beta_3^2 + \frac{20}{77}\beta_4^2 + \frac{10}{39}\beta_5^2 + \frac{98}{386}\beta_6^2 + \frac{12}{7\sqrt{5}}\beta_2\beta_4 + \frac{20}{21}\sqrt{\frac{7}{11}}\beta_3\beta_5 + \frac{30}{11}\frac{1}{\sqrt{13}}\beta_4\beta_6 \right), \tag{1.4}$$

$$\bar{\beta}_3 = \beta_3 + \frac{5}{\sqrt{4\pi}} \left(\frac{4}{\sqrt{45}}\beta_2\beta_3 + \frac{6}{11}\beta_3\beta_4 + \frac{60}{91}\sqrt{\frac{7}{11}}\beta_4\beta_5 + \frac{7}{33}\sqrt{\frac{77}{13}}\beta_5\beta_6 + \frac{10}{21}\sqrt{\frac{35}{11}}\beta_2\beta_5 + \frac{100}{33\sqrt{13}}\beta_3\beta_6 \right), \tag{1.5}$$

$$\bar{\beta}_4 = \beta_4 + \frac{6}{\sqrt{4\pi}} \left(\frac{3}{7}\beta_2^2 + \frac{3}{11}\beta_3^2 + \frac{243}{1001}\beta_4^2 + \frac{3}{13}\beta_5^2 + \frac{42}{187}\beta_6^2 + \frac{20\sqrt{5}}{77}\beta_2\beta_4 + \frac{60}{91}\sqrt{\frac{7}{11}}\beta_3\beta_5 + \frac{20}{11\sqrt{13}}\beta_4\beta_6 + \frac{15}{11}\sqrt{\frac{5}{13}}\beta_2\beta_6 \right). \tag{1.6}$$

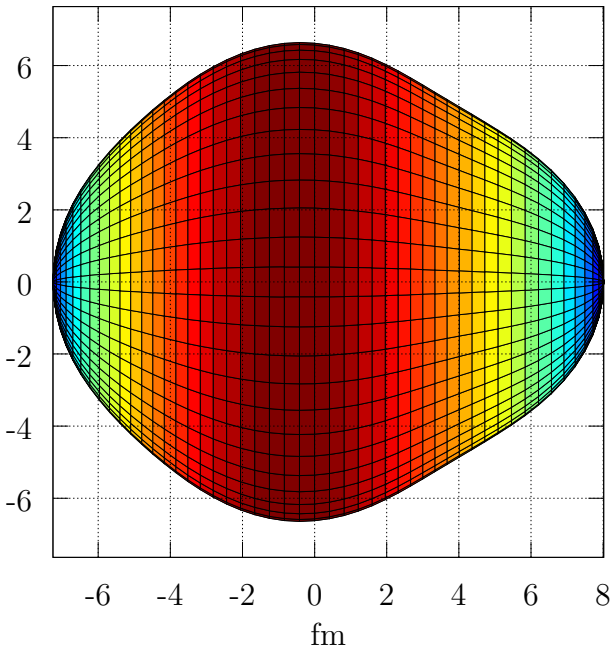

Figure 1.1: Representation of the nuclear surface of ^{226}Ra using Equation 1.2 expanded to $\lambda = 4$ and using the measured β_λ values from Ref. [3]. The colour scale represents the radius of the surface from the symmetry axis.

This relationship between multipole moments and deformation parameters is used to give a schematic representation of the shape of the nuclei studied in this thesis (see Figure 6.2), while Figure 1.1 shows ^{226}Ra, plotted using β_λ parameters calculated in the same way, from measured Q_λ values [3].

1.1.1 Rigid-rotor model

The electromagnetic matrix elements connecting an initial and final state with angular momentum, I_i and I_f, respectively, can be reduced by exploiting the Wigner-Eckart theorm, separating the projection quantum number (K) dependent components from the radial part, which contains the nuclear structure information. This leads to an expression for the reduced matrix elements which is proportional to the multipole moment (an intrinsic or transitional moment, which is distinct from the static or spectroscopic moment), Q_λ [6]:

$$\langle I_f || E\lambda || I_i \rangle = (2I_f + 1)^{\frac{1}{2}} \langle I_f 0 \lambda 0 | I_i 0 \rangle Q_\lambda a_\lambda, \tag{1.7}$$

where $a_1 = \sqrt{\frac{3}{4\pi}}$ and $a_{\lambda\geq 2} = \sqrt{\frac{2\lambda+1}{16\pi}}$ and $\langle I_i 0\lambda 0|I_f 0\rangle$ is the Clebsch-Gordan coefficient, assuming $K = 0$. This is useful in defining the strength of an electromagnetic transition between those two states, which is given by:

$$B(E\lambda; I_i \to I_f) = \frac{1}{(2I_i+1)}|\langle I_f||E\lambda||I_i\rangle|^2. \tag{1.8}$$

By substituting Eq. 1.7 into Eq. 1.8, an expression for transition strength is obtained in terms of the intrinsic multipole moment.

$$B(E\lambda; I_i \to I_f) = \frac{(2I_f+1)}{(2I_i+1)}\langle I_f 0\lambda 0|I_i 0\rangle^2 Q_\lambda^2 a_\lambda^2. \tag{1.9}$$

Under the assumption that all states in a band have the same intrinsic structure, i.e. same intrinsic matrix element or multipole moment, $B(E\lambda)$ values can be determined as spin increases within a band. Two simple indicators of nuclei which behave like a rigid rotor, are the ratios of the energies of the first two excited states, usually $E_{4/2}$ in even-even nuclei, and the strengths of the two lowest $E2$ transitions in the ground band, usually $B_{4/2}$:

$$E_{4/2} = \frac{E\,(4^+)}{E\,(2^+)} = 3.33, \tag{1.10}$$

$$B_{4/2} = \frac{B(E2; 4^+ \to 2^+)}{B(E2; 2^+ \to 0^+)} = 1.43. \tag{1.11}$$

For purely vibrational nuclei, the energy of the 4^+ state is approximately twice that of of the 2^+ state, i.e. $E_{4/2} \approx 2$, while $B_{4/2}$ also tends towards a value of 2.

1.2 Reflection-Asymmetric Nuclei

The very first observation of low-lying negative-parity states in alpha spectroscopy [7, 8] led to the suggestion that they have the same intrinsic structure as the ground state and a K quantum number of 0 [9]. It was 25 years before this was associated with a possible stable octupole deformation in the ground state of these nuclei [10–13] and predictions of their properties began.

All of the nuclei described are *axially* symmetric with respect to the longest axis and the lowest configuration of the even-even nuclei have a K quantum number of 0. However, the parity of some low-lying excitations is negative, implying that such a state is not symmetric with respect to reflection. The implication of this reflection asymmetry is presented in Figure 1.2 for three different assumed potentials with respect to the octupole deformation parameter, β_3. The first (left-most panel) of these represents a vibration about a zero octupole deformation, while the other extreme (right-most panel), is the ideal case in which an infinite barrier exists between degenerate, deformed minima, and a rigid octupole deformation ensues. In nature, this scenario is never reached in a true, complex, many-body quantum system, where dynamical fluctuations smear the phase transition to deformation, and the centre panel represents the most realistic, octupole soft, deformation. The barrier height shown in the centre panel of Fig. 1.2 is still relatively small, even in cases presented as the strongest candidates for a stable octupole deformation, i.e. the actinide nuclei around $A = 224$ [13].

On a microscopic level, octupole correlations arise through a parity-breaking interaction between intruder orbitals, with the quantum numbers (N, j, l) and $(N-1, j-3, l-3)$ natural parity states, leading to a tendency for the strongest correlations to occur just above closed shells, namely at particle numbers Z or $N \simeq 34$, 56, 88 and 134. The largest interaction comes when the energy difference between the interacting states is minimised and the density of interacting states is

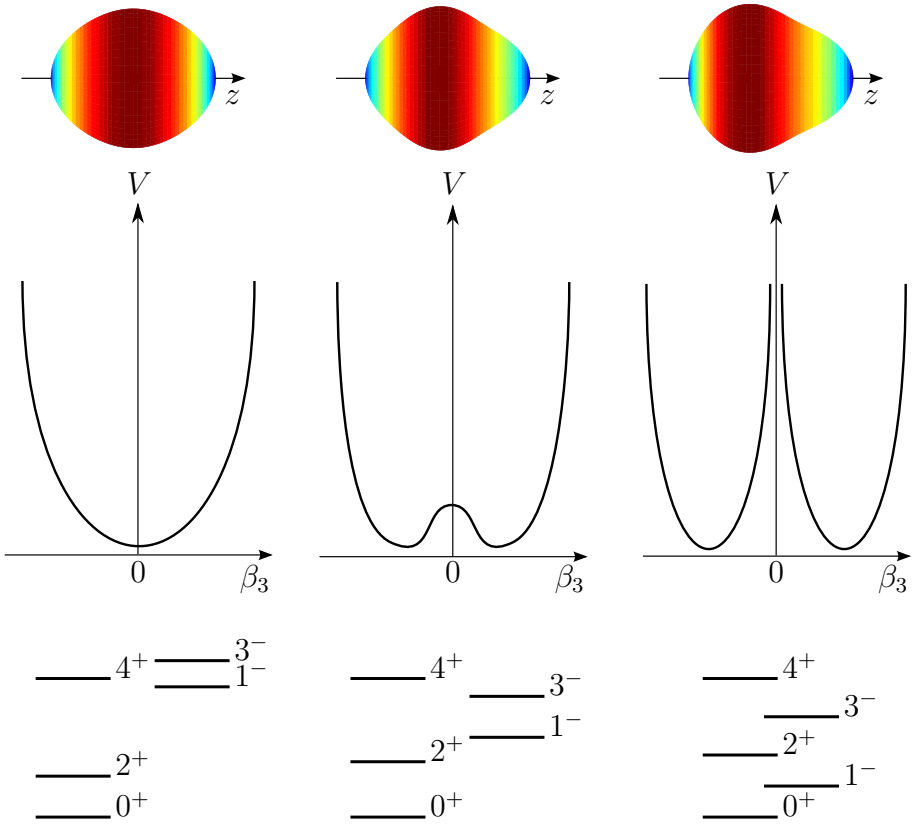

Figure 1.2: Nuclear potentials as a function of the octupole deformation parameter, β_3, for (left to right) a quadrupole deformed ($\beta_2 \neq 0$) nucleus which is octupole-vibrational with an average deformation of $\bar{\beta}_3 = 0$, an intermediate case with a small potential barrier separating two degenerate, deformed minima and an ideal case of rigid deformation. Adapted from Figure 1 of Reference [14].

at its maximum, augmenting the number and magnitude of coupling matrix elements. Both of these conditions are fulfilled with increasing mass number, leading to the combination of $Z \simeq 88$ and $N \simeq 134$ a fertile testing ground for reflection asymmetry.

In the following, the appropriate experimental observables are described in terms of reflection asymmetry and the evidence they provide in support of collective octupole excitations.

1.2.1 Energy levels

Low-lying 1^- and 3^- excited states, of collective origin, betray reflection asymmetry. Their relative excitation energy with respect to the first-excited 2^+ and 4^+ states is an indicator of the strength of the interaction and this reaches a minimum for ^{224}Ra. The comparison to the positive-parity states, coupled with the $E(3^-)$ and $E(1^-)$ difference, is also essential in quantifying the collective nature of these excitations [15]. An illustration of different level schemes for even-even nuclei is shown in Fig. 1.2. In odd-mass nuclei, the manifestation of reflection asymmetry on the energy levels, comes in the form of parity doublets [10, 16].

A first observation of odd-even staggering at high-spin in ^{218}Ra [17], and subsequently in the neighbouring even-even actinide nuclei [18–20], shows stabilisation of octupolarity [21]. Above $I = 5\hbar$, the positive- and negative-parity states begin to interleave, approaching the asymmetric rotor limit. The alignment of octupole phonons with a rotational band, also cause odd-even staggering, due to the weakening of the sphericity-driving, pairing force, caused by the Coriolis force. However, the rotational frequency follows a distinctly different path with angular momentum [22], giving a pointer to the nature of the correlations by observing high-spin states.

1.2.2 Dipole moments

An unusually large intrinsic dipole moment is observed in the "octupole" regions of the nuclear chart. Here, transitions between yrast states of opposite parity have considerable $E1$ strength. The $B(E1)$ strength is measured to be $> 10^{-4}$ single-particle units in octupole-deformed nuclei, and as high as 10^{-2} W.u. [23]. These values are orders of magnitude greater than typical values of similar transitions measured elsewhere in the nuclear chart.

It was suggested that a displacement of the centres of charge and mass [12, 24, 25]

in reflection-asymmetric nuclei would lead to an enhancement of the intrinsic dipole moment. This effect is explained by the tendency of charged particles to gather where the radius of the potential contour is smallest, i.e. at the narrow end of the "pear" shape.

Assuming an axially-symmetric system, one can express the intrinsic dipole moment as [25, 26]:

$$D_0 = e\frac{NZ}{A}\left[\langle z_{p.c.m}\rangle - \langle z_{n.c.m}\rangle\right], \tag{1.12}$$

where $z_{p.c.m}$ and $z_{n.c.m}$ represent the co-ordinates of the proton and neutron centre of mass, respectively. In reflection-asymmetric nuclei, intrinsic parity is broken and therefore $z_{p.c.m} \neq z_{n.c.m}$ leading to a non-zero dipole moment. The relative weakness of the Coulomb force to the nuclear strong force maintains a small D_0, yet large enough to allow for the experimentally observed $E1$ strengths.

However, experimental observations of relatively small $|D_0|$ values in ^{224}Ra prompted the introduction of a shell-correction term to the calculation of the intrinsic dipole moment [27]. The earlier works of Strutinsky, and Bohr and Mottelson used only a macroscopic approach and hence could not predict fluctuations in the intrinsic dipole moment for nuclei with the same shape. The microscopic part of the dipole moment, introduced by Leander *et al.* [27], has been calculated [26] to be roughly equal to the macroscopic, or liquid-drop term, and is summed either constructively or destructively,

$$D_0 = (\pm)D_0^{macro} + (\pm)D_0^{shell}. \tag{1.13}$$

The resulting dipole moment in ^{224}Ra reproduces the previously observed $B(E1)/B(E2)$ branching ratios [28, 29]. These calculations, in fact, do very well in reproducing the known systematics in the actinide, as well as the lanthanide region where the small D_0 in ^{146}Ba is also reproduced.

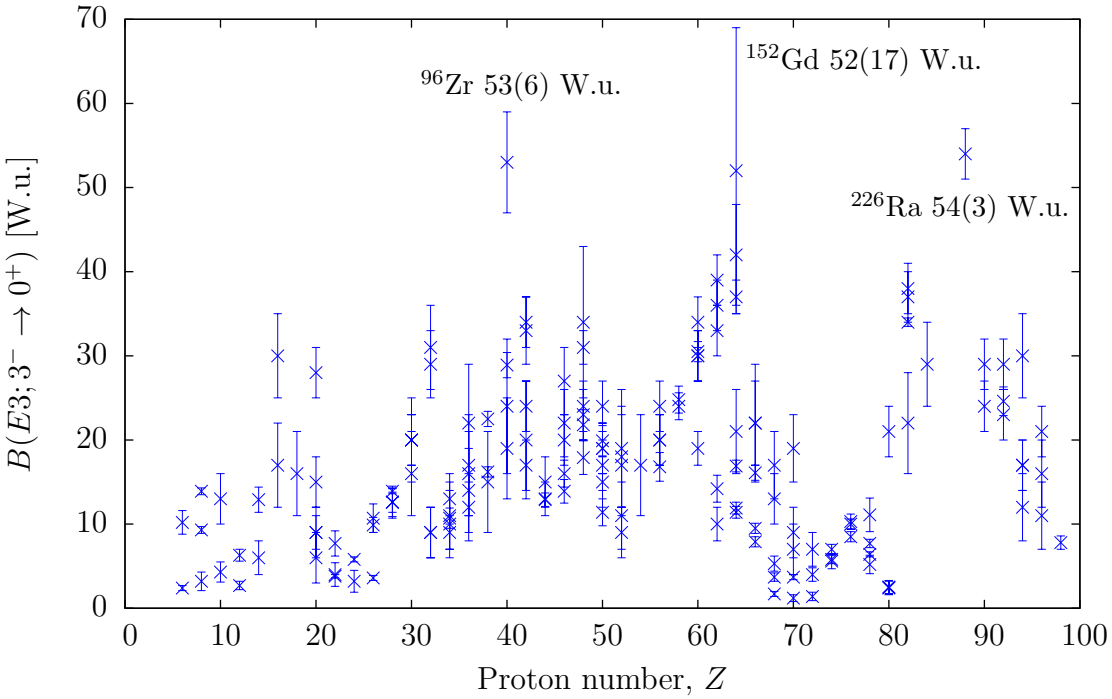

Figure 1.3: Previously measured $B(E3; 3^- \rightarrow 0^+)$ values as a function of proton number, Z. Values are calculated from tabulated data in Ref. [30].

1.2.3 E3 transition strength

The single-particle effects described for dipole moments (Section 1.2.2) do not have as strong an influence in the octupole moment, or the $E3$ matrix elements. For this reason, measurements of $E3$ matrix elements or octupole moment, Q_3 (via Equation 1.8), provide the best measure of the collective strength of the octupole correlations.

The simplest indicator one can get from these measurements, is the $B(E3; 3^- \rightarrow 0^+)$, which gives a direct measure of the collective strength of the electric-octupole transition from the ground state to the first excited 3^- state. Data throughout the nuclear chart has been plotted in Figure 1.3, as a function of proton number, Z. It is clear that, in the actinide region ($Z \sim 88$), there is a lack of measurements, attributed to the difficulty of performing such experiments, discussed at the beginning of this chapter.

A complete set of $E3$ matrix elements has the possibility to provide unambiguous information on the nature of the octupole excitations, be it rotational or vibrational. In ^{148}Nd [23, 31], the very small values for $\langle 2^+||E3||3^-\rangle$, $\langle 4^+||E3||5^-\rangle$, $\langle 1^-||E3||4^+\rangle$ and $\langle 3^-||E3||6^+\rangle$, compared to those of the stretched transitions between rotational, even-spin states and the odd-spin, vibrational states, such as $\langle 2^+||E3||5^-\rangle$, indicates a coupling of an octupole phonon to a rotational band. However in ^{226}Ra, these appear to follow more closely to the rigid rotor values [3], indicating true quadrupole-octupole deformation.

1.2.4 Further evidence

Many other theoretical and experimental evidence points to reflection-asymmetry in nuclei. Some of these are listed below, with appropriate references and will not be expanded upon further in this thesis since they aren't of relevence to it's content.

- Binding energy discrepancies [2, 12, 13].
- The decoupling parameter [32, 33].
- Magnetic moments in odd-mass nuclei [33, 34].
- Differential radii of odd-mass nuclei [35].
- Alpha decay hindrance factors [32, 36, 37].
- Exotic decay and cluster preformation [38–40].

For a comprehensive review of the subject of reflection asymmetry, see Ref. [1].

Chapter 2

Coulomb Excitation

When an atomic nucleus is excited from the ground state via the time-dependent electromagnetic field generated by a collision with another nucleus, it can be described as having undergone "Coulomb excitation". If this process is performed at energies well below the Coulomb barrier, the distance between the interacting nuclei remains much larger than the range of the nuclear force, ensuring its effect is negligible and all interactions can be treated using the well understood electromagnetic force.

As a result of this basic condition, it is possible to utilise "safe" Coulomb excitation to obtain spectroscopic properties of excited states in nuclei via the measurement of the excitation cross-sections. The observation of the level population is usually an indirect process, where the information gained is either the subsequent decay via γ-ray (or possibly even internally-converted electron [41]) emission, or the kinetic energy of the collision partners as a function of angle. The latter is limited by the intrinsic energy resolution of the experiment and is most useful for experiments utilising light projectiles (protons, α particles and light ions) or potentially light target nuclei in extremely inverse kinematics, taking advantage of a Helios-like spectrometer [42, 43].

There have been numerous review articles and books on the subject and a de-

tailed description of the technique and its theory can be found in Refs. [44–47]. Here, a brief description of the relevant theory is outlined in Section 2.1 and the Coulomb excitation analysis code, GOSIA is described in Section 2.2.

2.1 Theoretical description

Early use of Coulomb excitation relied on the validity of first- and second-order perturbation theory to describe a one-, or at most, two-step process. This relative simplicity came with the use of light-ion beams and was extensively exploited to measure collective quadrupole properties of many stable nuclei. Coulomb excitation of many states with the use of heavy ions presented a problem that became too great for the perturbation treatment, briefly described in Section 2.1.2. The complexity of multiple Coulomb excitation meant that a numerical approach had to be developed, and this is considered in Section 2.1.3. Analysis of Coulomb excitation data requires the validity of the semi-classical approximation, described in Section 2.1.1, since a full quantal calculation would be too computer intensive.

2.1.1 The Semi-Classical Approximation

The condition for "safe" Coulomb excitation can be expressed in terms of a classical picture using the distance of closest approach, b, for a head-on collision. It has been shown [47] that the nuclei should be separated by a distance of 5 fm so that nuclear interactions are conservatively below 0.1% of the total excitation. This yields an expression for the minimum distance of closest approach,

$$R_0\left(A_p^{1/3}+A_t^{1/3}\right)+5>b=\frac{Z_pZ_te^2}{E_p}, \tag{2.1}$$

where $R_0(=1.25\text{ fm})$ is the average nucleon radius and $A_{p/t}(Z_{p/t})$ are the mass(charge) numbers of the projectile (p) and target (t) nuclei and E_p is the kinetic energy of the

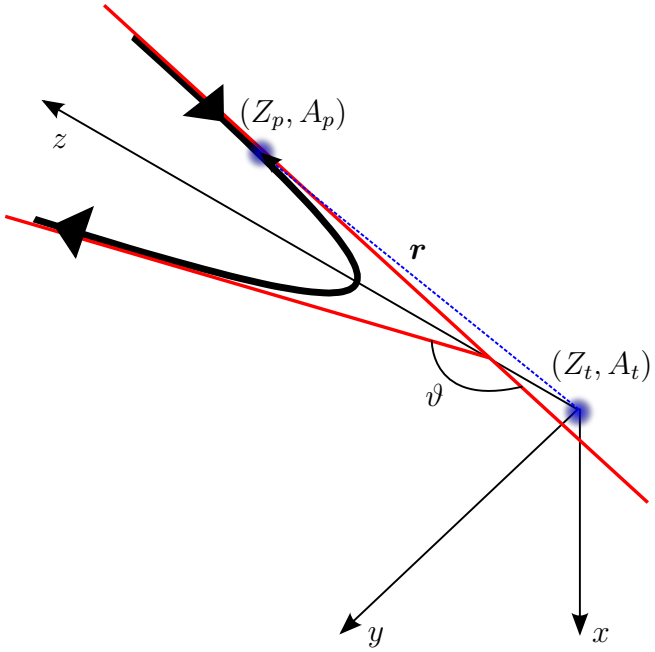

Figure 2.1: Classical depiction of the projectile orbit in the Coulomb field of the target nucleus, shown at the axes origin. The hyperbolic orbit is essentially the same as that in Rutherford scattering.

projectile. For the experiments in Chapter 4, the minimum value of b is ≈ 17 fm.

Of course, for the incoming particle to be safely treated classically, the size of the wavepacket must be much smaller than the relative distance between the two nuclei. This is achieved when the Sommerfeld parameter, η, is much greater than unity:

$$\eta = \frac{2\pi a}{\lambda} = \frac{Z_p Z_t e^2}{\hbar v_p}, \tag{2.2}$$

where $a = b/2$, half the distance of closest approach, λ is the de Broglie wavelength of the projectile with a velocity v_p and $Z_p e$ and $Z_t e$ are the respective charges of the projectile and target nuclei.

The hyperbolic trajectory depicted in Figure 2.1 is symmetric which is only true if the incoming and outgoing energies are similar, i.e. the inelastic scattering can be approximated to elastic scattering. This introduces another requirement, that the

energy transfer, ΔE, must be much smaller than the projectile energy, E_p, i.e.

$$\frac{\Delta E}{E_p} << 1. \tag{2.3}$$

In practice, symmetrisation of initial and final velocities is used to approximate this effect, but since the energy transfer is not necessarily at the point of closest approach, it cannot be accounted for fully.

For heavy projectiles at low energy, the condition $\eta \gg 1$ is fulfilled and usually (at least it is true for all cases of interest in this thesis), the excitation energy is small compared to the incoming beam energy. As a consequence of these, the semi-classical approximation is valid for the analysis of heavy ion Coulomb excitation. The Coulomb excitation cross section can, therefore, be represented as a product of the "Rutherford" cross section, σ_R, and the probability, P_n, of exciting a given state, $|n\rangle$:

$$\frac{d\sigma_n}{d\Omega} = P_n \frac{d\sigma_R}{d\Omega} \tag{2.4}$$

Here, the standard Rutherford cross-section is given by

$$\frac{d\sigma_R}{d\Omega} = \frac{a^2}{\sin^4(\vartheta/2)}, \tag{2.5}$$

where ϑ is the centre of mass scattering angle and a is half the distance of closest approach, b, defined in Equation 2.1.

2.1.2 First-order Perturbation Theory

A simple, but in the end impractical, way of viewing the excitation is to treat it as a first-order perturbation [44] to the time-dependent Schrödinger equation of the form

$$i\hbar \frac{\partial}{\partial t}|\psi(t)\rangle = H(t)|\psi(t)\rangle, \tag{2.6}$$

where the Hamiltonian, $H(t)$, can be decomposed into the three distinct parts of the electromagnetic interaction. These are the monopole-monopole term, $H_0(t)$, which treats the elastic ("Rutherford") scattering and the classical trajectory; the monopole-multipole term, $V(\boldsymbol{r}(t,\theta,\phi))$, which is responsible for the excitation of either the projectile or the target nucleus; and the multipole-multipole term, which accounts for the mutual excitation of *both* the target and projectile. Mutual excitation is small compared to the excitation of a single partner, since the individual probabilities are low, and can be neglected. Therefore, the Hamiltonian is expressed as:

$$H(\boldsymbol{r}(t)) = H_0(\boldsymbol{r}(t)) + V(\boldsymbol{r}(t)). \tag{2.7}$$

The probability in Equation 2.4 can be generalised for a multi-level system and given for each excitation path connecting an initial state $|i\rangle$ and a final state $|f\rangle$, with angular momenta $I_{i,f}$. It is the equal to the squared sum of the transition amplitudes, a_{if}, averaged over all magnetic substates, M_i and M_f,

$$P_{if} = \frac{1}{(2I_i+1)} \sum_{M_i M_f} |a_{if}|^2 . \tag{2.8}$$

The perturbation approach is valid when the electromagnetic interaction is weak compared to the total energy of the system. This condition is fulfilled for light ions exciting a single state in the target nucleus, for example. The transition amplitudes can then be defined in terms of the nuclear frequency, $\omega = \Delta E/\hbar$, which is associated to the excitation energy, $\Delta E = E_f - E_i$ and the interaction strength between the two states:

$$a_{if} = \frac{1}{\hbar} \int_{-\infty}^{\infty} \langle f|V(\boldsymbol{r}(t))|i\rangle e^{i\omega t} dt. \tag{2.9}$$

The matrix element in Equation 2.9 can be evaluated by expanding the monopole-

multipole interaction into the constituent multipole components:

$$V(\boldsymbol{r}(t)) = 4\pi Z' e \sum_{\lambda=1}^{\infty} \sum_{\mu=-\lambda}^{\lambda} \frac{1}{2\lambda+1} \frac{1}{\boldsymbol{r}(t)^{\lambda+1}} Y_{\lambda\mu}(\theta(t), \phi(t)) T(E\lambda, \mu), \tag{2.10}$$

where Z' is the atomic number of the other collision partner, $Y_{\lambda\mu}(\theta(t), \phi(t))$ are the normalised spherical harmonics with angles θ and ϕ in the centre of mass frame and $T(E\lambda, \mu)$ is the electric multipole moment of the nucleus undergoing excitation. Here, the magnetic multipoles can be neglected since magnetic excitations scale with $(v/c)^2$ and are, in the non-relativistic case, much smaller than their electric counterparts.

Substituting Equation 2.10 into Equation 2.9 the excitation amplitudes in terms of the nuclear matrix elements can be evaluated as:

$$a_{if} = \frac{4\pi Z' e}{i\hbar} \sum_{\lambda\mu} \frac{1}{2\lambda+1} \langle I_f M_f | T(E\lambda, \mu) | I_i M_i \rangle R_{\lambda,\mu}. \tag{2.11}$$

A simplification is made by representing the orbital integral by

$$R_{\lambda,\mu} = \int_{-\infty}^{\infty} e^{i\omega t} S_{\lambda,\mu}(t)\, dt = \int_{-\infty}^{\infty} e^{i\omega t} \frac{1}{\boldsymbol{r}(t)^{\lambda+1}} Y_{\lambda\mu}(\theta(t), \phi(t))\, dt \tag{2.12}$$

and the reduced matrix elements can be given using the Wigner-Eckart theorem:

$$\langle I_f M_f | T(E\lambda, \mu) | I_i M_i \rangle = (-1)^{I_f - M_f} \begin{pmatrix} I_f & \lambda & I_i \\ -M_f & \mu & M_i \end{pmatrix} \langle I_f || E\lambda || I_i \rangle. \tag{2.13}$$

These reduced, transition matrix elements are related to the transition strengths, $B(E\lambda)$, by Equation 1.8. Substituting these into Equation 2.8 and, in turn, Equation 2.4, we obtain the differential Coulomb excitation cross-section, for each electric

multipole:

$$\frac{d\sigma_{E\lambda}}{d\Omega} = \left(\frac{2\pi Z' e a}{\hbar}\right)^2 \frac{B(E\lambda)}{\sin^4\left(\frac{\vartheta}{2}\right)} \sum_{\mu} |R_{\lambda,\mu}|^2, \tag{2.14}$$

with the total differential cross-section for Coulomb excitation being the sum over all multipoles:

$$\frac{d\sigma_{CE}}{d\Omega} = \sum_{\lambda=1}^{\infty} \frac{d\sigma_{E\lambda}}{d\Omega}. \tag{2.15}$$

2.1.3 Multiple-step Coulomb Excitation

Multiple-step Coulomb excitation was outlined as early as 1956 by Alder and Winther [48] and subsequently expanded upon. A detailed outline of this early work is given in Chapter 5 of Ref. [45]. The treatment of the excitation probability can be represented as a coupled set of differential equations, where all possible paths are considered. The amplitude of an excitation to a state k, now depends on the couplings to all states n, namely the matrix elements defined in Eq. 2.13 and the energy difference between the levels, $E_k - E_n$. Of course, the probability, or more precisely, the amplitude for exciting the state n, a_n, is a crucial factor, one which further depends on couplings to all other states, including the state k,

$$\frac{da_k}{dt} = -i\frac{4\pi Z_{1,2} e}{\hbar} \sum_n a_n(t) \frac{it}{\hbar} (E_k - E_n) \sum_{\lambda\mu} (-1)^{\mu} S_{\lambda,\mu}(t) \cdot \langle I_k M_k | T(E\lambda,\mu) | I_n M_n \rangle. \tag{2.16}$$

Integration of these complex, coupled differential equations requires a numerical approach. The solution to such a problem has been refined in the coupled-channel computer code, GOSIA, described in Section 2.2. For an in-depth look at the numerical methods used, see Chapter 6 of the GOSIA manual of Ref. [49].

2.2 The Gosia Analysis Code

The analysis of multiple Coulomb excitation data was first treated numerically in the deBoer-Winther code [50]. The program treats the population of many nuclear levels via the quadrupole interaction by integrating the set of coupled differential equations, numerically. The decay is then treated and the angular distribution of the γ rays is computed. However, the input requires a certain knowledge of the quadrupole properties of the nucleus and as such, depends on the use of nuclear models. This issue and many more, such as the treatment of higher multipole orders (vital for this analysis, in particular), was overcome by Czosnyka, Cline and Wu with the introduction of the GOSIA code [4].

The GOSIA code can be used to calculate excitation cross-sections following multiple Coulomb excitation, given a set of electric and magnetic multipole matrix elements, $E1$ – $E6$, $M1$ and $M2$. For the simulation of an experiment, optimum angles and target/beam species can be found, whereas for analysis of real data, comparisons to these calculations can be used to fit the matrix elements to a number of data, in a model independent way. The most important observable is the γ-ray yield of a given transition, following the decay of a state which has been populated in the collision. This comparison is possible as the code also treats the decay of excited states governed by the very same matrix elements that determine the excitation. The assumption that these two processes are independent, and separated in time, is supported by a much faster excitation ($\sim 3 \times 10^{-21}$ s) than γ-ray de-excitation time ($\sim 10^{-14}$ – 10^{-9} s in the nuclei of interest).

Other, independent data can be included in the fit, such as lifetimes of excited states, known matrix elements, branching ratios and $E2/M1$ mixing ratios.

To calculate the cross-section and consequently the γ-ray yields, an integration of the coupled-channel differential equations is performed numerically, using a fast approximation described in the manual [49]. This calculation is done at a single

value of energy and angle and gives the "point" yields, $Y_{\text{point}}((I_i \rightarrow I_f), E, \Theta)$. Further integration over solid angle, Θ, and beam energy, E, (Equation 2.17) gives the integrated yields,

$$Y_{\text{int}}(I_i \rightarrow I_f) = \int_{E_i}^{E_f} \frac{1}{dE/dx} dE \int_{\Theta_2}^{\Theta_1} Y_{\text{point}}((I_i \rightarrow I_f), E, \Theta) \sin(\Theta) d\Theta. \tag{2.17}$$

Computing these integrations, with up to 30 meshpoints and 50 sub-meshpoints for each of dE and $d\Theta$, is time consuming, although it is performed only once as the recalculation is sped up with the use of average energy and angle values. These average point yields, $Y_{\text{ave}}(I_i \rightarrow I_f)$, are corrected by a constant factor to match the integrated yields and only if the matrix elements diverge significantly is it necessary to recalculate the correction factors with a re-integration.

The least-squares statistic used by GOSIA is very similar to χ^2 with the exception that it is normalised to the total number of data points, N, rather than the number of degrees of freedom. This is due to the difficulty in determining the degrees of freedom since each parameter and datum have hugely varying degrees of sensitivity in the fit. The statistic S, is shown, simplified:

$$S = \frac{1}{N} \left(\sum_i \frac{1}{\sigma_i^2} \left(Y_i^{\text{exp}} - Y_i^{\text{calc}} \right)^2 + \sum_j \frac{1}{\sigma_j^2} \left(d_j^{\text{exp}} - d_j^{\text{calc}} \right)^2 \right) \tag{2.18}$$

where Y represents the gamma-ray yield for each measured transition in each data set, i and the superscripts "exp" and "calc" are for the experimental and calculated values, respectively, while σ is the uncertainty on the relative yield (i.e. factoring in errors due to efficiency determination and background subtraction). The second summation is over the number of independent data, j, where d represents the value of each datum input and its associated error, σ.

2.2.1 Limitations

Comparisons to quantum-mechanical calculations in simple systems have been made to test the validity of the semi-classical approximation and overall differences in population were found to be $\approx 3\%$. However, some cancellation of this systematic effect comes from using the comparison of *relative* de-excitation γ rays in the analysis [51].

The depolarisation of the nuclear alignment due to the highly-fluctuating hyperfine fields of the recoiling atom is known as the de-orientation effect. This is responsible for the attenuation of the angular distribution of the de-excitation γ rays, something which can be corrected for when introducing attenuation coefficients, G_k. In GOSIA, the G_k coefficients are estimated using a two-state model [52, 53] and have been shown to be a good fit to experimental data [51]. In the end, this effect is not great in this experiment since the Miniball array covers a large fraction of the solid angle.

Chapter 3

Experimental setup

The Coulomb excitation of the unstable ^{220}Rn and ^{224}Ra nuclei was performed at the ISOLDE facility, CERN in August/September 2010 and September 2011. To date, the study of ^{224}Ra sets a record for the heaviest post-accelerated, radioactive ion beam (RIB) at ISOLDE, with the exception of the quasi-stable ^{238}U, and indeed the world. This chapter briefly describes the production of the nuclei studied (Section 3.1) and their acceleration through the REX linac (Section 3.1.2) to the Miniball spectrometer (Section 3.2).

3.1 The Radioactive Isotope Facility, ISOLDE

ISOLDE is a rare-isotope facility utilising the Isotope Separator On-Line technique, based at CERN in Geneva, Switzerland. The radioactive isotopes are produced in high energy, proton-induced reactions with a target material designed with chemistry, as well as nuclear physics, in mind. The protons arrive from CERN's PS Booster with an energy of 1.0 or 1.4 GeV and impinge on the primary ISOLDE target with a maximum current of 2.0 μA. Fission, fragmentation and spallation reactions have so far produced more than 600 isotopes of 70 elements from uranium carbide, molten lead and silicon carbide primary targets, amongst others. Up to

700 A of electrical current (equivalent to around 2000°C for a UC_x target) can be applied to the target to provide heating so as to thermalise the products and speed up the effusion and diffusion processes which govern the extraction of the species of interest and its subsequent ionisation. More detailed information on the ISOLDE facility is given in Reference [54].

3.1.1 Isotope production

Selection of the target material and ion source combination is crucial in extracting a high ion yield, and is dependent on the species of interest. In this work, two chemically very different elements are studied, one, radon, is a noble gas and the other, radium, is a group-two metal with a relatively low ionisation potential. In both cases, a $^{nat}UC_x$ target was used, impinged with 1.4 GeV protons at an average intensity of $\simeq 1.4\mu$A. However, the differences come in the ion source and transfer line combinations. For ^{224}Ra, the most simple set-up can be used, that of a heated transfer line made of tungsten, or indeed, tantalum, which has a higher thermionic work function than radium allowing for surface ionisation. It is not possible to use surface ionisation for ^{220}Rn because of the high ionisation potential of radon. Therefore, a plasma-ion source [55] is used, with a water-cooled transfer line which has the effect of suppressing the less volatile ions and reducing isobaric contamination.

Upon leaving the target, the 1^+ ions are accelerated to 30 keV and the isotope of interest is selected with the High Resolution Separator (HRS), a series of dipole and quadrupole magnets which separate according to the mass-to-charge ratio [56].

Accounting for efficiency losses through the HRS ($\text{eff}_{\text{HRS}} \simeq 80\%$), trapping and charge breeding ($\text{eff}_{\text{REX}} \simeq 60$ – 65%) and post-acceleration ($\text{eff}_{\text{EBIS}} \simeq 3$ – 5%), the production yield of ^{224}Ra has been estimated at 3×10^7 pps. For ^{220}Rn, the same efficiency values are assumed, leading to an estimated production yield of 1.0×10^7 pps.

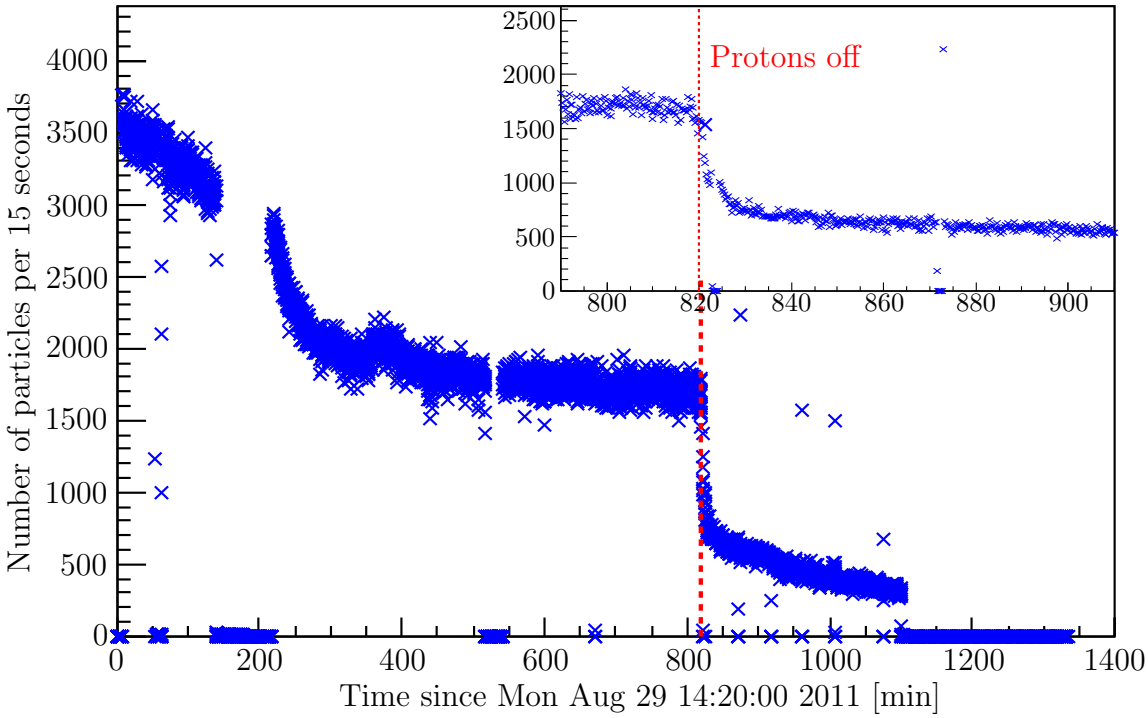

Figure 3.1: Rate of particles incident on the CD detector during and after protons were impinged on the primary target. The average current of the 1.4 GeV protons was 1.4 μA before the target was taken "off-line".

"Off-line" mode

The extraction of ^{224}Ra from the primary target can continue without a proton current on the primary target made possible by a combination of the relatively long half life of the isotope itself ($T_{1/2}$ = 3.66 days) and the α-decay parent nucleus, ^{228}Th ($T_{1/2}$ = 1.9 years). The former facilitates the survival of the species of interest until it travels from its point of production, through the target matrix, to the transfer line and subsequent acceleration, while the latter ensures an equilibrium is reached between extraction and production, yielding a reasonable production intensity without direct production of ^{224}Ra.

Data for the ^{224}Ra experiment was split between on-line and off-line mode, where the respective beam intensity at Miniball has been estimated at 5.8×10^5 pps and 6.2×10^4 pps, respectively, using the calculated cross-section for excitation of the ^{112}Cd target. This represents a factor of $\simeq 9$ reduction in production yield from

the primary target when the heating and isotope production is reduced without a proton current.

The assumption of an equilibrium is valid only when the chemistry of the parent, i.e. thorium, ensures it remains inside the target mass. As can be seen in Figure 3.1, the production rate decreases with time after protons are turned off as this is not the case for a long period. The immediate exponential drop observed is likely due to the cooling caused by the removal of the high proton current as well as the lack of direct production, hence it is difficult to ascertain the amount of nuclei produced via decay with respect to the proton-uranium reaction.

3.1.2 Post-acceleration: REX-ISOLDE

The Radioactive beam EXperiment (REX) is designed to accelerate the RIB from ISOLDE up to energies of 3.0 A.MeV. The final beam energy achieved during the experiments in this thesis were 2.85 A.MeV in 2010 and 2.82 A.MeV in 2011. The REX project has been outlined in References [57–63], and the design and commissioning report of Reference [64] contains a greater degree of technical details. Here, a summary of the acceleration procedure will be presented and a schematic representation can be seen in Figure 3.2.

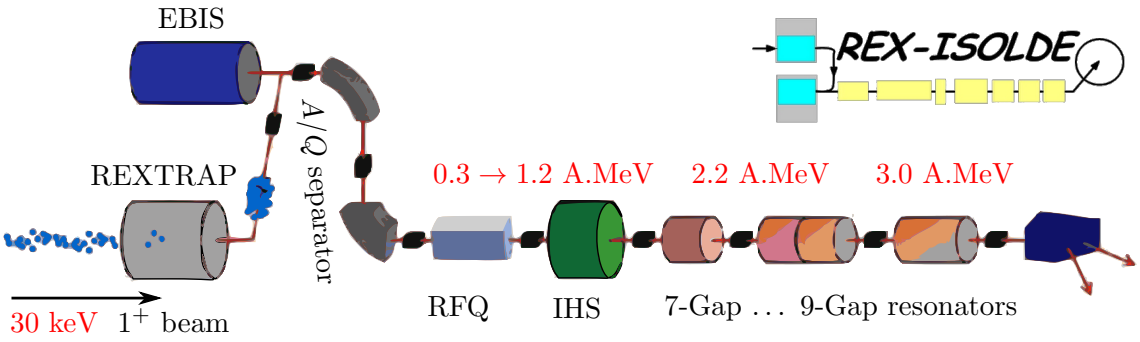

Figure 3.2: A schematic diagram of the REX accelerator. The energy at each step is indicated in red. The beam is delivered from the HRS at 30 keV in a 1^+ charge state (left to right in the diagram), bunched and charge bred to achieve a mass-to-charge ratio of $4.0 \leq A/Q < 4.5$ before mass separation and acceleration to the target position inside Miniball.

Bunching and charge-breeding

The semi-continuous 1^+ beam, from ISOLDE's HRS, is injected into REXTRAP [65, 66], a Penning trap designed to cool and bunch the ions. The cooling process, or deceleration, occurs firstly due to a high voltage barrier which reduces the 30 keV beam down to energies of eV magnitude, and then through collisions with an argon or neon buffer gas.

Charge breeding is achieved with an Electron Beam Ion Source (EBIS) [66–68], required for mass separation and to make compact linear acceleration feasible (the first element, the RFQ, requires that $A/Q < 4.5$. A 2-T superconducting magnet is used to confine a beam of mono-energetic electrons with a current up to of 500 mA which strip electrons via impact ionisation.

The trapping time is governed by the charge-breeding time, which in turn depends on the required charge state. For these heavy nuclei with $A \geq 220$, a charge state of $Q \geq 50^+$ is required to achieve an mass-to-charge ratio < 4.5, leading to a large breeding time of 400 ms, incurring increased efficiency losses. Charge exchange in the trap also causes loss of some 1^+ ions. However, the largest "bottle neck" with regards to the efficiency comes from the ions being distributed about a number of charge states in EBIS, resulting in an overall trapping/breeding efficiency of ($\text{eff}_{\text{EBIS}} \simeq 3 - 5\%$).

Mass separation and acceleration

Before injection into the linear accelerator, the beam, now consisting of n^+ ions, is passed through a mass separator with a resolution of $\frac{\Delta(A/Q)}{A/Q} \simeq 100$ [64]. At this stage, beam contaminants can come from the residual gas (atmospheric and REXTRAP buffer gas), amongst other sources, if a charge state of $Q = n^+$ reproduces a inseparable A/Q value. However, since these are a much lower mass than the beam species of interest (at least in this thesis), their cooling profile in REXTRAP is very

different, and these contaminants can be suppressed [69], although this mode of operation was not utilised for the experiments here. Some light mass contaminants are present at a low level in the ^{220}Rn(52^+) and ^{224}Ra(52^+) beams, however, their kinematics are very different and the scattering events can be disentangled with relative ease in Miniball.

Injection into the Radio-Frequency Quadrupole (RFQ) is the first step of the post-acceleration of the RIB [60, 61, 70]. This structure accepts the re-accelerated, 5 A.keV, n^+ ions from EBIS and enhances the energy to 300 A.keV. A rebunching takes place before injection to the IH structure, which further accelerates the beam to a variable energy between 1.1 and 1.2 A.MeV. Following this, a series three 7-gap resonators increase the beam energy to 2.2 A.MeV before the final cavity, a 9-gap resonator accelerates the beam to the final energy of $\leq$ 3.0 A.MeV.

Lead shielding and a concrete tunnel have been constructed to reduce bremsstrahlung radiation at Miniball caused by secondary electrons in the accelerator gaps.

3.1.3 Timing

The specific timing of the ISOLDE facility is schematically presented in Figure 3.3. Extraction of the beam from REXEBIS triggers the linear accelerator's 800-μs RF, "on-beam" window, 100 ms before injection. Usually, the entire release from REXEBIS occurs within the first $\approx$300 μs, but with large beam intensities, this causes pile-up events in the detectors and increases dead-time. To counteract this, a "slow-extraction mode" has been achieved reducing the instantaneous particle intensity at Miniball, prolonging the bunch with to around 500 μs.

The trigger from REXEBIS also opens an "on-beam" window for the Miniball spectrometer (see Section 3.2). During this 800 μs window, aligned with the accelerator's RF window, the data acquisition system records all information with each

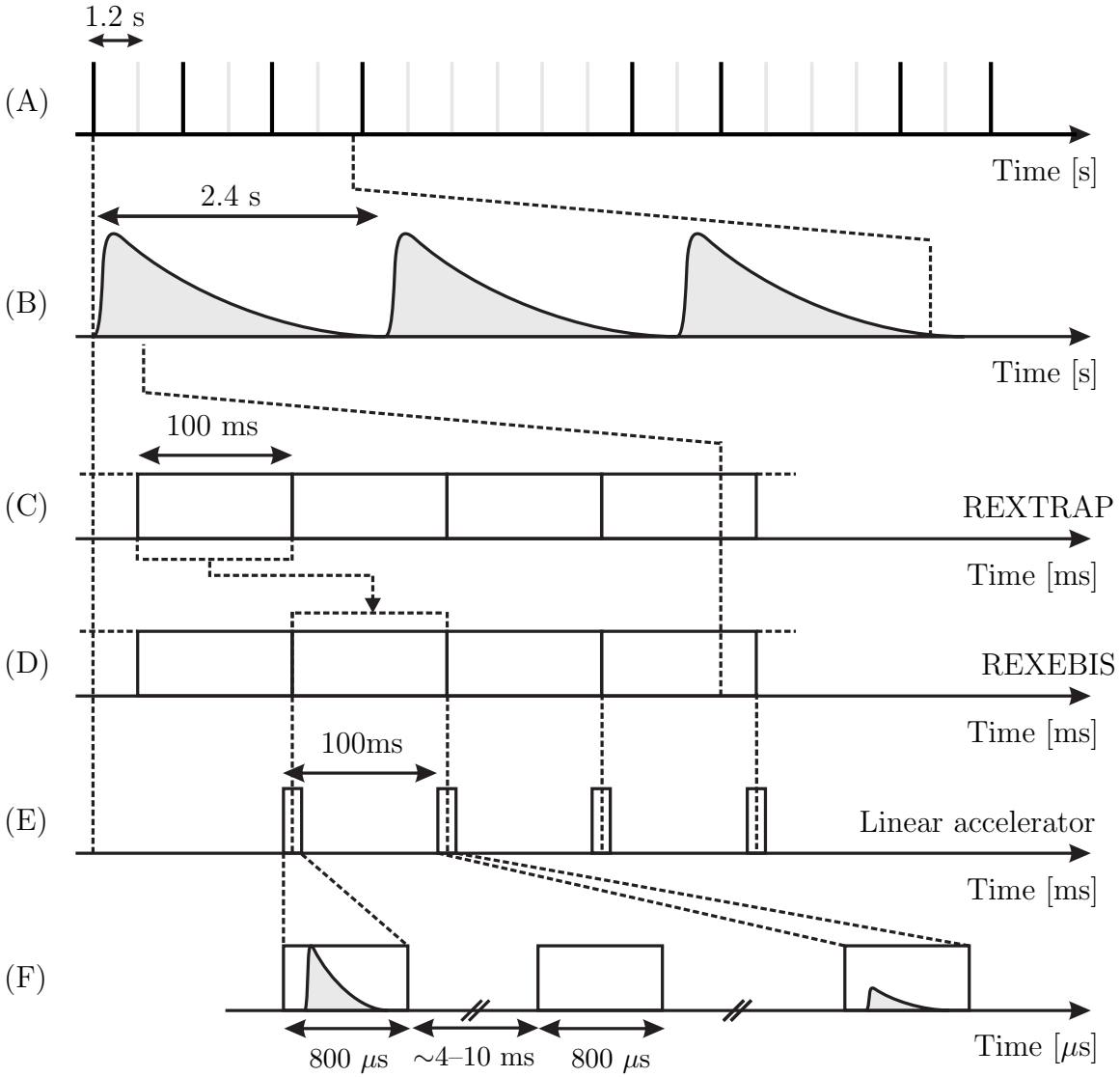

Figure 3.3: Schematic of the specific timing at ISOLDE. (A) The supercycle of proton bunches of ≈ 100 μs width from CERN's PS Booster separated by 1.2 seconds. The ISOLDE primary target receives an allocation of the bunches, shown in black, while others in the supercycle are distributed to other experiments. (B) Release profile of produced isotopes from the primary target. The release curves of ^{220}Rn and ^{224}Ra will be very different due to the varying half-lives and ionisation mode. (C-D) REXTRAP and REXEBIS beam bunches, synchronised with (E) the RF window of the REX linac. (F) The 800 μs "on-beam" and "off-beam" time windows using the Miniball setup.

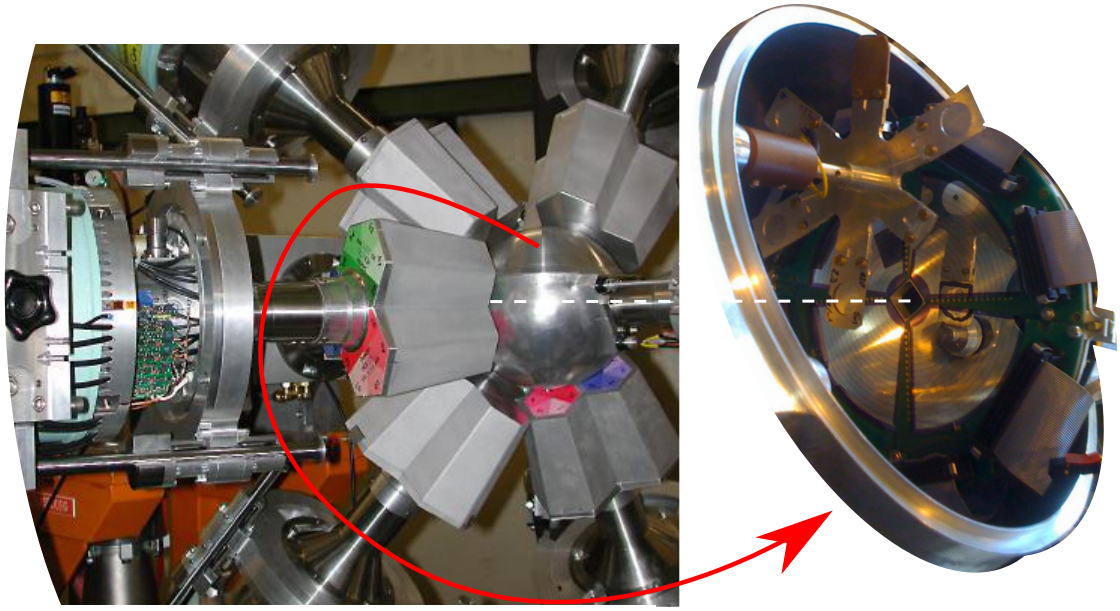

Figure 3.4: Photographs showing the Miniball clusters (not from this experiment, but reproduced from Ref. [73]) closed around the target chamber as well as the inside of the target chamber. The targets, positioned on the rotary target wheel, along with the CD detector are visible.

signal in each and every detector segment, individually timestamped. This later allows for a full reconstruction of the real events and coincidences.

3.2 Miniball

The Miniball spectrometer consists of eight triple-cluster HPGe detectors, each with 6-fold electronic segmentation. The array features a close geometry design, covering up to 65% of the 4π solid angle, and as a consequence has high detection efficiency for γ rays. Full design specifications and a greater degree of detail can be found in References [71, 72].

The high granularity of the detector array ensures good determination of the position of interaction, required for the determination of the angle for Doppler shift correction. Simply taking the centre of a given segment as the interaction point gives sufficient position sensitivity (limited by angular resolution of CD detector,

see Section 3.2.1), although pulse-shape analysis techniques have been shown to improve the effective granularity by a factor of ≈ 17 [71].

The Miniball set-up at REX-ISOLDE is the subject of a detailed review which can be found in Reference [74]. Presented in this section are the details and measurements, relevant to this thesis.

3.2.1 CD Detector

The CD detector is so named due to its physical similarity to a Compact Disc. It is, in fact, a Double-Sided Silicon Strip Detector composed of four quadrants each with 16-fold segmentation on the front side (annular p+n junction strips) and 24 n+n ohmic, radial strips on the back, electronically paired to give a 12-fold, electronic segmentation. The Si wafer has a thickness of 60 μm, providing ample of stopping for the heavy ions in this thesis, plus an inactive layer of between 0.3 and 0.8 μm of aluminium.

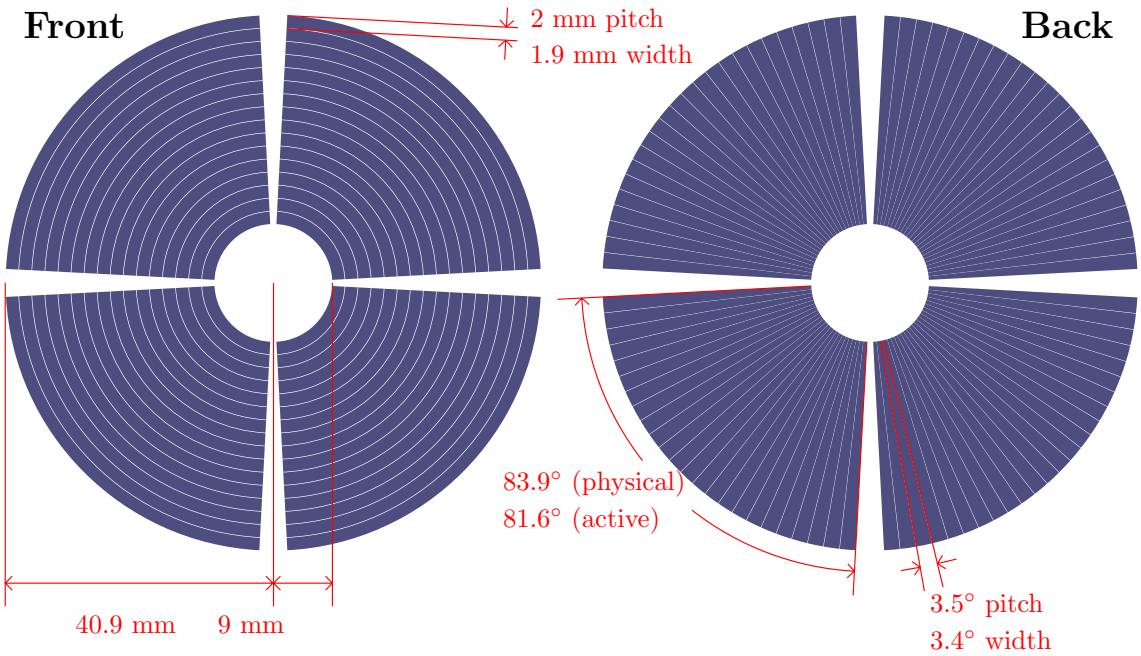

Figure 3.5: Schematic drawing of the double-sided silicon strip detector. There are small, 0.1 mm, inactive regions between the 1.9 mm wide annular strips and similarly, 0.1° inactive regions separate the 3.4° wide secular strips. The inner radius is 9 mm.

The azimuthal symmetry of the particle detector allows for a simple relationship to be made with scattering angle, while the high granularity aids in the angular correlation to coincident γ rays allowing for a well-determined Doppler correction. The energy of the detected particle is also used for determination of velocity in the Doppler-shift formula of Equation 3.2, and to identify projectile- and recoil-scattering events.

3.2.2 Efficiency determination

The γ-ray detection efficiency in the Miniball array needs to be known to good precision since this will impact on the uncertainty in the measured yields. A measurement took place before the beginning of the experiment in both 2010 and 2011 to determine the relative efficiency curve of the complete Miniball array in the energy range of interest. Sources of ^{152}Eu and ^{133}Ba were placed at the target position giving data points as low as 53 keV and as high as 1408 keV. The parameterisation used to determine the relative efficiency curve is shown below.

$$log(\epsilon) = a + b \cdot x + c \cdot x^2 + d \cdot x^3 + e \cdot x^4, \tag{3.1}$$

where ϵ is the relative efficiency, $x = log\left(\frac{E_\gamma}{E_0}\right)$ and $a - e$ are free parameters.

Using the measured relative intensities from the Evaluated Nuclear Structure Data File (ENSDF) at NNDC [75], one can fit an efficiency curve to the ^{152}Eu data points. The average ratio between this curve and the ^{133}Ba data points, N, is then calculated and a second curve constructed with the addition of the normalised ^{133}Ba data points. This normalisation is left as a free parameter during the fit of the second curve. The resulting fit parameters and their respective errors, obtained using GNUPLOT [76] and checked with TOPFIT [77], are listed in Table 3.1 and the efficiency curves shown in Figures 3.6 and 3.7.

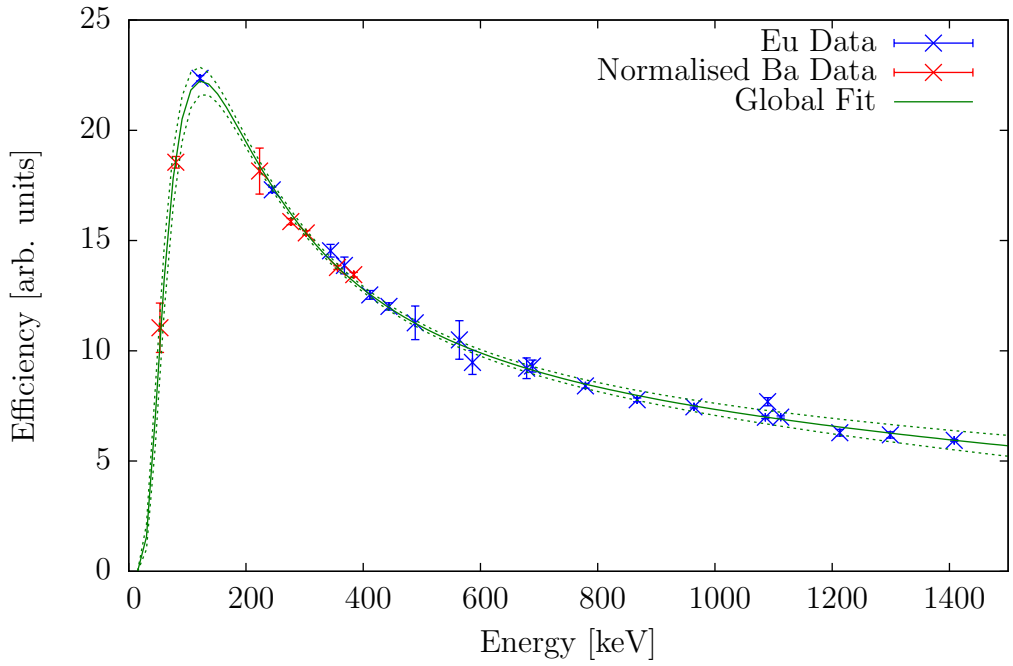

Figure 3.6: Relative efficiency curve for the complete Miniball array as determined in August 2010 with the add-back procedure on.

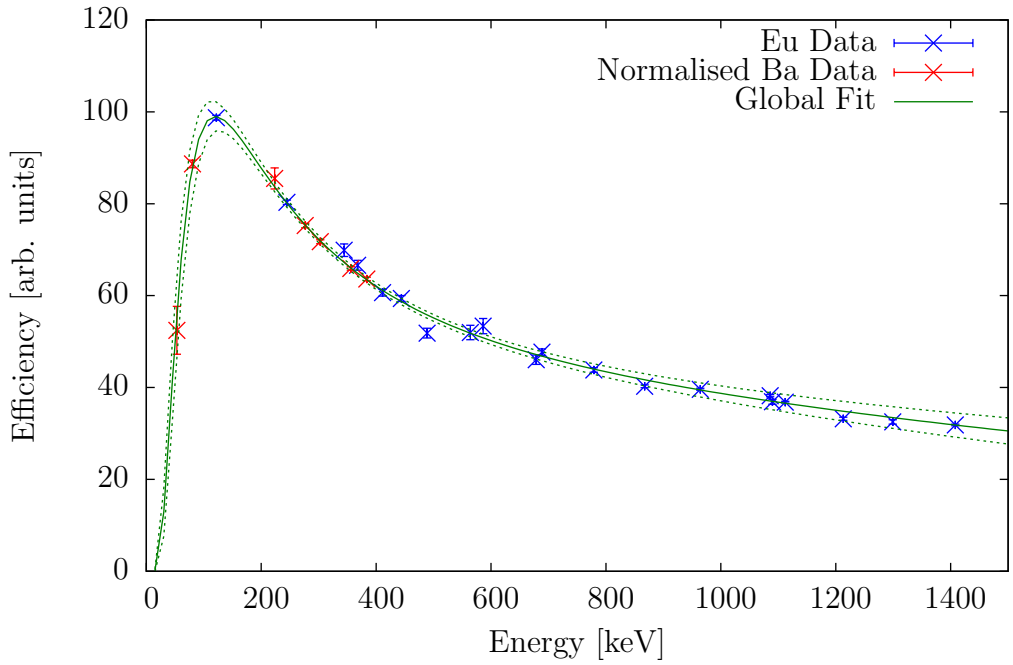

Figure 3.7: Relative efficiency curve for the complete Miniball array as determined in August 2011 with the add-back procedure on.

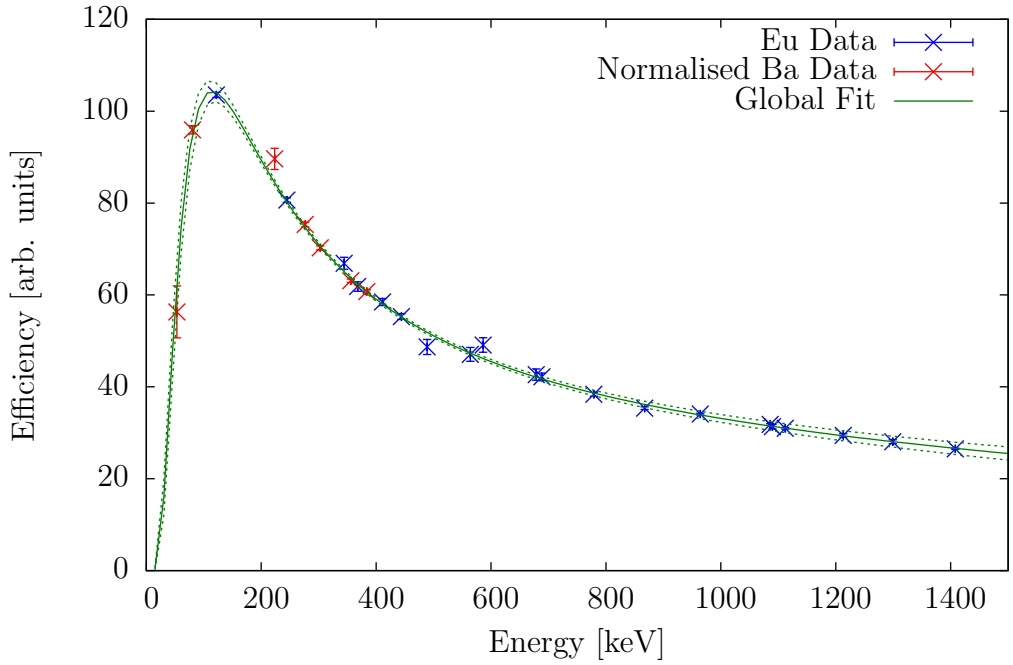

Figure 3.8: Relative efficiency curve for the complete Miniball array as determined in August 2011 with the add-back procedure off.

The E_0 factor is used to distribute the relative error correctly. Each parameter, a-e, has an error associated with it, extracted from the least-squares fit procedure and their contributions to the total error are added in quadrature. Except for the parameter a, all parameters have an energy-dependent contribution and this tends to zero when $E_\gamma = E_0$. Therefore, E_0 is found using an iterative approximation to reproduce a consistent energy dependent uncertainty function in the region where there is data. An E_0 value which is too small forces the error bars to increase at higher energy whilst decreasing the error bars at low energy, such that it becomes unphysical, and vice versa. For the current Miniball setup, it was found that a value of $E_0 = 325$ keV was most appropriate.

Table 3.1: Tabulated relative efficiency parameters of Equation 3.1 describing the fitted curves in 2010 and 2011 with and without the addback (AB) procedure turned on, shown in Figures 3.6, 3.7 and 3.8.

	2010	**2011 with AB**	**2011 without AB**
$a =$	2.683 ± 0.010	4.238 ± 0.011	4.212 ± 0.007
$b =$	-0.645 ± 0.013	-0.529 ± 0.015	-0.635 ± 0.009
$c =$	-0.04 ± 0.02	-0.032 ± 0.023	-0.060 ± 0.014
$d =$	0.128 ± 0.010	0.092 ± 0.011	0.100 ± 0.006
$e =$	-0.058 ± 0.010	-0.048 ± 0.011	-0.040 ± 0.007

3.2.3 Add-back routine

An add-back procedure is employed in the Miniball array so that events occurring in neighbouring detectors, i.e. the same cluster, within a $\pm$100 ns time window are added to give a single event. This allows for the full energy a single γ ray, which has under-gone a Compton scattering process and thus produced multiple "hits" in neighbouring detectors, to be reconstructed, therefore, increasing efficiency. The energies of the two or more events are summed and the segment with the highest energy is assumed to be the position of the first "hit".

Using ^{133}Ba and ^{152}Eu sources at the target position, the relative intensity of different γ rays with and without the add-back procedure, known as the AB-factor, has been measured and is shown in Figure 3.9. It is clear that there is a gain in efficiency above $\sim$ 250 keV and any loss in efficiency below this is measured to be, at most, 5%. Of course, random coincidences with γ rays emitted from radioactive nuclei in the target chamber or other background sources is possible, and this is the likely cause of the loss of efficiency at lower energies, since the Compton scattering cross-section decreases with decreasing energy.

The AB-factor is also affected by incorrect "add-back" of true γ-γ events, emitted in a cascade, since the timing resolution is not sufficient to distinguish these from Compton scattering events. This can be seen by an increase in the intensity of γ-ray

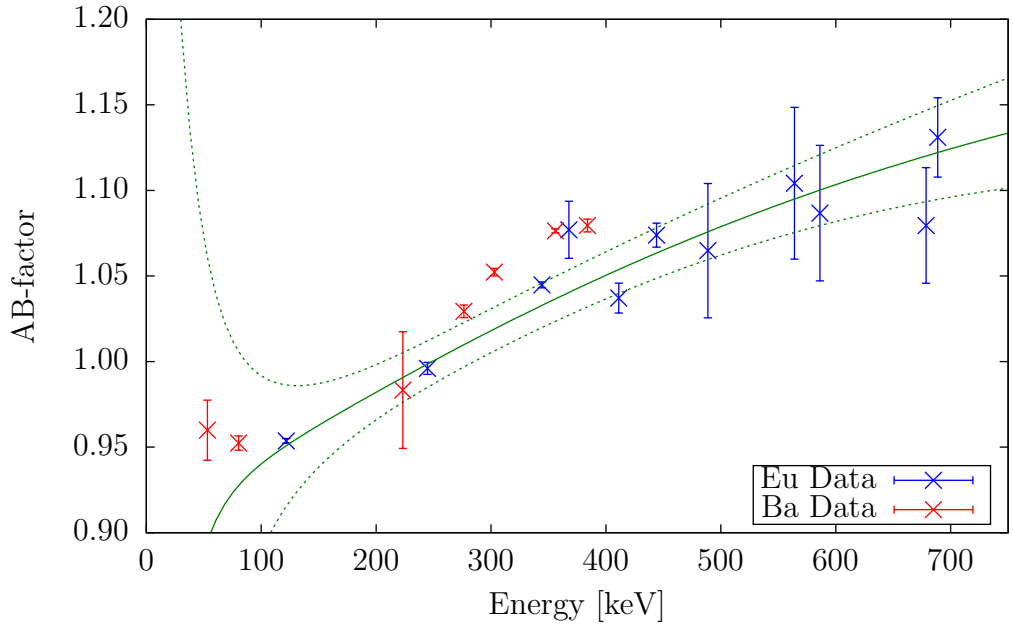

Figure 3.9: Ratio of Miniball efficiency with and without add-back. Data points are the ratios of the efficiencies of γ-decay lines from the ^{152}Eu and ^{133}Ba sources while the line shows the ratio of the two fitted efficiency curves shown in Figures 3.7 and 3.8 and is not a fit to the data itself. Please note that the error on this ratio becomes very large at low energies.

sum peaks, such as the 437 keV peak (see Figure 3.10) caused by the pile-up of the 356 keV and 81 keV γ rays. This effect results in a sum peak in the spectra of ^{220}Rn at 534 keV (see Section 4.2 and Figure 4.7).

3.2.4 Determination of Ge-detector positioning

The detector clusters of the Miniball array are mounted on a flexible frame allowing rotation of the clusters about the target position. Both the polar (θ_{clu}) and azimuthal (ϕ_{clu}) angles of each detector with respect to the incident beam can be adjusted during the installation of the clusters, as well as the rotation about its own axis (α_{clu}). Therefore, to determine angles precisely, a calibration method is necessary. Utilising the dependence of the Doppler shift on polar angle (as in Equation 3.2), and knowledge of the fixed cluster geometry, the parameters determining the cluster positioning can be fitted.

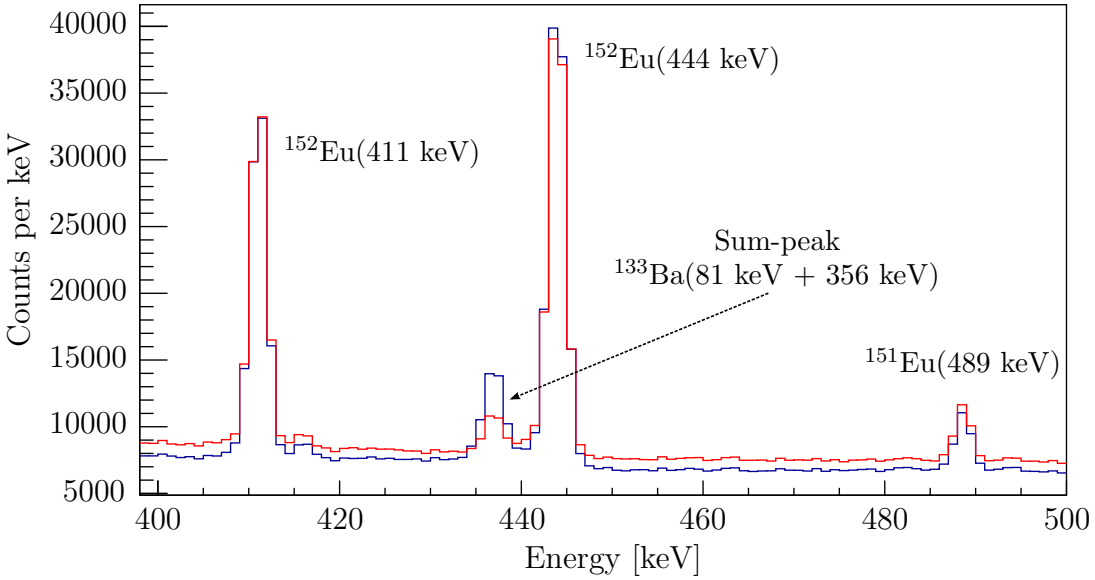

Figure 3.10: Miniball γ-ray spectra taken with the ^{152}Eu and ^{133}Ba sources in place showing the 437 keV sum peak caused by the pile up of the 81 keV and 356 keV γ rays in ^{133}Cs following electron capture in ^{133}Ba. The blue spectrum is taken with the add-back procedure on and the red spectrum without add-back. The add-back procedure incorrectly sums γ rays in a cascade which are both detected in the same cluster making it more probable that a pile-up event will occur and increasing the intensity of the sum peak seen in the spectra.

Calibration with ^{22}Ne

A ^{22}Ne beam is taken to the Miniball target position where a 1.9 mg/cm^2 thick, 98%-deuterated polyethylene target is placed. Two reactions, namely ^{22}Ne$(d,\gamma p)^{23}$Ne and ^{22}Ne$(d,\gamma n)^{23}$Na, populate excited states in the product nuclei, which then decay via 440 keV and 1017 keV γ-ray transitions, respectively.

Since the reaction is a case of extreme inverse kinematics, the maximum scattering angle is small, plus, the average polar angle over the 2π azimuthal range is zero, meaning the angle of the γ ray can be treated independently of the emitted nucleus. Therefore, the measured Doppler shift in each segment of the Miniball array, is a direct measurement of the recoil velocity, β, and the polar angle, θ_{seg}. Since all segments in a single cluster (3 detectors$\times$6-fold segmentation= 18 segments) have a fixed geometry relative to each other, a fit of the Doppler shift in each can be made to a total of 5 parameters, (d_{clu},θ_{clu},ϕ_{clu},α_{clu}, β), where d_{clu} is the distance from the

interaction point in the target to the interaction point in the Ge crystal.

β can be determined using a combination of LISE++ [78] and SRIM2010 [79] and is fixed to be equal for all clusters, although, it is left as a free parameter in the final fit to ensure convergence. Similarly, θ_{clu} is coupled for pairs of detectors by virtue of them being fixed to the same arm, allowing for further coupling in the fit.

The detector distance, d_{clu}, is not well determined since the mean-free path of γ rays in a solid material is non-zero and dependent on their energy. Since the γ-ray energies of interest in this thesis are relatively low in energy, the 440 keV transition is used for the determination of the angles, although good agreement has been found using data for both transitions.

The fit method is a simple and crude, iterative grid search, in which the starting parameters and limits are determined from reading the physical angles from the Miniball support frame. The frame angles are already a good starting point and can be determined to within $\pm 5^{\circ}$. Each parameter is varied independently, keeping all other fixed at their starting values and the best fit value, determining using a χ^2-type least-squares test, is stored. The new parameters are iteratively fed back into the grid search until a decrease in the total χ^2 is no longer obtained. Local minima cannot be differentiated from the true, global minimum with this iteration procedure, and so many different starting values must be used to test the validity of the fit. In the final analysis, there are many χ^2 minima which sit very close together, however, the ϕ_{clu} angle, for example, varies by a maximum of 0.3° between the different solutions.

3.2.5 Doppler correction

The velocity of scattered projectiles and recoiling target nuclei are significant enough to cause Doppler shift of the emitted photons. The energy of the detected γ ray is

shifted according to:

$$E_\gamma = \frac{\gamma E_0}{1 - \beta \cos \vartheta}, \tag{3.2}$$

where E_0 is the energy in the nucleus frame of reference, β is the nucleus' velocity in units of c, ϑ is the angle of the emitted γ ray with respect to the nucleus direction of motion and γ is the Lorentz factor $1/\sqrt{1-\beta^2}$. Using knowledge of the Ge-detector segment which is first "hit" by the γ ray and the segment of the CD detector in which the particle deposits its energy, a correlation between particle angles (θ_p, ϕ_p) and γ-ray angles $(\theta_\gamma, \phi_\gamma)$ can be made:

$$\cos \vartheta = \sin \theta_p \sin \theta_\gamma \cos (\phi_p - \phi_\gamma) + \cos \theta_p \cos \theta_\gamma. \tag{3.3}$$

By dividing E_0 by Equation 3.2 and substituting in Equation 3.3 one can extract a Doppler correction factor that can be used to correct the γ-ray energy,

$$\frac{E_0}{E_\gamma} = \frac{1}{\gamma} \left(1 - \beta \left(\sin \theta_p \sin \theta_\gamma \cos (\phi_p - \phi_\gamma) + \cos \theta_p \cos \theta_\gamma\right)\right). \tag{3.4}$$

Further to this, β can be determined from the energy deposited in the CD detector (E_p in units of MeV) and the simple kinetic energy relationship, $\beta = \sqrt{2E_p/m_0c^2}$, where m_0 is the mass of the detected particle in units of MeV/c^2.

Kinematic reconstruction

Every event needs to be corrected according to Equation 3.4, and to do this, both β and θ need to be determined on an event-by-event basis. This is a simple task when the particle and the γ ray which it emits are detected in coincidence. However, if the other collision partner is detected, say the target recoil when Doppler correction is required for the scattered projectile or vice versa, then a kinematic reconstruction is required to establish the projectile angle and velocity. The approximations used for these cases are shown in Appendix A.

Broken Miniball segments

Events occurring in dead segments are identified when a signal is observed only in the core, with no coincident segment signal. Since the add-back procedure uses the full energy signal at the core, but the angular information from the segments and the latter information is missing, zero values are registered for the angle. This leads to an incorrect Doppler correction factor for these events. This is seen as a misshapen peak and is not immediately obvious in the data until each cluster is plotted individually. In these spectra, the effect manifests itself as a small peak or "bump" on the edge of the correctly Doppler corrected events.

The solution is to trap these events during the sort procedure, i.e. those which have a core signal but no segment signal, and reassign the respective $(\theta_\gamma, \phi_\gamma)$ angles with those of the core. This determines the angles with a great enough precision to provide sufficient Doppler correction at the recoil velocities in this thesis.

Chapter 4

Coulomb excitation of ^{220}Rn and ^{224}Ra

This thesis centres on the investigation of $E3$ matrix elements in nuclei where octupole correlations are expected to be strongest, namely ^{220}Rn and ^{224}Ra, have been studied so far. Coulomb excitation (see Chapter 2) is the only reasonable way of accessing $E3$ transitions in these nuclei, and since they and the neighbouring nuclei in the actinide nuclei are unstable, radioactive ion beams (see Chapter 3) are required. This chapter presents the spectroscopy of the ^{220}Rn and ^{224}Ra beams and the segmentation of the data into different target and scattering angle combinations.

Target selection

Both beams were studied using nickel ($Z = 28$), cadmium ($Z = 48$) and tin ($Z = 50$) targets, providing differing kinematics, and therefore differing sensitivity to the Coulomb excitation process. In the case of the cadmium experiments, ^{114}Cd (^{220}Rn,^{220} Rn*) and ^{112}Cd (^{224}Ra,^{224} Ra*), the increased probability of target excitation coupled with their relatively well-measured spectroscopic properties leads to the possibility of an absolute cross-section, and therefore beam intensity, measure-

ment. However, this information is not required for the final analysis of Chapter 5 as both nuclei studied have precise measurements of the lifetimes of their first excited, 2^+ (and 4^+ in the case of ^{224}Ra) states, providing a well defined normalisation. Consequently, a ^{120}Sn target was used in the study of both nuclei because of the very high first 2^+ energy and low probability of target excitation. Not only does this reduce any, already negligible, effects to the semi-classical approximation, the lack of γ-ray de-excitation of the target results in spectra without the high background from the Compton scattering caused by a high-energy transition. A lighter target in ^{60}Ni, also with large E_{2^+} and low $B(E2; 2^+ \rightarrow 0^+)$, gave increased sensitivity to single-/multi-step excitation and reduces the feeding from higher states to the 3^- state of interest.

4.1 Event selection

The timing scheme for the Miniball setup at ISOLDE is laid out in detail in Ref. [74]. In the following (Section 4.1.1), the definition of prompt and random events will be outlined and the background subtraction technique described. The particle gating, which leads to the selection of the (Z, θ) experiments, is described in Section 4.1.2.

4.1.1 Time windows

The time difference between the detection of a γ ray, and a particle in the same EBIS pulse, is used to determine whether or not they are correlated. The prompt coincidence window is determined from Figure 4.1, which shows the true coincident events in a peak around 600 ns wide. Events outside of this peak can be attributed to the correlation of a γ ray with an elastically scattered particle from a different collision to the one which caused the excitation. These random events are used to determine the background spectra, which are subtracted from the prompt co-

incidence spectra scaled by the width of the respective time windows, assuming a background constant rate across the correlation time used.

Downscaling problems

In 2011, when data was taken with the ^{220}Rn beam, a downscaling factor, n, of 2 was used to reduce the number of randomly correlated, elastically scattered particles, with the goal of improving dead-time and reducing the size of the raw data. An 800 ns hardware time window is triggered by the detection of a γ-ray in Miniball and only 1 in 2^n particles (25% in this case) which fall outside of this window are written to the data stream. This, however, caused unforeseen problems since the delayed particles appear to fall close to the edge of the 800 ns γ-ray trigger (Figure 4.1 (b)).

When downscaling is used, the background subtraction isn't so simple. To overcome the artificial variation in the random spectra due to downscaling, the γ-ray de-excitation of β- or α-decay daughter nuclei can be utilised. The radioactive beam scatters into the walls of the chamber or remains implanted in the Si wafer of the CD detector, subsequently decaying. Excited states are formed in the daughter nuclei and their γ-ray decay is randomly correlated to particle events, providing time-independent background peaks in the spectra, the intensities of which can be used to normalise the prompt and random windows.

More importantly still, the possibility of prompt events being downscaled means that the particle-γ efficiency is compromised and cannot safely be assumed to follow the γ-ray singles curve. Since the timing resolution of a Ge detector degrades with lower energy γ rays the effect on the efficiency is energy dependent. Figure 4.2 shows four normalised time difference spectra gated on different energy transitions. The lowest energy gate is on the X rays at 85 keV and it is clear that the large tail on the right-hand side of the peak is caused mainly by the poor timing resolution of

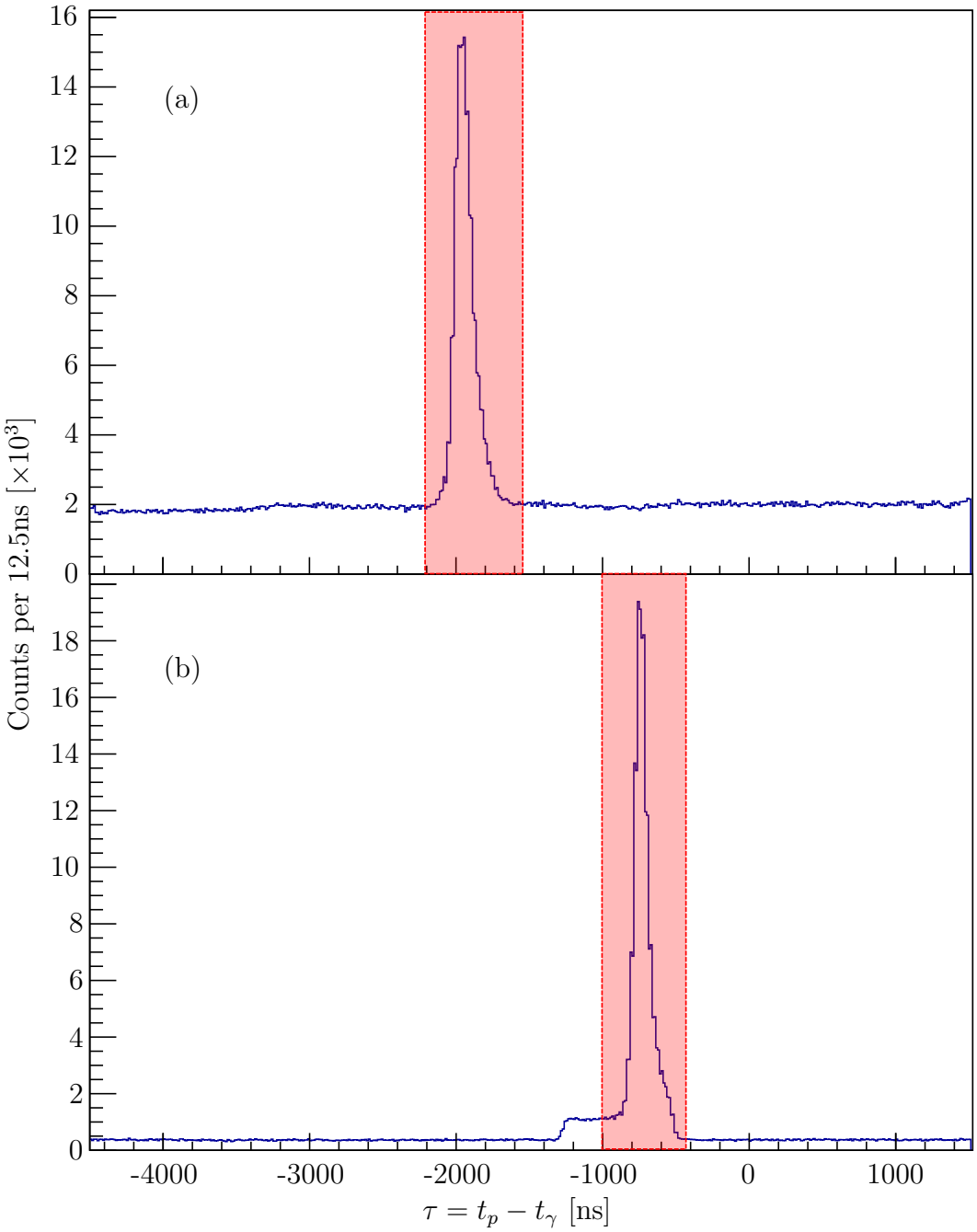

Figure 4.1: (a) Particle-γ time difference in the ^{224}Ra on ^{112}Cd experiment. A software time window about a particle event in the CD detector is positioned such that all prompt, true γ-ray coincidences are recorded. These are seen in the peak centred around -2000 ns, where the offset is caused by the different timing properties of the electronics and a delay on the particle signal. There is no hardware coincidence condition set and elastically scattered particles, which are randomly correlated to γ rays, are not downscaled (explained in Ref. [74]). (b) As for (a) but for the ^{220}Rn on ^{60}Ni experiment where the downscaling was applied. Please note here how the prompt window overlaps the downscaled region.

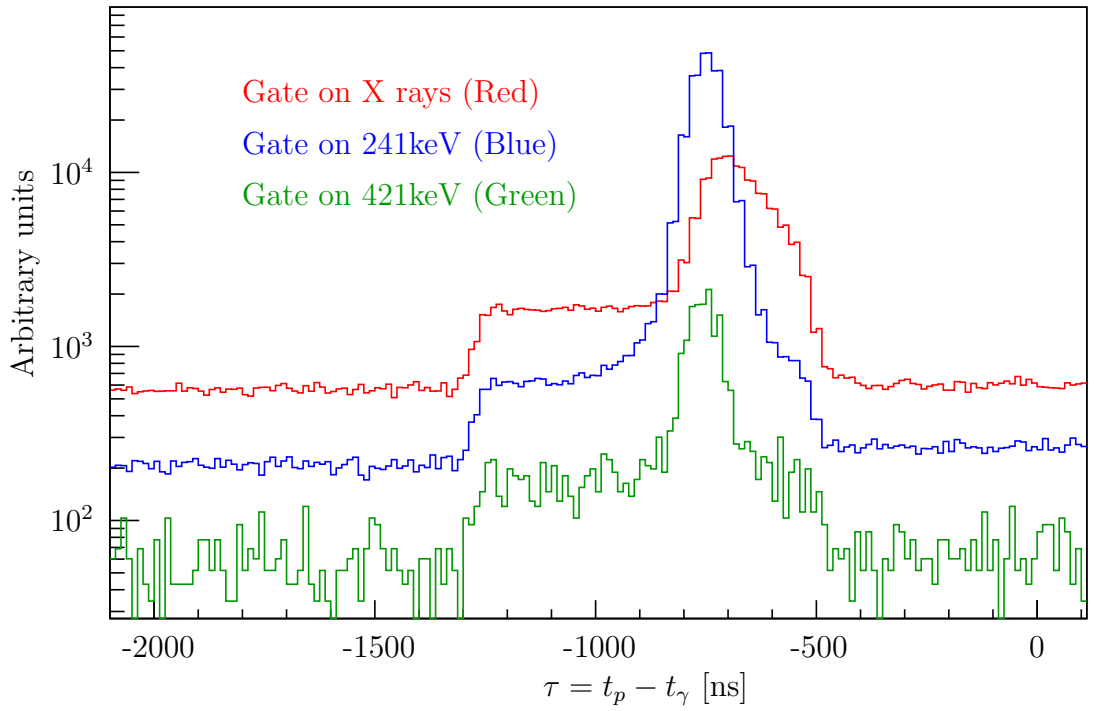

Figure 4.2: Particle-γ time difference in the ^{220}Rn on ^{60}Ni experiment, gated on the energy range for X rays (red), the $2^+ \rightarrow 0^+$ transition at 241 keV (blue) and the $3^- \rightarrow 2^+$ transition at 421 keV (green). Degradation of timing with decreasing energy deposited in the Ge detectors is seen in the increase in peak width.

these events. Critically, the events gated on 241 keV transition (the lowest observed transition in these experiments) do not fall outside of the downscaling window, supporting the use of relative efficiency curve of Figure 3.7 for this energy regime.

4.1.2 Particle Identification

The use of heavy beams leads to inverse kinematics, where the mass of the projectile is greater than that of the target mass. This has consequences for the kinematics in the laboratory frame, namely a maximum projectile scattering angle, θ_P, given for elastic scattering by:

$$\sin\theta_P = \frac{m_T}{m_P}\sqrt{1 - \frac{\Delta E}{E_P}\left(1 + \frac{m_P}{m_T}\right)}, \tag{4.1}$$

where ΔE is the energy transfer, E_P the projectile energy and $m_{T,P}$ the masses of the target and projectile, respectively. Although, since $\Delta E << E_P$, Equation 4.1 can be approximated to elastic scattering and simplified to $\sin\theta_P = \frac{m_T}{m_P}$. For ^{220}Rn on ^{120}Sn, this maximum laboratory angle is 33° and can be seen in Figure 4.3 (a).

This leads to an ambiguity between centre of mass angle and projectile angle, where the laboratory angle has two solutions. These solutions can be separated by energy, but this becomes troublesome around the maximum angle where problems are caused by a lack of granularity in the particle detector and energy straggling caused by the interaction in a target with a finite width. However, no such problem exists for the target recoils, where the translation from centre of mass scattering angle to laboratory angle, θ_T, is single valued. For that reason, the angular range is defined in terms of the detected recoil and a gate constraining the energy and angular range is applied to select recoils in the range where there is no ambiguity. A projectile gate is also defined to determine true coincidences, that is if the first particle passes the recoil gate and the second passes the projectile gate. If the second particle does not pass the projectile gate, then it is considered a randomly correlated particle, and the event is treated on the basis of recoil detection only.

The recoil gate is further split to give two ranges in the centre of mass (CoM) scattering angle. Events occurring in strips 3–8 of the CD detector are considered for the high CoM angular range, and those in strips 9–16 for the low CoM angular range. By splitting the data in this way, sensitivity to the Coulomb excitation cross section is increased.

4.1.3 Particle Multiplicity

Events are sorted such that each and every detected γ ray is correlated to a single prompt or random particle (1-p events), two prompt or random particles (2-p events) or even higher multiplicities (n-p events). It is also possible that a correlation is made

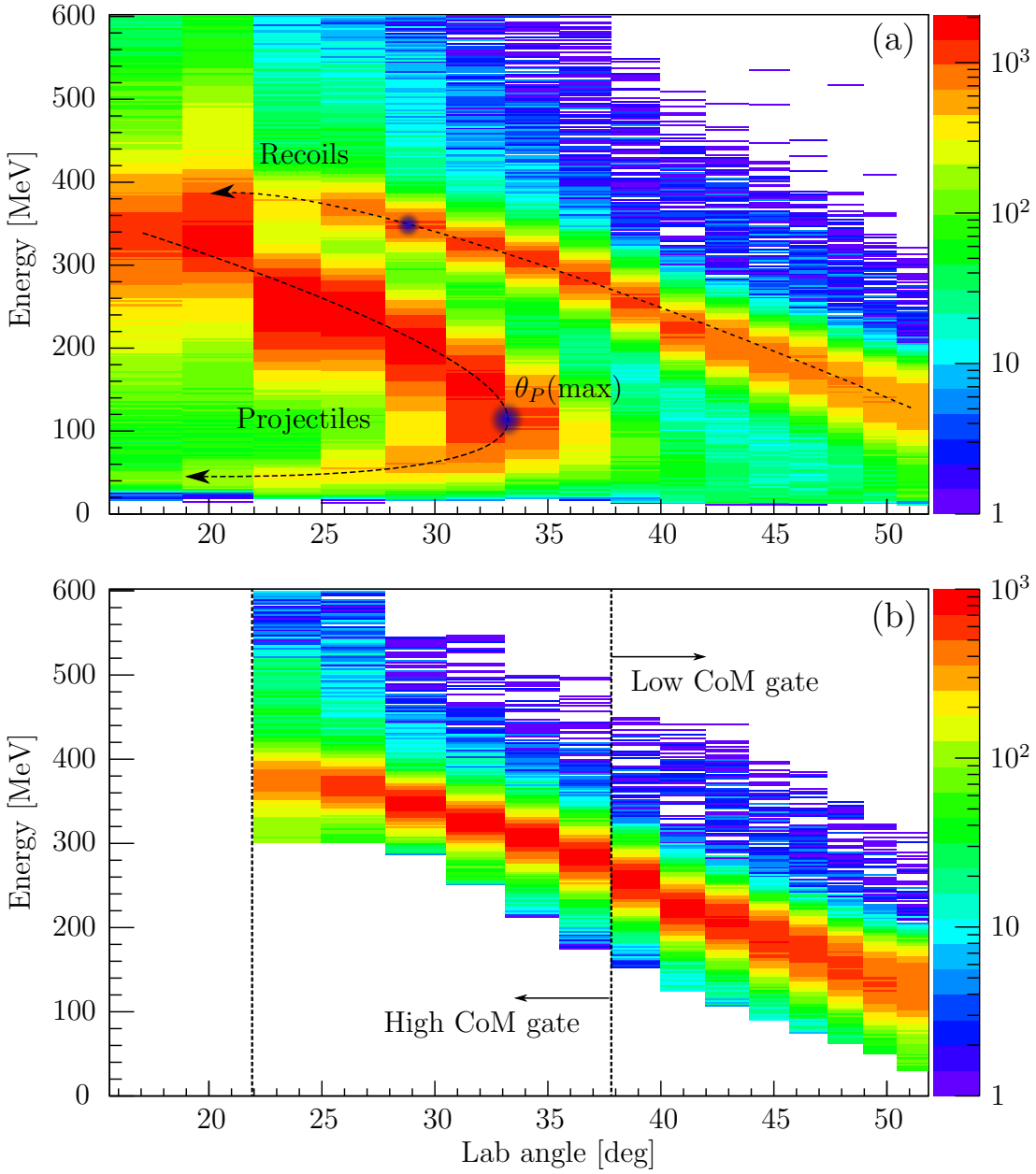

Figure 4.3: (a) Particle spectrum taken in the CD detector for the ^{120}Sn(^{220}Rn,^{220}Rn*) experiment at 2.82 A.MeV. The arrows show the direction of increasing centre of mass (CoM) scattering angle, while the blue dots represent a target and projectile at the same CoM angle. The z axis represents the number of events per 2 MeV, per CD strip. Notice that each strip has a different angular pitch and so it is not proportional to "per degree". (b) As in (a), but now with the recoil gate applied. The two inner most strips of the CD detector are not used for the recoil gate due to the overlap with the projectiles in this region.

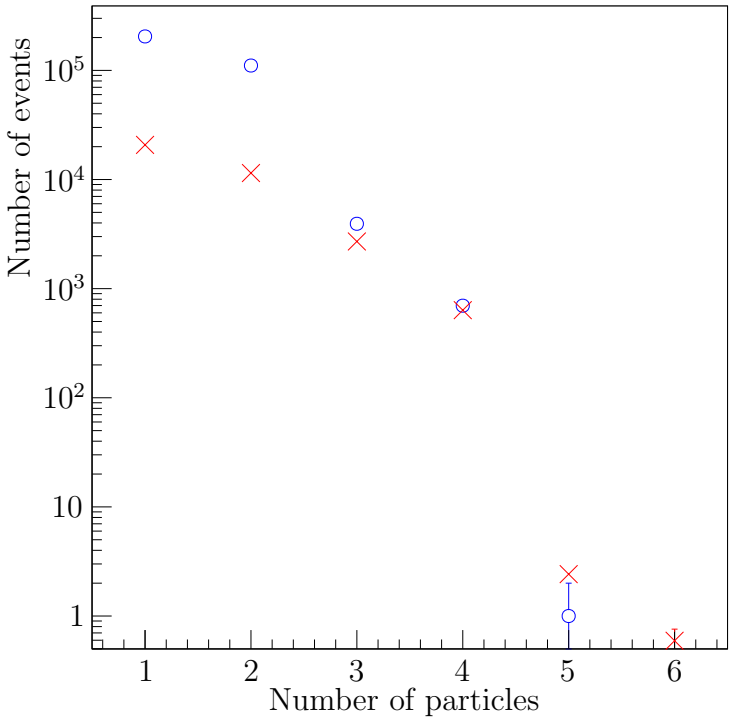

Figure 4.4: Particle multiplicity for the ^{112}Cd(^{224}Ra,^{224}Ra*) experiment. The blue circles (○) are prompt events, i.e those inside the prompt window of Figure 4.1, while the red crosses (×) are random events, those outside of the prompt window of Figure 4.1, normalised to the prompt data using the ratio of the respective window widths. Multiplicities greater than 2 account for $< 1.5\%$ of the total events.

between a γ ray and a combination of prompt and random particles and in this case, the random events are not considered and the particle multiplicity is considered to be that of the number of prompt particles.

As can be seen in Figure 4.4, the number of events with a prompt multiplicity greater than 2 represent a small fraction of the total data. These events are caused by a genuine 2-p event where both recoil and scattered projectile are detected, plus a number of randomly correlated elastically scattered particles from an independent collision. However, 3-p events can still be filtered and the random event rejected by utilising kinematic relationships between the real prompt events. So far, 4-p events and higher have not been included in the data.

The assumption that the kinematic relationship between projectile and recoil is clean, is tested in Figure 4.5. If the particle detection efficiency were equal to 100%, every prompt γ ray would be in coincidence with two particles. However, after setting the condition for recoil detection between 22° and 52°, the correlated projectile is not detected 16% of the time. Only a factor of 2% can be attributed to

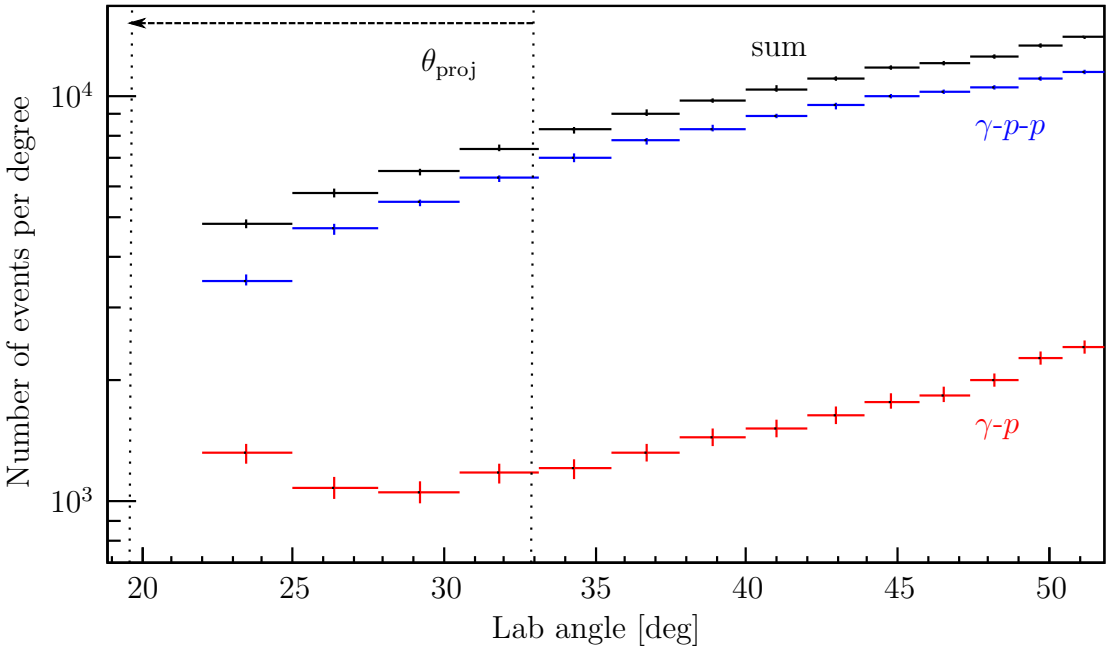

Figure 4.5: Experimental recoil scattering cross-section as a function of recoil scattering angle for γ-particle and γ-particle-particle events for the ^{120}Sn(^{224}Ra,^{224}Ra*) experiment. The data show the number of events per degree in each strip of CD detector, separated into 1-p (red) and 2-p (blue) events, while the black data points are the sum. The x-axis range represents the angular range spanned by the CD detector while the dashed vertical lines show the limits of the projectile angle corresponding to the extremes of the recoil angle.

the dead regions separating the segmented annular rings of the detector, while it is also possible for a small fraction of events to pass between quadrants of the detector due to the finite width of the beam spot.

The non-linearity of the 1-p cross-section suggests that other, angular dependent effects cause the loss of the second collision partner also. At higher laboratory angles for recoil detection, the correlated projectile is at very low angles close to the inside edge of the CD detector and it becomes more likely that it will scatter below the detectable angular range when a finite beam spot width is considered. A small drop in projectile detection efficiency is also observed at the lowest recoil angles around 24°, corresponding to projectile angles around the maximum.

By summing 1-p with 2-p (including 3-p or γ-projectile-recoil-random) events the, albeit small, angular effect on the projectile detection efficiency is eliminated

and an increase in the total number of events is obtained over the strict selection of two particle kinematics.

4.2 Spectroscopy of ^{220}Rn via Coulomb excitation

The low-lying level scheme of ^{220}Rn has been previously measured using β- [80, 81] and α-decay spectroscopy [36, 82, 83]. This was extended, using γ-ray spectroscopy following multi-nucleon transfer reactions, to high spin by Cocks *et. al.* [20] and all odd and even yrast states of the octupole band, up to and including $I^\pi = 21^+$, have been placed. Collated information from the Nuclear Data Sheets [84] is used to construct the level scheme shown in Figure 4.6. The placing of the new level at 937.9(10) keV and its $I^\pi = 2^+_\gamma$ assignment is discussed in Section 4.2.1.

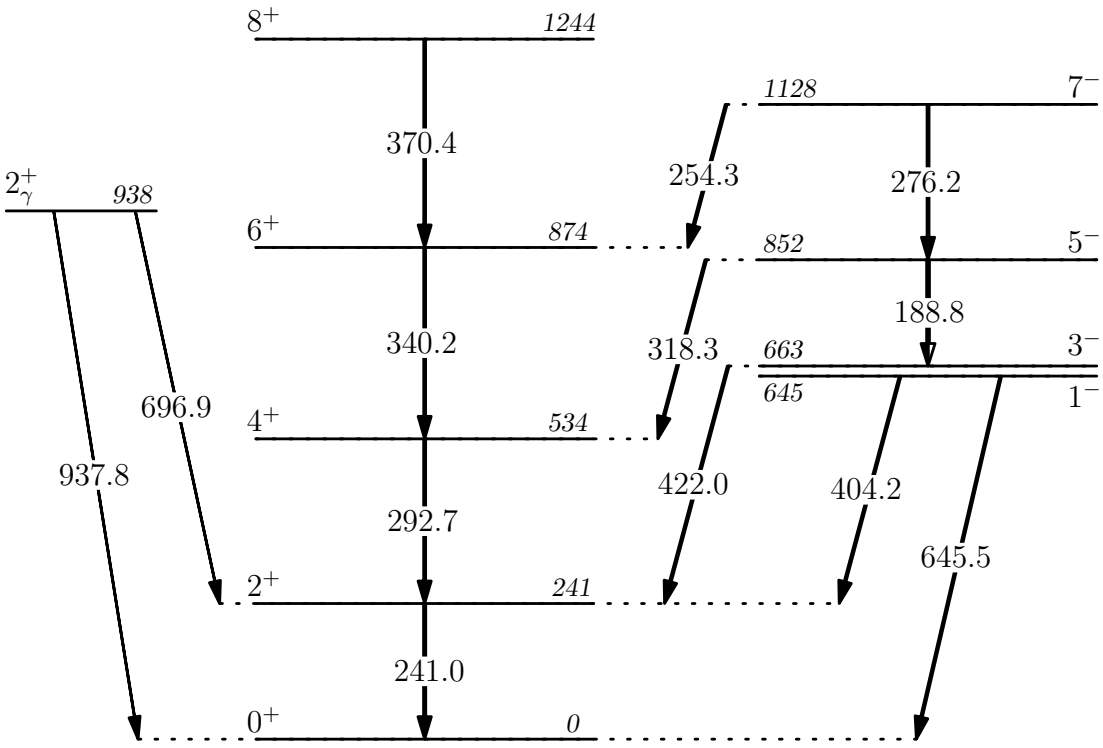

Figure 4.6: Reduced level scheme of ^{220}Rn.

An initial sorting of the data uses a particle event in the CD detector as a trigger and correlates this to all γ rays which fall inside the time windows described

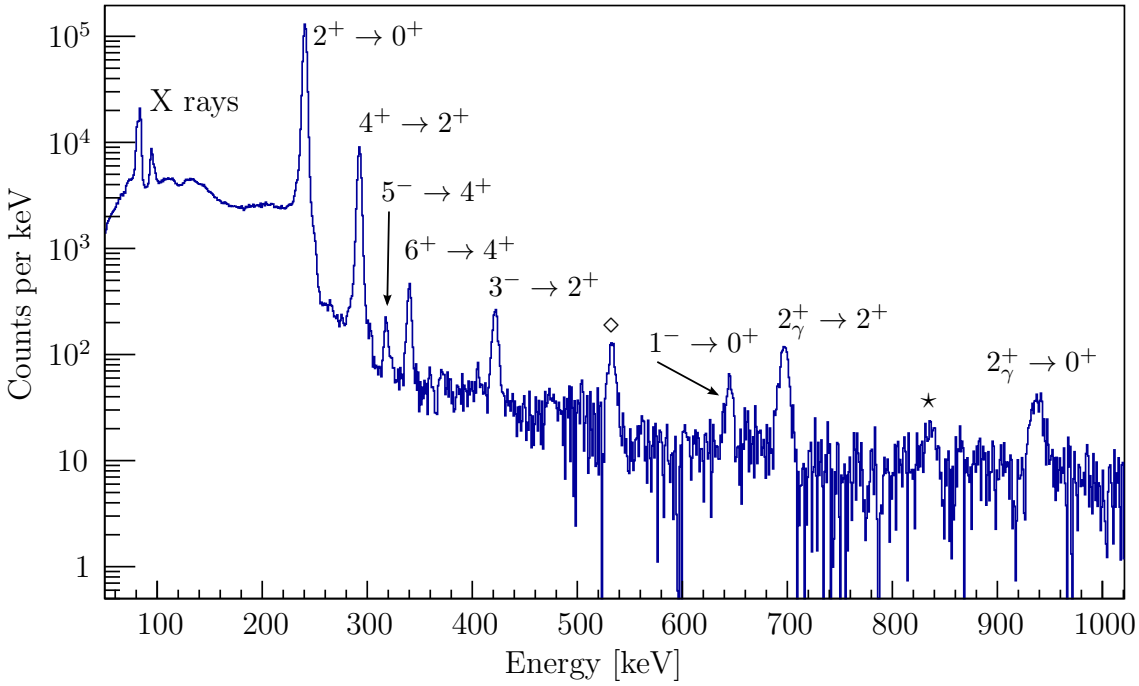

Figure 4.7: Gamma-ray spectrum of particle-*gamma* singles events in ^{220}Rn, Doppler corrected and background subtracted. Transitions labeled were either previously observed or determined in this work (see Section 4.2.1). The 534 keV peak, labelled with a diamond (◇), is a sum peak caused by the pileup of the 241 keV, $2^+ \rightarrow 0^+$ and 293 keV, $4^+ \rightarrow 2^+$ transitions. The 836(2) keV peak, labelled with a star (⋆), is unplaced in this nucleus. Data from Sn and Ni target experiments are summed but the Cd data is not included for clarity of presentation.

in Section 4.1.1, yielding events of type p-$n\gamma$, where n is the number of γ rays in coincidence with the particle, p. The majority of these events are p-0γ or p-singles events, since the most likely collision is an elastic one, meaning there is no excitation and subsequent γ-ray decay associated. Those events with $n > 0$ are expanded to particle-*gamma* singles events and are Doppler corrected, background subtracted and shown in spectrum of Figure 4.7, which now includes all γ rays definitively correlated with either a projectile or a target recoil.

Events with $n \geq 2$ are reduced to p-γ-γ events and form a γ-γ matrix, the projection of which is shown in Figure 4.8. The "total statistics" spectra, coupled with γ-γ coincidence analysis allows confirmation of the known level scheme, along with the measurement of two branching ratios, presented in Table 4.1. The total

intensities of all measured transitions are presented in Table B.1 as Experiment No. "p-γ".

4.2.1 Vibrational states

In this region of the nuclear chart, vibrational states are observed at low energy, around 1 MeV. Bands associated to γ and β vibrations have been populated in heavy-ion Coulomb excitation experiments in neighbouring thorium nuclei [85]. The level at 937.8(8) keV in Figure 4.6 is proposed to be one such state, namely, the 2^+ member of the $K = 2$, γ-vibrational band. This level has been observed for the first time in this work, although its decay to the lowest 2^+ state was listed as an unplaced transition in the β-decay studies of Liang *et al.* [80].

The decay of the 2^+_γ state to both the ground state and the first excited 2^+ can be seen in Figure 4.7 in the form of 937.8(12) keV and 696.9(10) keV transitions, respectively. The placement of the level is supported by the energy difference between the two transitions, 240.9(16) keV, being consistent with the energy difference of the 2^+ and 0^+ states, but also by analysis of the γ-γ matrix. The projection, shown in Figure 4.8, implies that the 937.8 keV transition is not coincident with any other, while the 696.9 keV transition is coincident with the $2^+ \rightarrow 0^+$ transition only (see inset of Figure 4.8).

A transition to both $I^\pi = 0^+$ and 2^+ states requires the state to be either $I = 1, 2$, ruling out $I = 3$ (and higher) since the $\Delta I = 3$ transition to the ground state would be greatly hindered compared to the $\Delta I = 1$ transition to the 2^+ state. A $I = 0$ state is also not possible because of the observed γ-ray decay to the 0^+ ground state. Coulomb excitation of unnatural parity states, such as a 1^+ or 2^-, is orders of magnitude less likely than excitation of natural parity states [47]. The significant population of this state, which is not fed from γ-ray de-excitation (no γ-γ coincidences with the $2^+_\gamma \rightarrow 0^+$ transition), implies a 1^- or 2^+ spin and

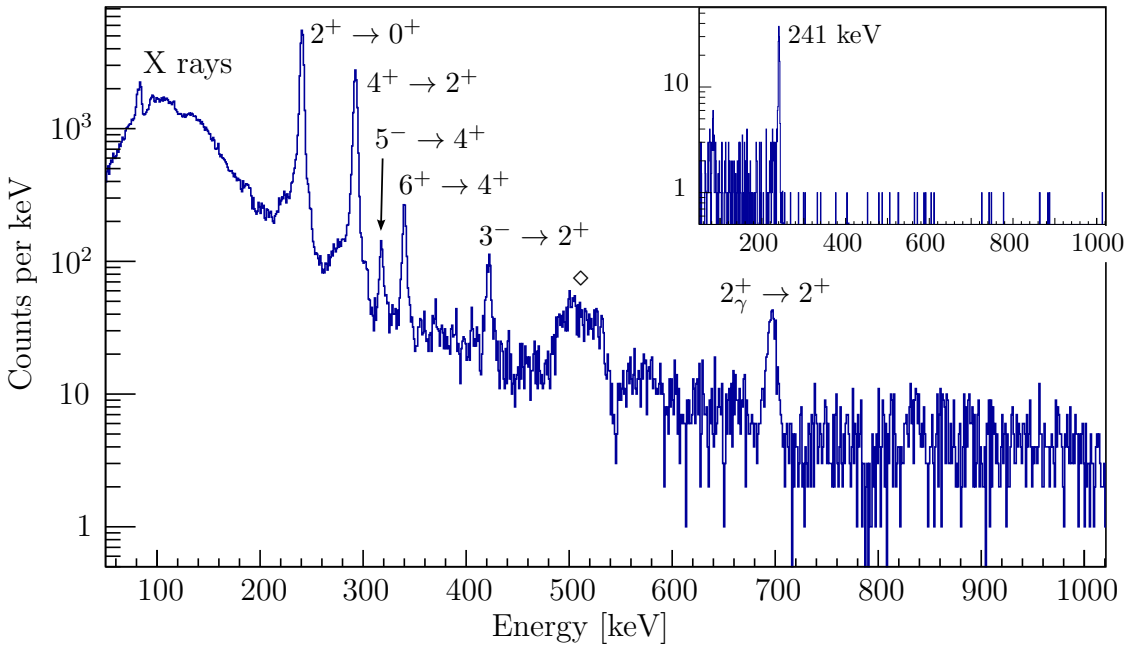

Figure 4.8: Projection of the particle-γ-γ matrix of events with the ^{220}Rn beam. The matrix is symmetrised with Doppler corrected events and those random in time are subtracted according to the ratio of the relative prompt/random window widths. The "bumps" on the left edge of the 241 keV, $2^+ \rightarrow 0^+$ and 293 keV, $4^+ \rightarrow 2^+$ peaks are caused by Compton scattered events. The diamond ($\diamond$) indicates the 511 keV annihilation peak, smeared out due to the Doppler correction. The inset figure shows the projection gated on the 697 keV transition. Data from Sn and Ni target experiments are summed but the Cd data is not included for clarity of presentation.

parity assignment. A 1^- level would be populated via an $E3$ excitation from the 2^+ state, similar to 645 keV level, but the much higher energy difference would require an impractically large $E3$ matrix element connecting the states to reproduce the population observed. Therefore, a $I^\pi = 2^+$ assignment is made.

The γ-ray branching ratio for the decay of the state can give an indication of its structure. Comparisons are made to the prediction of the Alaga rules [86] and the Bohr and Mottelson rotation-vibration model [6], assuming the same correction factor, $\alpha_\gamma = 0.030$, as measured in ^{232}Th [85], shown in Table 4.1. The branching ratio of the proposed $I^\pi = 2^+_\gamma$ state at 938 keV, decaying to the 2^+ and 0^+ members of the ground band, agrees well with the rotation-vibration prediction, supporting the assignment as the $K = 2$ band head.

Table 4.1: γ-ray branching ratios in ^{220}Rn, measured in this work, compared with the predictions of the Alaga rules and the rot-vib model of Bohr and Mottelson.

State (I_i)	I_1	I_2	$Y_\gamma(I_i \to I_1)/Y_\gamma(I_i \to I_2)$		
			Experiment	Alaga	Rot-Vib
2^+_γ	2^+	0^+	2.1 ± 0.5	0.32	2.41
1^-	2^+	0^+	0.26 ± 0.12	0.49	—

4.2.2 Data segmentation

As discussed at the start of this Chapter, and Section 4.1.2, the data is segmented to give different (Z,θ) combinations (see Section 5.1 for details). A lighter target with a lower-Z value reduces the probability of multiple-step Coulomb excitation, leading to sensitivity to different excitation paths. This effect can be seen in the γ-ray spectrum of Figure 4.9, where the data taken on the Ni ($Z = 28$) and Sn ($Z = 50$) are compared. The population of the 4^+ state is reduced by a factor 2 relative to the 2^+ state when the nickel target is used, whereas the 3^- state, populated by a single-step $E3$ excitation, shows an increase in the relative population.

Segmentation into different angular ranges is possible due to the granularity of the CD detector. Recoil events occurring in the inner-most strips (low laboratory angle) of the detector correspond to high centre of mass scattering events, while the outer strips (high laboratory angle) contain scattering events at low centre of mass scattering angle. This provides two angular ranges for which the Coulomb excitation cross-section is sensitive, resulting in different level populations between the data sets. This is obvious in Figure 4.10 where the γ-ray intensities of the transitions are very different, especially for the states populated in multiple-step processes. For example, the $6^+ \to 4^+$ intensity is enhanced in the high centre of mass range due to the increased probability of multiple-step Coulomb excitation.

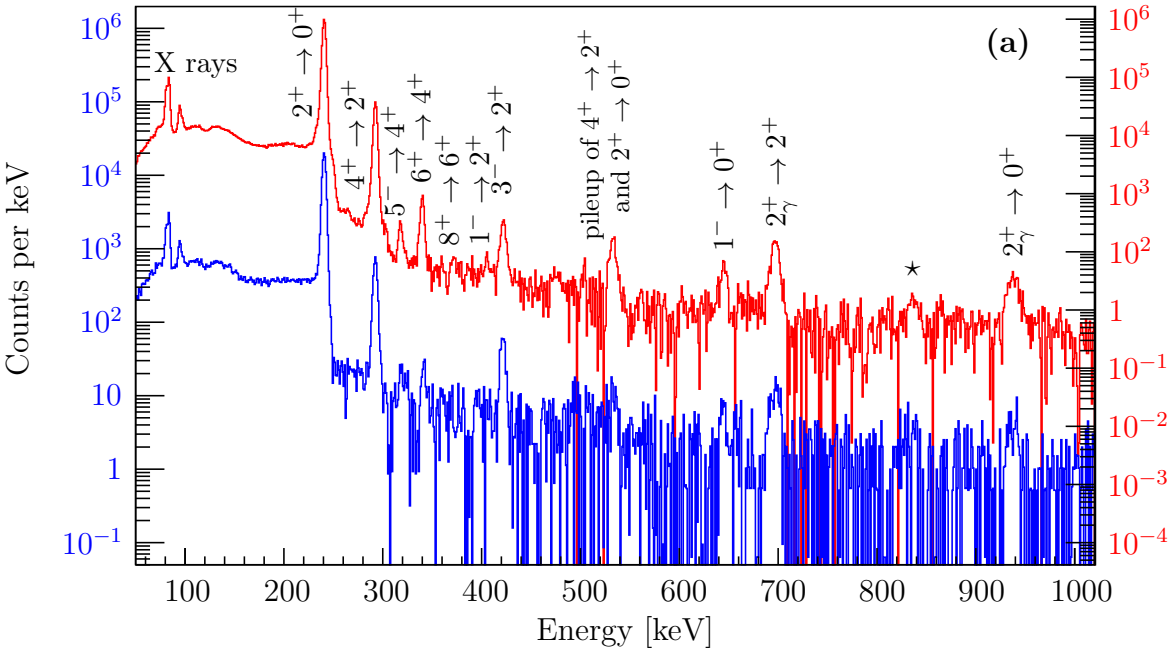

Figure 4.9: Comparison of Ni (blue) and Sn (red) targets with the ^{220}Rn beam. The peak marked with $\star$ is unplaced in the level scheme. The population of high-spin states is clearly reduced when the lower Z target (Ni) is used, see $6^+ \to 4^+$ intensity.

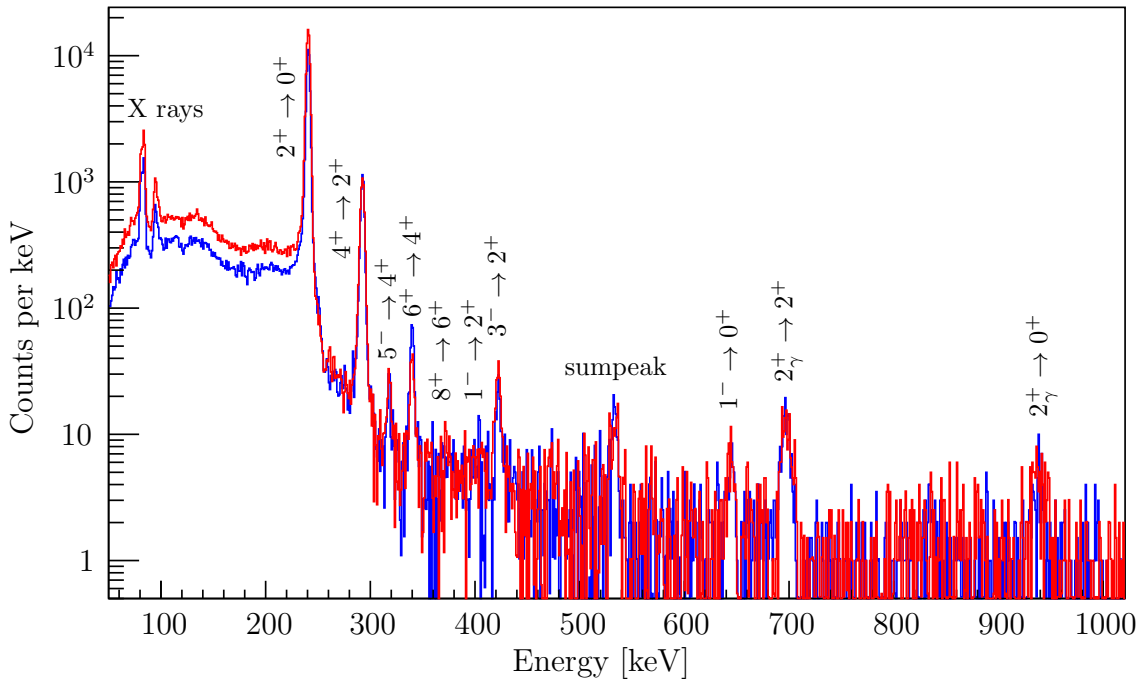

Figure 4.10: Comparison of high centre of mass (CoM) scattering angular range (blue) and low CoM angular range (red) with the ^{220}Rn beam on ^{120}Sn target. As with the change of target Z, the change in angle yields different cross sections for exciting states with the variation in intensities reflecting this.

4.3 Spectroscopy of ^{224}Ra via Coulomb excitation

There have been numerous studies of the level structure of ^{224}Ra in the past and as such, the level scheme is rather well determined at low-energy. Asaro, Stephens and Perlman [7] identified the first observed low-lying odd-spin states in this nucleus, back in 1953. Populating states in ^{224}Ra via the α decay of ^{228}Th [83], limits the number of levels that can be observed, however, β-decay of ^{224}Fr populates a large number of low-spin states [87], identifying, in particular, the excited 2^+ state assumed here to be the band-head of the $K = 2$ γ-vibrational band. Two-neutron pickup [28] and knockout [29] and most significantly, multi-nucleon transfer reactions [20], have placed the yrast levels up to $I^\pi = 26^+$ among others. A reduced level scheme showing the positive- and negative- parity band, and the vibrational level discussed in Section 4.3.1, is presented in Figure 4.11, where the level and γ-ray energies are extracted from Ref. [88].

The data is sorted in the same way as the ^{220}Rn data (see Section 4.2) and the particle-γ spectra, containing the total statistics, can be seen in Figure 4.12, while the γ-γ projection is presented in Figure 4.13. The $2^+ \rightarrow 0^+$ transition at 84.4 keV sits in the region of the x-rays, making it difficult to extract the intensity of the peak and forms a doublet with the 85.4 keV, $K_{\alpha 2}$ peak. Utilising the measured relative intensity to the $K_{\alpha 1}$ X rays [89], it is possible to fit all three peaks in question simultaneously, to extract the 84.4 keV yield. However, doing this requires the coupling over fit parameters such as the peak width, and the fixing of the centroid of the $K_{\alpha 2}$ peak. This introduces large uncertainties in the other, free parameters, specifically the peak area, leading to the rather large uncertainties for the yields of the $2^+ \rightarrow 0^+$ transition. Unfortunate as this is, the $4^+ \rightarrow 2^+$ transition is measured to better than 5% in all cases and provides a robust normalisation point for the GOSIA analysis of Section 5.2.2 when coupled with the precise ($\frac{\Delta\tau}{\tau} = 5\%$) lifetime of the 4^+ state. Since the lifetime of the 2^+ state is also independently measured with

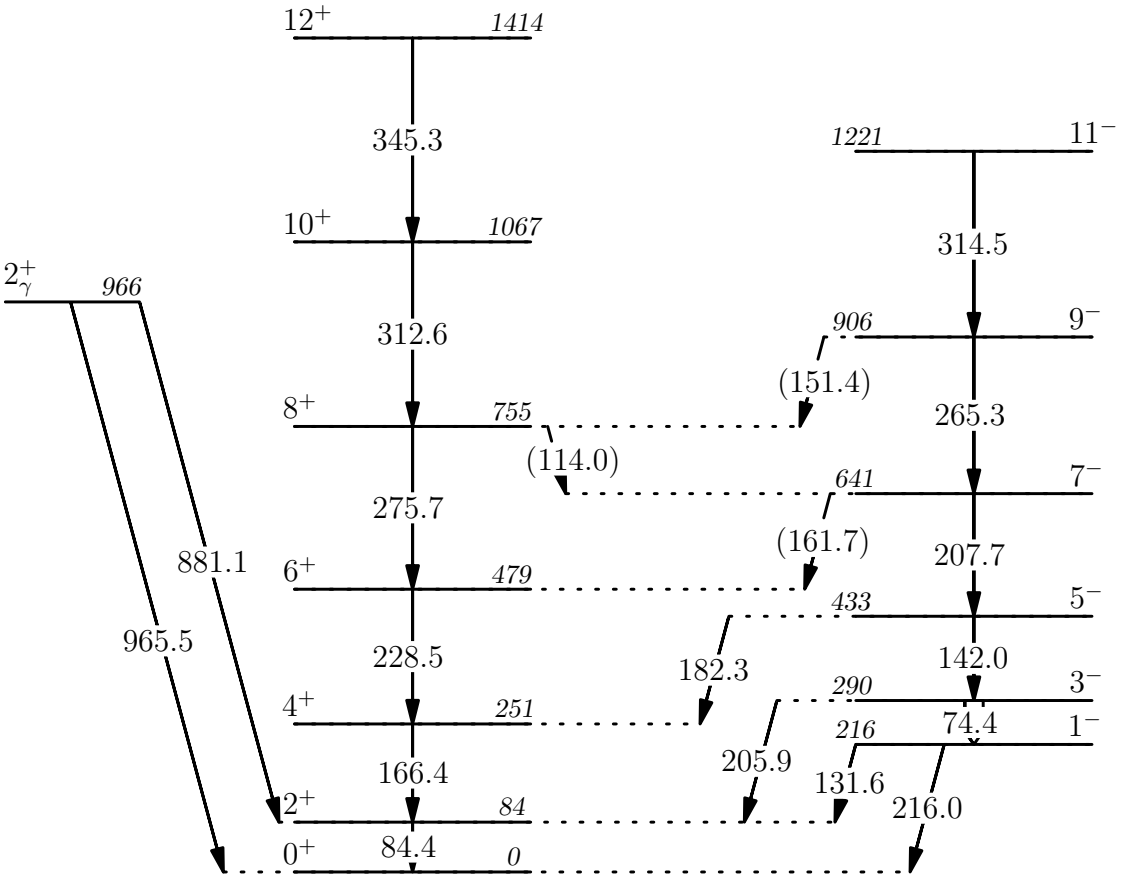

Figure 4.11: Reduced level scheme of ^{224}Ra.

a 3% uncertainty, the matrix element controlling the excitation to this state, namely $\langle 0^+||E2||2^+\rangle$, is determined without the requirement for precise yield measurements.

4.3.1 Vibrational states

A state has been observed at 965.5 keV in ^{224}Ra, both in this experiment and that of Kurcewicz *et. al* following the β decay of ^{224}Fr [87]. The spin and parity assignment in that experiment is given tentatively as $I^\pi = 2$ and is assumed to be the band-head of the $K = 2$ γ-vibrational band. Statistics for the two de-exciting transitions are not as high as for the similar state observed in ^{220}Rn (see Section 4.2.1), however, γ-γ coincidences do confirm the state's placement in the level scheme of Fig. 4.11. Further to this, the measured γ-ray branching ratio,

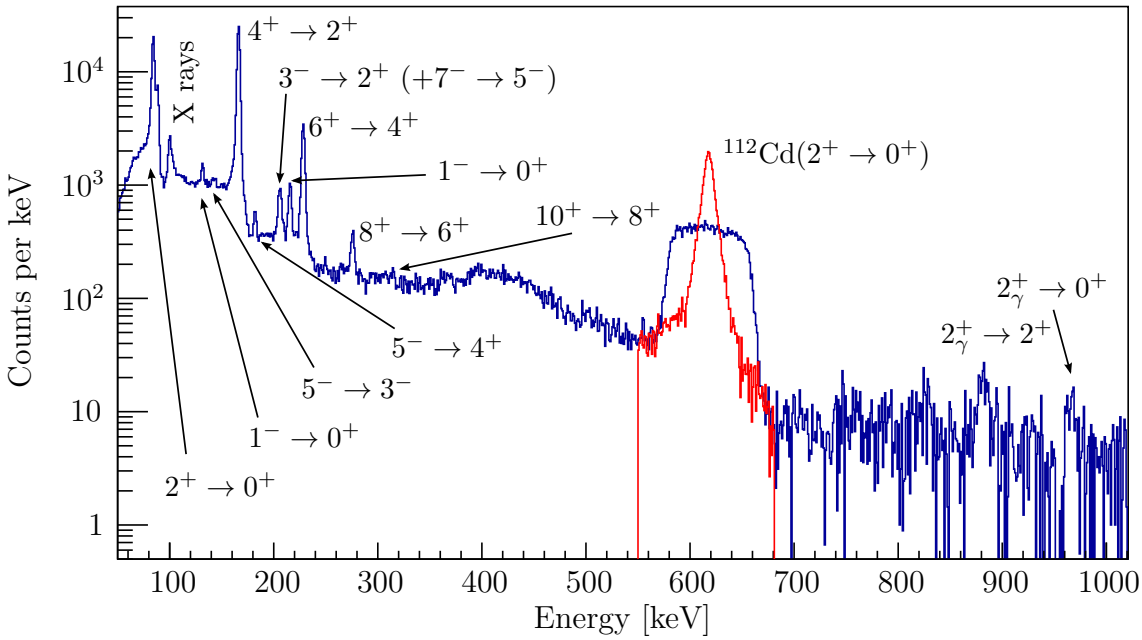

Figure 4.12: Gamma-ray spectrum of particle-γ singles events in ^{224}Ra, Doppler corrected and background subtracted. Transitions labeled were all previously observed. The broad peak around 600 keV is caused by the incorrect Doppler correction of the 617 keV, $2^+ \to 0^+$ transition, γ rays, emitted from the recoiling ^{112}Cd nucleus. The overlaid red line is a partial spectrum showing this transition, now Doppler corrected using the recoil kinematics.

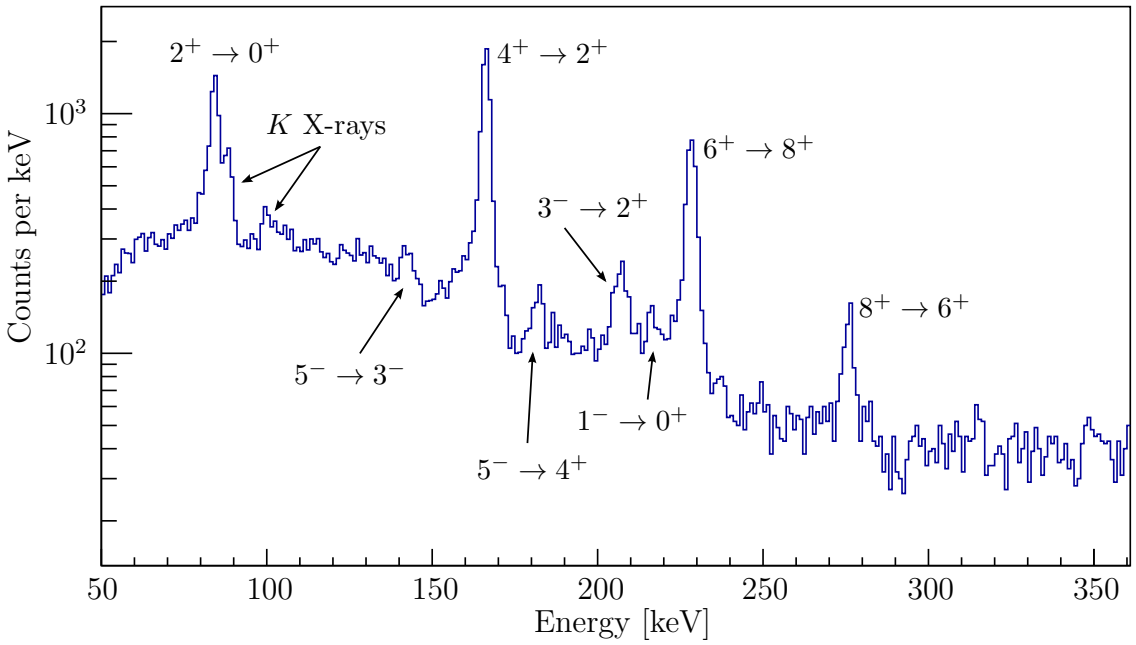

Figure 4.13: Projection of the particle-γ-γ matrix of events with the ^{224}Ra beam. The matrix is symmetrised with Doppler corrected events and those random in time are subtracted according to the ratio of the relative prompt/random window widths. The $1^- \to 0^+$ transition is suppressed relative the the nearby $3^- \to 2^+$ transition, reflecting the lower probability of detecting a coincident transition.

Table 4.2: γ-ray branching ratios in ^{224}Ra, measured in this work, compared with previous measurements, the predictions of the Alaga rules and the rotation-vibration model of Bohr and Mottelson, where appropriate.

State (I_i)	I_1	I_2	$Y_\gamma(I_i \to I_1)/Y_\gamma(I_i \to I_2)$			
			Experiment	Previous [88]	Alaga	Rot-Vib
2^+_γ	2^+	0^+	1.1 ± 0.4	1.67 ± 0.19	0.90	6.73
1^-	2^+	0^+	0.48 ± 0.05	0.515 ± 0.009	0.45	—
5^-	4^+	3^-	1.8 ± 0.4	4 ± 2	—	—

presented in Table 4.2, reproduces that expected from the Alaga rules [86] for a $\Delta K = 2$ transition and is also consistent with the previously measured value. Also, the limit given on the transition strength in Table 5.6 (< 3 W.u), is of the order that is expected for a $2^+_\gamma \to 0^+$ transition in this region. However, this is not strong enough evidence alone for a confident assignment of this state's configuration and therefore we rely on systematics of similar 2^+ states in this region to justify the $K = 2$ assignment for the purposes of this analysis.

4.3.2 Data segmentation

Just as with the ^{220}Rn data (see Section 4.2.2), the data is segmented (see Section 5.1 for details) to increase sensitivity to different excitation paths and therefore, better determine the matrix elements in the Coulomb excitation analysis of Chapter 5. Figure 4.14 contains the total statistics spectra for the Ni and Sn targets where the effect of changing the target Z on the multiple-step excitation probability, is clear.

The data is also segmented by scattering angle, using two recoil gates, one represent the higher laboratory (lab) angle or low centre of mass (CoM) angle and the other being the low lab and high CoM angle. These two data sets are compared for the ^{112}Cd target in Figure 4.15.

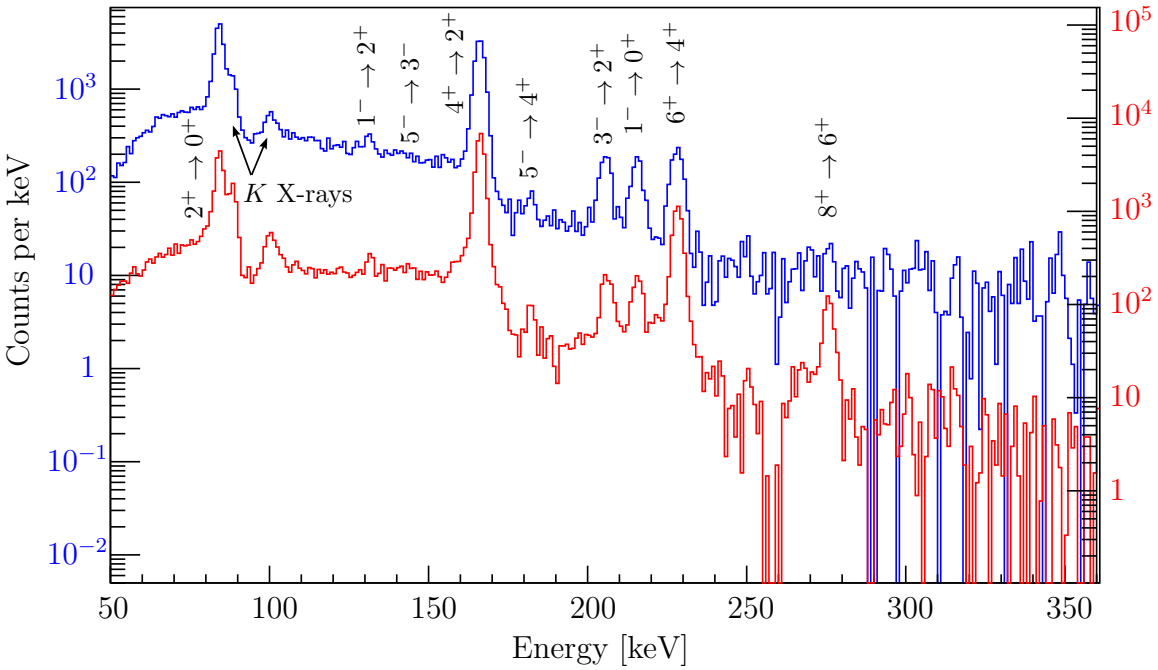

Figure 4.14: Comparison of Ni (blue) and Sn (red) targets with the ^{224}Ra beam. The population of high-spin states is clearly reduced when the lower Z target (Ni) is used, see $8^+ \to 6^+$ intensity.

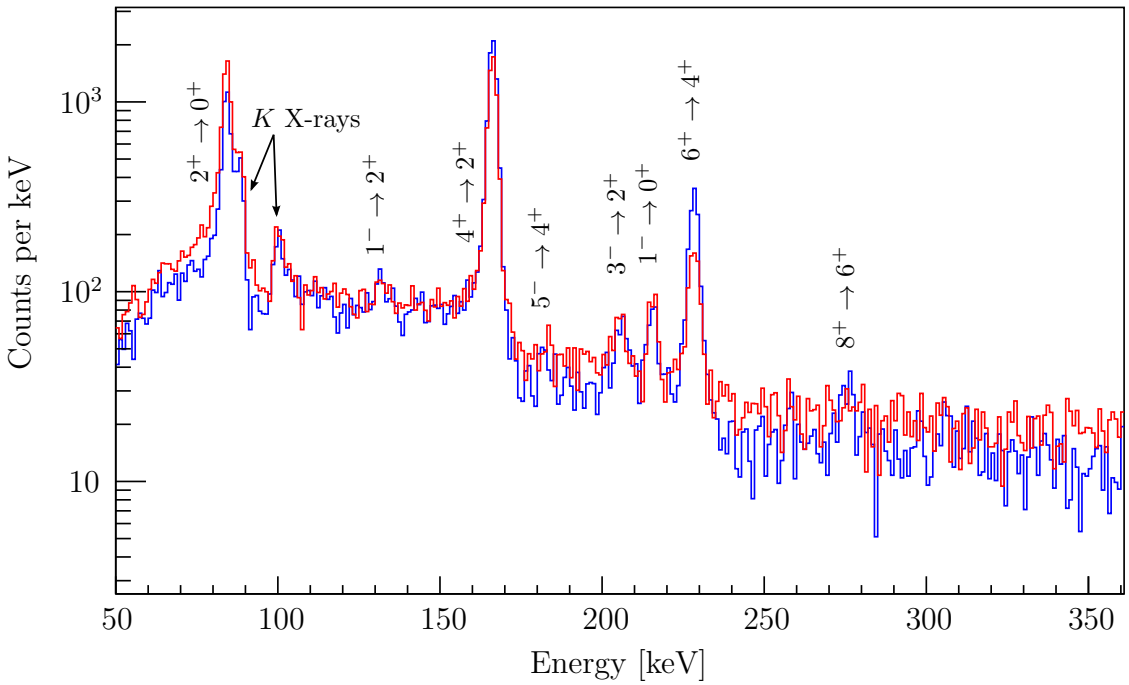

Figure 4.15: Comparison of high centre of mass (CoM) scattering angular range (blue) and low CoM angular range (red) with the ^{224}Ra beam on ^{114}Cd target. The probability of multiple-step Coulomb excitation increases with CoM scattering angle and this is observed with the relative population of the 6^+ and 8^+ states.

Chapter 5

Analysis and Results

The data is analysed using the GOSIA code, previously described in Section 2.2. GOSIA has been used similarly to extract $E2$ and $E3$ matrix elements in ^{148,150}Nd and ^{226}Ra [3, 23, 31, 90]. An explanation of the input required is presented in a detailed way in the manual [49]. Here, in Section 5.1, a summary of the important input will be presented along with a "recipe" of how the matrix elements are fit to the data in Section 5.2. Extraction of the statistical error on the fitted matrix elements is described in Section 5.3 and the further subsections describe methods used to ensure confidence in the final fit and estimate further systematic contributions to the uncertainties. The results of the final fits are presented for ^{220}Rn and ^{224}Ra in Sections 5.4 and 5.5, respectively.

5.1 Gosia Input

For the calculation of the excitation cross section, information on the beam and target species, along with beam energy and scattering angle, are required to determine the kinematics. Further to this, the nuclear-structure information, energy levels and matrix elements, of the nucleus to be studied must also be defined. The partner nucleus requires no structure information, since it is assumed that no mutual exci-

Table 5.1: Summary of GOSIA "experiments"

Projectile	Target (thickness)	Beam energy	Angular range (lab)	No.
^{220}Rn	^{114}Cd (2.0 mg/cm^2)	620.40 MeV	22.05°–37.75°	1
			37.86°–51.80°	2
	^{120}Sn (2.3 mg/cm^2)	620.40 MeV	22.05°–37.75°	3
			37.86°–51.80°	4
	^{60}Ni (2.1 mg/cm^2)	620.40 MeV	22.05°–37.75°	5
			37.86°–51.80°	6
^{224}Ra	^{112}Cd (2.0 mg/cm^2)	633.92 MeV	23.94°–40.32°	1
			40.43°–54.32°	2
	^{120}Sn (2.0 mg/cm^2)	633.92 MeV	23.94°–40.32°	3
			40.43°–54.32°	4
	^{60}Ni (2.1 mg/cm^2)	631.68 MeV	23.10°–39.87°	5
			39.30°–53.23°	6

tation takes place. All possible $E1$, $E2$, $E3$ and $E4$ couplings for yrast states up to $I^\pi = 12^+$ are included and initial values estimated using the rigid-rotor model of Equation 1.7 and Q_λ values extracted from known lifetimes or comparisons to previously measured matrix elements in the neighbouring nucleus, ^{226}Ra. It is imperative that higher, unobserved levels are included in the calculation since use of the coupled-channel system results in an overestimation of the transition amplitude to the final level.

The proposed γ-band, observed in both ^{224}Ra and ^{220}Rn, is included up to $I^\pi = 4^+$, where the unobserved 3^+_γ and 4^+_γ levels are included only for the reason already explained and are assumed to be situated 50 keV and 100 keV above the 2^+_γ state, respectively. The starting values for the matrix elements represent a ground state to 2^+_γ transition strength of 1 W.u. and are all coupled to this 1 free variable using Equation 1.7. $M1$ transitions are included to account for de-excitation of the vibrational states to the ground band, although these have no effect on the Coulomb excitation process.

Table 5.2: Additional spectroscopic data used in the GOSIA analysis.

Nucleus	Datum	Ref.	Notes
^{220}Rn	$\tau_{2^+} = 210.6(72)$ ps	[91, 92]	weighted average
	b.r.$(1^-) = 0.43(8)$	[80]	$\frac{I_\gamma(1^-\to2^+)}{I_\gamma(1^-\to0^+)}$
	b.r.$(5^-) = 4.1(14)$	[20]	$\frac{I_\gamma(5^-\to4^+)}{I_\gamma(5^-\to3^-)}$
	b.r.$(7^-) = 0.41(13)$	[20]	$\frac{I_\gamma(7^-\to6^+)}{I_\gamma(7^-\to5^-)}$
^{224}Ra	$\tau_{2^+} = 1073(27)$ ps	[92, 93]	weighted average
	$\tau_{4^+} = 261(13)$ ps	[92]	
	b.r.$(1^-) = 0.515(9)$	[88]	$\frac{I_\gamma(1^-\to2^+)}{I_\gamma(1^-\to0^+)}$
	b.r.$(3^-) = 50(20)$	[88]	$\frac{I_\gamma(3^-\to2^+)}{I_\gamma(3^-\to1^-)}$
	b.r.$(5^-) = 3.9(20)$	[88]	$\frac{I_\gamma(5^-\to4^+)}{I_\gamma(5^-\to3^-)}$
	b.r.$(7^-) = 0.133(43)$	[20]	$\frac{I_\gamma(7^-\to6^+)}{I_\gamma(7^-\to5^-)}$
	b.r.$(2^+_\gamma) = 1.67(19)$	[88]	$\frac{I_\gamma(2^+_\gamma\to2^+)}{I_\gamma(2^+_\gamma\to0^+)}$

The data in this thesis, described in Sections 4.2 and 4.3, was taken on three different targets and each was segmented into two angular ranges for recoil detection, thus there are six (semi-)independent data sets or "experiments" to be input, summarised in Table 5.1. The target thickness is defined using the incident and exit beam energy, calculated using SRIM [79], which in turn define the integration limits E_i and E_f. The angular range is defined using the recoil detection angles in the laboratory and is assumed to be symmetrical in ϕ, hence the integration limits in the centre of mass frame, $\Theta_{1,2}$, can be calculated by the code unambiguously.

For each experiment, the efficiency-corrected γ-ray intensity, or yield, together with the associated uncertainty, for every observed transition above a user-defined threshold is given in a separate file, read by the code at run time. The uncertainties given at this point include not only the statistical errors, encapsulating the effect of subtracting background events and cleanliness of the fitted peak, but also a factor which represents the uncertainty on the relative efficiency of the Miniball spec-

trometer. Proper treatment of the angular distribution also requires the detector geometries, including size and angle about the target position, which are determined in Section 3.2.4.

Previously measured spectroscopic properties are included as further data points and those used are given in Table 5.2 along with the appropriate references. These data are removed after the final fit to ensure that the results, and consequently the uncertainties, are independent of previous experiments. It is not possible to determine a fully independent fit in ^{224}Ra, however, as the lifetime of the 2^+ state is required to compensate for the large uncertainties on the $2^+ \rightarrow 0^+$ transition yields.

5.2 Fitting Procedure

An oversimplification of the procedure used to extract the matrix elements is to say that the code fits a number of parameters (the matrix elements) to reproduce the measured data (the γ-ray yields). The best solution is the one that produces the lowest total χ^2 (the S function, Eq 2.18). To be sure that the fit converges correctly, it needs to be over-defined and have more data than free parameters, especially in this case where the sensitivity to data or parameters can vary by many orders of magnitude. Free parameters aren't exclusive to the matrix elements. Since the γ-ray yields are only a relative measurement, a normalisation constant for each "experiment" is also required and in all cases outlined here. This normalisation is theoretically calculable for data segmented only by angular range, since the integrated beam current is equal and therefore the difference between them is only a factor related to the inelastic cross section. However, it is not possible to calculate this factor in the current version of GOSIA [49] and so these remain as free parameter in the fit. In the case that GOSIA is improved to allow this relative normalisation of experiments, the number of normalisation constants for each isotope studied would be three, instead of six, since each different target data-set would

require normalisation.

The least-squares search follows a procedure that needs to be optimised depending on the situation. A choice is made by the user whether to turn on or off certain features, including when to use the full calculation or the approximation, which can speed up or slow down the process of finding a minimum. This optimisation includes the possibility to switch between a steepest decent minimisation and a gradient plus derivative method, the latter of which uses the second-order information of the least-squared surface to better locate the direction of the search, especially when sharp valleys in the multi-parameter surface are present. These sharp valleys are common place in such analyses and are caused by strong correlations between two or more parameters, a feature of branching ratio data. The GOSIA manual [49] describes the numerical aspects in detail.

5.2.1 The ^{220}Rn Minimum

The final analysis of the ^{220}Rn data involved a total of 30 experimental yields for eight different transitions over six "experiments" (tabulated in Appendix B, Table B.1) plus the four additional spectroscopic data from Table 5.2, including the lifetime of first excited 2^+ state at 241 keV, known to 3.4% accuracy. Freely varying matrix elements total 15 (those of Table 5.5) while there are also six independent normalisation constants which are also varied in the fit.

Although there are 15 matrix elements varied in the fit, the rest are not fixed, but coupled to the nearest matrix element of the same multipolarity which is free and lower in energy. The coupling is such that the ratio of the two matrix elements gives the same intrinsic moment in the rigid-rotor model of Equation 1.7. Main examples of these coupled parameters are the diagonal matrix elements, discussed in Section 5.3.5, and the insensitive $E3$ matrix elements connecting high-lying excited levels in the band. In the first case, releasing the coupling can have an effect on the

fit, since the increase in the number of free parameters, and the relative sensitive nature of diagonal matrix elements (via the static quadrupole moment and the re-orientation effect [94]) allows for an unphysical reduction of the least-squares statistic per degree of freedom. In the latter case, the insensitivity of these matrix elements slows the fit down by increasing the parameter space unnecessarily. This reduction of parameters extends to higher-spin $E2$ matrix elements and all unobserved $E1$ and $E2$ transitions, whereas all $E4$ matrix elements are fixed throughout (see Section 5.3.4).

The results of the fit are presented in Section 5.4. The final uncertainties are calculated with all matrix-element couplings removed so as not to perturb the χ^2 surface. The least-squares statistic of Equation 2.18, S, for the final minimum is equal to 0.86.

Independence of the fit

It is crucial that the minimum taken as the best fit, is unique and not localised from a true, deeper minimum. To test this, and to be sure that the final fit is independent of the starting parameters, the input was randomised. The couplings were left in place, but all free parameters were given random starting values within reasonable limits. For example, in band, transitional $E2$ matrix elements could take a value between ± 9.9 eb and $E3$ matrix elements between ± 5.0 eb$^{\frac{3}{2}}$. An integration over energy and angle is performed using these random values and new correction factors obtained, before a new set of random matrix elements are calculated and many iterations of the fitting procedure ran. At this point, the χ^2 remains much higher than the point found at the suspected minima and since the matrix elements are now very different to those used for the calculation of the correction factors, a re-integration is performed. After this, the fit converged with only the relatively insensitive $E1$ matrix elements lying far from the values in the suspected minimum.

To solve this problem, parameters which control the fit were optimised to allow a large number of iterations of a small step size and the code was allowed to perform many hundreds of iterations before terminating. Doing this allowed the original minima to be reached, confirming the model-independent nature of the result.

The coupling of insensitive matrix elements could be seen as "model dependence" and so various coupling schemes were investigated. Predictably, the values of insensitive matrix elements do not impact on the fit and so too the coupling has no effect on the overall result. Only the relative phase of the matrix elements are fixed and remain a source of model dependence. This absolute sign is arbitrary and so, following the conventions of GOSIA, a positive matrix element is used to connect states whose wave functions have the same intrinsic phase, remembering that the sign of the Clebsch Gordan coefficient is negative when $I_f - I_i - \lambda < 0$. The assumption here is that all states within the octupole band have the same intrinsic phase. Switching the relative phase of the dipole and octupole moments is tested in Section 5.3.2.

5.2.2 The ^{224}Ra Minimum

The ^{224}Ra data analysis used a total of 48 experimental yields for ten different transitions over six "experiments" (tabulated in Appendix B, Table B.2) plus the seven additional spectroscopic data from Table 5.2. Of these data, the lifetimes of the first excited 2^+ state at 84.4 keV and 4^+ state at 250.7 keV, are measured with 2.5% and 5% uncertainty, respectively. A total of 16 matrix elements (those of Table 5.6) are varied in the fitting procedure along with six normalisation constants.

The investigation of the minimum followed in the same way as ^{220}Rn (Section 5.2.1), including the technique used to ensure the independence of the fit. The final uncertainties are calculated with the all matrix-element couplings removed. In testing the independence of the fit, all additional spectroscopic data was removed with the exception of τ_{2^+}, which is required to compensate for the contamination of

the $2^+ \rightarrow 0^+$ peak due to the X rays. The results of the fit are presented in Section 5.5. The least-squares statistic, S, for the final minimum is equal to 0.55.

5.3 Error Analysis

Usually, the uncertainties from a multi-parameter, least-squares fit would be estimated using a curvature matrix or by finding the width about the minima where the normalised χ^2 increases by unity. The former method cannot be applied here for many reasons, notably that the assumption of quadratic behaviour in χ^2 is not valid for Coulomb excitation data and that the gradient of this curve may never truly reach zero. This imperfection in the fit is not a problem for the determination of the central values of the parameters which are sensitive to the fit, but an unreasonably large number of iterations to insignificant parameters is required to reach a "perfect" minimum. The $\chi^2 + 1$ method implies that all parameters have equal or at least similar significance, whereas the nuclear matrix elements, which are the fit parameters in this case, can vary by many orders of magnitude in their sensitivity to the data.

5.3.1 Statistical Errors

For the reasons discussed, a method of estimating the statistical errors in Coulomb excitation analyses that does not require the assumption of quadratic behaviour of χ^2 or a perfect minimum, has been developed by Lesser and Cline [95, 96]. A full derivation of this method can be found in the GOSIA manual [49], along with the numerical estimations used by the GOSIA code. Here, a simplified description of the process used to determine an error estimation, is given.

Diagonal Errors

The error calculation is separated into two steps to manage the computation time and provide a method of determining the quality of the fit. The first step is the calculation of the diagonal errors, or the error on a single matrix element whilst all others are kept fixed. This can be used to ensure that the error bars of all sensitive matrix elements are close to symmetric as dramatic asymmetries at this point is an indicator that the true minimum is not yet achieved. The code also checks whether the least-squares statistic, S, improves significantly during this one-dimensional scan of the parameter space and prints a message to the user making it easier to predict where a better solution may lie.

Correlated Errors

A full calculation of the errors relies on knowledge of the sensitivity of a given matrix element; information which is obtained from the diagonal error estimation. This information is also used to define a "maximum correlation curve", that is, a direction in the parameter space whereby a change in χ^2 when changing a given parameter is offset to the maximum degree by changes in other, correlated parameters. Scanning along the line of this path for a given matrix element, while allowing all other matrix elements to vary, reproducing a minimum S, χ^2 is evaluated. The positive and negative values at which the integral becomes 68.3% of the total range, up to a maximum/minimum value determined from the diagonal calculation, is used as the estimate of the uncertainty on the matrix element in question.

5.3.2 $E1/E3$ relative phase

Coulomb excitation experiments are sensitive to the relative phase of the $E1/E3$ moments [97]. Using, in principle, the same technique as Amzal *et al.*, [97], the population of the 3^- state in ^{224}Ra was calculated assuming different signs of the

product of Q_1 and Q_3 as defined in the rotational model. The sensitivity becomes significant only at high centre-of-mass scattering angles, and Experiments 1, 3 and 5 of Table 5.1 show a variation between the positive and negative solutions of less than 10% in the population of the 3^- state.

Changes in the magnitude of the $E1$ and $E3$ matrix elements wash away any small changes in level population and therefore, both solutions must be considered and the differences in the resulting matrix elements factored into the overall uncertainty. The differences between the two solutions, presented in Table 5.4, is small and the χ^2 of the final fit is almost identical. Here, the assumption is that the relative phase is positive, since there clearly isn't sufficient sensitivity to distinguish between the two solutions.

In ^{220}Rn, the effect is smaller and the difference between the two solutions where $Q_1 \cdot Q_3 > 0$ and $Q_1 \cdot Q_3 < 0$ is $< 1\%$ for the population of the 3^- state. However, a variation in the matrix elements is still observed and included as a systematic error in Table 5.4.

5.3.3 Beam energy and target thickness

There can be a systematic error introduced due to the uncertainty in the beam energy ($\pm 0.7\%$ [64]) and target thickness (assumed to be ± 0.1 mg/cm^2). Since GOSIA does not account for these sources of error in the matrix elements, and no simple relationship exists between the measured matrix elements and experimental factors such as beam energy, a brute force investigation is required to determine the magnitude of the uncertainty in the results.

By using the extremes of beam energy and target thickness at 3σ to define the incoming and exit beam energies, an estimation of the systematic uncertainty in the matrix elements can be obtained. Here, the largest increase in cross-section would come from a thick target and high beam energy, whereas the lower limit of the

Table 5.3: Effect of different assumptions on matrix elements in ^{220}Rn. The table shows percentage differences in the matrix elements found at the two different chi-squared minima in each case. The first column refers to $E1/E3$ relative phase effects, the second column to beam energy and target thickness errors and the third column to diagonal matrix element assumptions.

Matrix Element	$Q_1 \cdot Q_3$ % diff.	$\uparrow$ / $\downarrow$ XS % diff. / $2\sqrt{2}$	DME % diff.
$\langle 0^+ \| \| E1 \| \| 1^- \rangle$	0.25	0.23	5.6
$\langle 2^+ \| \| E1 \| \| 1^- \rangle$	0.23	0.19	5.6
$\langle 2^+ \| \| E1 \| \| 3^- \rangle$	0.17	0.7	59
$\langle 4^+ \| \| E1 \| \| 5^- \rangle$	2.5	2.5	6.2
$\langle 6^+ \| \| E1 \| \| 7^- \rangle$	2.0	2.3	8.1
$\langle 0^+ \| \| E2 \| \| 2^+ \rangle$	0.10	0.0008	1.2
$\langle 2^+ \| \| E2 \| \| 4^+ \rangle$	0.012	1.4	0.002
$\langle 4^+ \| \| E2 \| \| 6^+ \rangle$	0.8	2.4	0.73
$\langle 1^+ \| \| E2 \| \| 3^+ \rangle$	0.08	2.6	9.5
$\langle 3^+ \| \| E2 \| \| 5^+ \rangle$	0.08	2.6	9.5
$\langle 0^+ \| \| E2 \| \| 2^+_\gamma \rangle$	2.3	2.3	21
$\langle 0^+ \| \| E3 \| \| 3^- \rangle$	1.3	1.7	8
$\langle 2^+ \| \| E3 \| \| 1^- \rangle$	1.8	2.7	9
$\langle 2^+ \| \| E3 \| \| 3^- \rangle$	2.6	1.7	3.1
$\langle 2^+ \| \| E3 \| \| 5^- \rangle$	2.6	2.8	3.1

cross-section is represented by a combination of a thin target and a reduced beam energy.

The average difference between the values of each matrix element at these two solutions is used to calculate the systematic error, i.e $|ME_i^{\uparrow} - ME_i^{\downarrow}|/2\sqrt{2}$. The factor $\sqrt{2}$ is intended to account for the lack of proper quadratic addition of the two extremes in beam energy and target thickness.

As can be seen in Tables 5.3 and 5.4, also Figures 5.1, 5.2 and 5.3 for ^{224}Ra, the effect is larger as spin increases due to the multiplicative effect of under- or over-estimating the population of each intermediate state in multiple excitation.

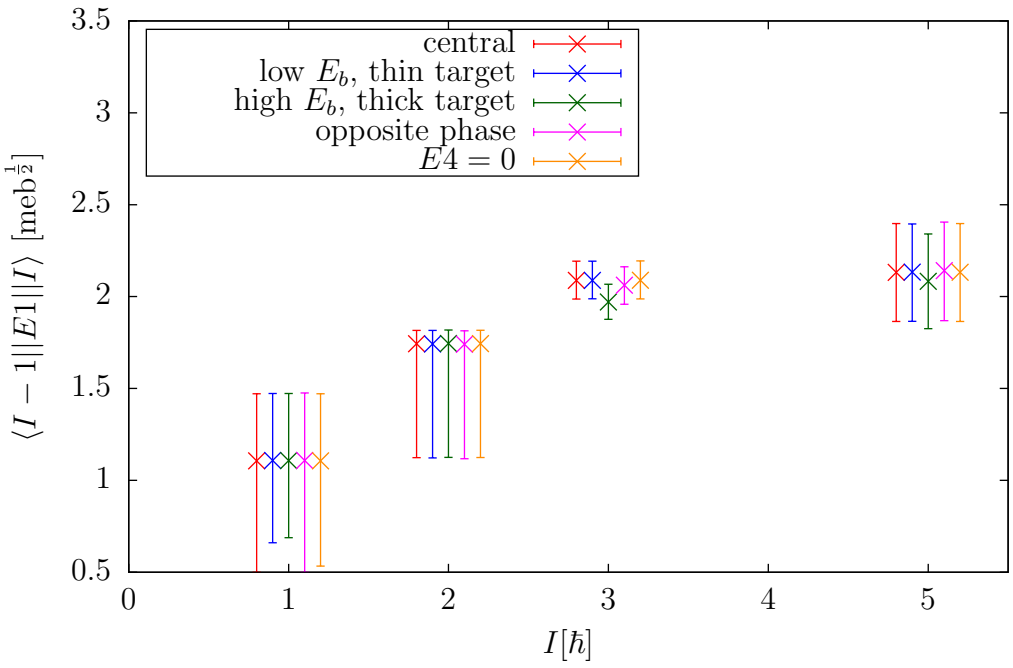

Figure 5.1: Magnitude of E1 matrix elements extracted from GOSIA assuming different beam energy and target thickness conditions. The uncertainties represent the initial statistical errors, uncorrected for the coupling of matrix elements. See Section 5.3.3 for details

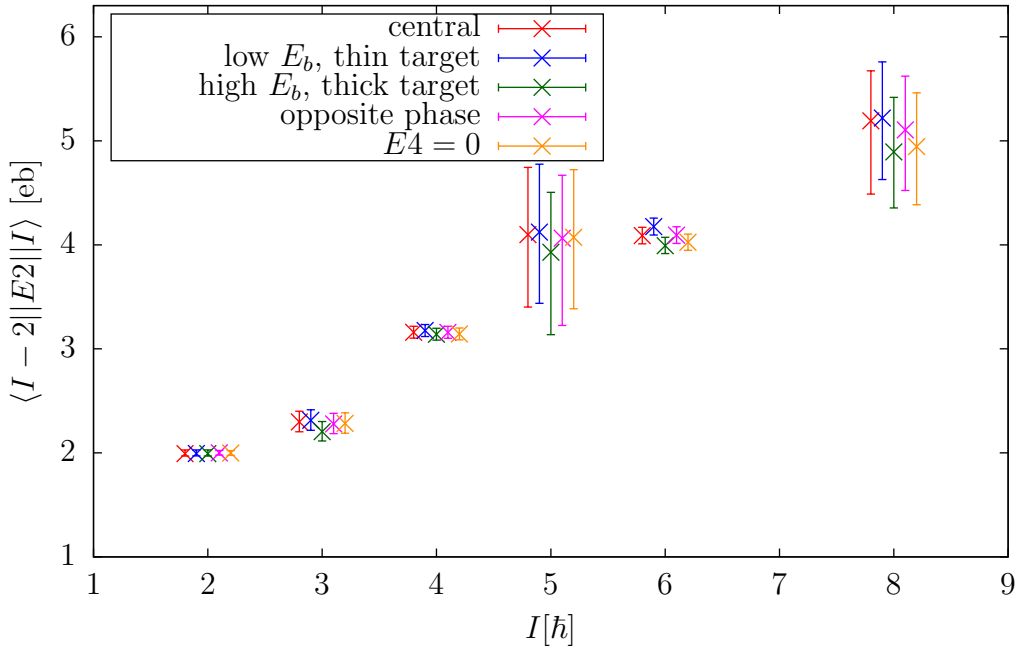

Figure 5.2: Similar to Fig. 5.1 but for E2 matrix elements.

Table 5.4: Effect of different assumptions on matrix elements in ^{224}Ra. The table shows percentage differences in the matrix elements found at the two different chi-squared minima in each case. The first column refers to $E1/E3$ relative phase effects, the second column to beam energy and target thickness errors and the third column refers to the effect of switching of $E4$ matrix elements.

Matrix Element	$Q_1 \cdot Q_3$ % diff.	$\uparrow$ / $\downarrow$ XS % diff. / $2\sqrt{2}$	$E4 = 0$ % diff.
$\langle 0^+ \| \| E1 \| \| 1^- \rangle$	0.0	0.0	0.0
$\langle 2^+ \| \| E1 \| \| 1^- \rangle$	0.0	0.0	0.0
$\langle 2^+ \| \| E1 \| \| 3^- \rangle$	1.5	2.0	0.0
$\langle 4^+ \| \| E1 \| \| 5^- \rangle$	0.5	0.8	0.0
$\langle 6^+ \| \| E1 \| \| 7^- \rangle$	0.3	1.6	0.0
$\langle 0^+ \| \| E2 \| \| 2^+ \rangle$	0.4	0.02	0.3
$\langle 2^+ \| \| E2 \| \| 4^+ \rangle$	0.04	0.4	0.5
$\langle 4^+ \| \| E2 \| \| 6^+ \rangle$	0.11	1.6	1.6
$\langle 6^+ \| \| E2 \| \| 8^+ \rangle$	1.7	2.2	5.0
$\langle 1^+ \| \| E2 \| \| 3^+ \rangle$	0.9	1.5	0.7
$\langle 3^+ \| \| E2 \| \| 5^+ \rangle$	0.8	1.7	0.6
$\langle 0^+ \| \| E2 \| \| 2^+_\gamma \rangle$	0.12	14.7	1.2
$\langle 0^+ \| \| E3 \| \| 3^- \rangle$	0.8	0.22	0.9
$\langle 2^+ \| \| E3 \| \| 1^- \rangle$	0.6	1.5	1.4
$\langle 2^+ \| \| E3 \| \| 3^- \rangle$	0.07	12.4	0.4
$\langle 2^+ \| \| E3 \| \| 5^- \rangle$	2.0	2.0	0.6

5.3.4 $E4$ matrix elements

It is clear that, in this region of the nuclear chart, there is a non-zero value for the electric hexa-decapole ($E4$) matrix elements. A measurement of $B(E4; 4^+ \rightarrow 0^+)$ has been made in the neighbouring ^{226}Ra [3]. From this, it is possible to extract a hexa-decapole moment ($Q_4 = 2.55(35)$ eb^2) assuming the nucleus behaves like a rigid rotor.

During the GOSIA investigation, it was very clear that the data from this experiment lacked sensitivity to the $E4$ matrix elements (1σ error bars $> 200\%$ for

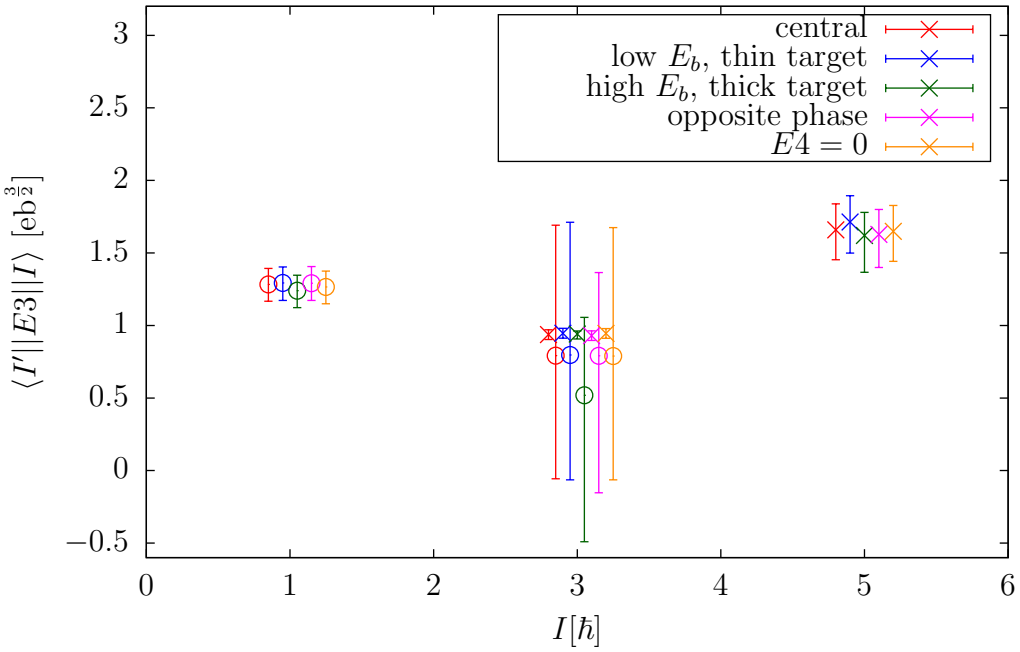

Figure 5.3: Similar to Fig. 5.1 but for E3 matrix elements. Stretched, $I' = I - 3$, and unstretched, $I' = I - 1$, matrix elements are represented by crosses ($\times$) and open circles ($\circ$), respectively.

example), and so the assumption that Q_4 is equal in ^{224}Ra and ^{226}Ra is used. For ^{220}Rn, the simple assumption that $\frac{Q_4(^{226}\mathrm{Ra})}{Q_4(^{220}\mathrm{Rn})} = \frac{\beta_4(^{226}\mathrm{Ra})}{\beta_4(^{220}\mathrm{Rn})}$ holds true is used. The measured Q_4 value is taken from Ref. [3] and theoretical β values from Ref. [13]. Since the resulting $E4$ matrix elements are so small, their effect is negligible.

All $E4$ matrix elements are calculated from the rigid-rotor formula and kept fixed during the analysis with diagonal matrix elements fixed to be 0 eb^2. To test the effect of this assumption on the ^{224}Ra fit, another fit was performed with all $E4$ matrix elements equal to zero and the result is shown in Column 4 of Table 5.4. Since the $E4$ matrix elements in ^{220}Rn are so small, their effect is neglected in the calculation of the uncertainties.

5.3.5 Diagonal $E2$ matrix elements

The diagonal $E2$ matrix elements represent the spectroscopic quadrupole moment of a state. In this experiment, there is not sufficient sensitivity (uncertainties $> 200\%$) to the matrix elements to allow them to vary as free parameters and so they are coupled to the corresponding transitional $E2$ matrix element which depopulates the state. To do this, it is necessary to assume a ratio obtained from model dependence, in this case the rigid-rotor model. States in ^{224}Ra are assumed to behave like a perfect rigid rotor as, to good approximation, so too does ^{226}Ra. Also, the ratio $B_{4/2}$ (according to Equation 1.11) is very close to the rigid-rotor value of 1.43.

This cannot be assumed with such confidence in ^{220}Rn since the $B(E2; 4^+ \rightarrow 2^+)$ value is not known and the $E(4^+)/E(2^+)$ implies less collectivity than the higher-mass radon isotopes. Initial values can still be obtained from the rigid-rotor model as the $B(E2; 2^+ \rightarrow 0^+)$ is known from the measured lifetime of the 2^+ state and the effect on the final fit assuming different values for the diagonal $E2$ matrix elements (DMEs), investigated.

Three simple conditions are used to investigate the magnitude of this effect on the measured matrix elements. All DMEs are coupled to the nearest, freely varying, transitional $E2$ matrix element below the state and the ratio fixed to the ratio of the rigid-rotor prediction. The DMEs are then either positive, negative or zero. The chi-squared value is lowest for the negative solution and highest for the positive. The absolute difference between these two solutions is considered an additional systematic error and is presented in Table 5.3.

5.4 ^{220}Rn Results

All sensitive matrix elements in ^{220}Rn that were allowed to vary in the fit and represent a real, physical measurement are presented in Table 5.5. For example,

Table 5.5: Magnitude of measured matrix elements in ^{220}Rn, extracted from the GOSIA analysis. Error bars represent 1σ while limits are 3σ.

Matrix elements [efm$^\lambda$]		$B(E\lambda)\downarrow$ [W.u.]	Q_λ [efm$^\lambda$]
$\langle 0^+ \| \| E1 \| \| 1^- \rangle$	< 0.10	$< 1.5 \times 10^{-3}$	< 0.02
$\langle 2^+ \| \| E1 \| \| 1^- \rangle$	< 0.13	$< 3 \times 10^{-3}$	< 0.019
$\langle 2^+ \| \| E1 \| \| 3^- \rangle$	< 0.18	$< 2 \times 10^{-3}$	< 0.02
$\langle 4^+ \| \| E1 \| \| 5^- \rangle$	0.028 ± 0.009	$3.0^{+2}_{-1.6} \times 10^{-5}$	$2.6 \pm 0.8 \times 10^{-3}$
$\langle 6^+ \| \| E1 \| \| 7^- \rangle$	< 1.3	< 0.5	< 0.10
$\langle 0^+ \| \| E2 \| \| 2^+ \rangle$	137 ± 4	48 ± 3	434 ± 14
$\langle 2^+ \| \| E2 \| \| 4^+ \rangle$	212 ± 4	63 ± 3	419 ± 9
$\langle 4^+ \| \| E2 \| \| 6^+ \rangle$	274 ± 14	73 ± 8	429 ± 20
$\langle 1^- \| \| E2 \| \| 3^- \rangle$	180 ± 60	60^{50}_{30}	420 ± 150
$\langle 3^- \| \| E2 \| \| 5^- \rangle$	220 ± 150	60^{100}_{50}	400 ± 300
$\langle 0^+ \| \| E2 \| \| 2^+_\gamma \rangle$	32 ± 7	2.6 ± 1.1	100 ± 20
$\langle 0^+ \| \| E3 \| \| 3^- \rangle$	810 ± 50	33 ± 4	2180 ± 130
$\langle 2^+ \| \| E3 \| \| 1^- \rangle$	< 2600	< 760	< 6000
$\langle 2^+ \| \| E3 \| \| 3^- \rangle$	< 5300	< 1400	< 12000
$\langle 2^+ \| \| E3 \| \| 5^- \rangle$	1700 ± 400	90 ± 50	3000 ± 700

the $\langle 2^+ \| \| M1 \| \| 2^+_\gamma \rangle$ value is not presented since this is related to $\langle 2^+ \| \| E2 \| \| 2^+_\gamma \rangle$ via the mixing ratio which is undetermined in the fit and hence, is not truly measured. It is left free, however, as it is sensitive to the branching ratio to the decay to the 0^+ ground state, a data point which must be fit since both decays are observed.

It is possible to calculate the transition multipole moments for each measured matrix element, assuming the rigid-rotor model of Equation 1.7. These have been plotted as a function of the initial spin, I_i, for each of the dipole, quadrupole and octupole moments in Figure 5.4. A straight line has been drawn which represents the weighted average of these values, assuming Q_λ is independent of spin. This assumption seems consistent with the data, although there are only two measurements of Q_3, which is not enough to draw conclusions on rigid-rotor behaviour since similar behaviour can be explained with the coupling of a octupole phonon to a rotational band, as will be explained in Section 6.2.

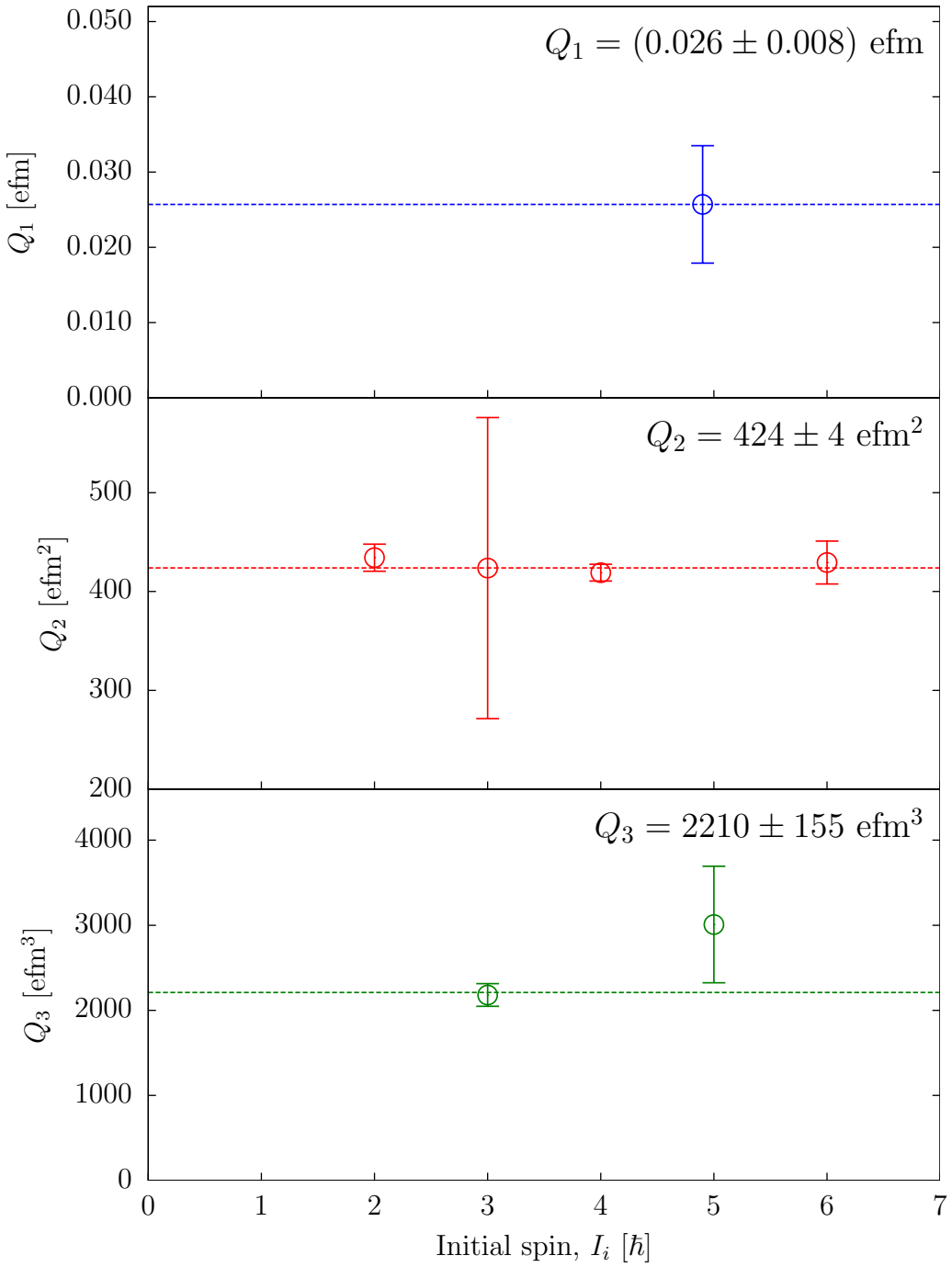

Figure 5.4: Transition moments, Q_λ, in ^{220}Rn as a function of spin, extracted using Equation 1.7. The weighted average is represented by the corresponding dashed lines.

A strong indicator of the independence of this measurement comes in the reproduction of the measured τ_{2^+} [91, 92] when all additional spectroscopic data points are removed from the GOSIA fit. The uncertainties presented in Table 5.5 are independent of these data and represent only the sensitivity to, and statistical uncertainties of the measurements in this thesis, plus the systematic errors of Table 5.3. In addition, lifetimes of the 4^+ and 6^+ states can now be calculated as 66 ± 3 ps and 28 ± 3 ps, respectively.

The state at 939 keV, with proposed $(I^\pi, K) = (2^+, 2)$, has a transition strength measured to be 2.7(11) W.u., which is similar to the value of 2.9(3) W.u. measured in ^{230}Th [98] and 3.47(17) W.u. in ^{232}Th [99] for the respective states in those nuclei.

5.5 ^{224}Ra Results

The final extracted matrix elements in ^{224}Ra are presented in Table 5.6. The uncertainties reflect the sensitivity to the matrix elements, the systematic errors outlined in Table 5.4 and the statistical error, without the inclusion of additional spectroscopic data outlined in Table 5.2. The one exception to this is τ_{2^+}, which is included to account for the large uncertainties on the γ-ray yield, therefore $\langle 0^+||E2||2^+\rangle$ is not an independent measurement.

It has been shown that the 4^+ lifetime, previously measured by Neal and Kraner [92] ($\tau_{4^+} = 261(13)$ ps), is consistent with the analysis here under all circumstances. This data point is therefore used to attest to the validity of the analysis procedure and the independence of the results. Using the $B(E2)$ values in Table 5.6, lifetimes for the even-spin states that have not yet been measured, assuming the decay branch is 100% $E2$, are calculated as $\tau_{6^+} = 76 \pm 6$ ps and $\tau_{8^+} = 30^{-7}_{+8}$ ps.

The transition multipole moments for each measured matrix element, assuming the rigid-rotor model of Equation 1.7 have been calculated and plotted as a function of initial spin in Figure 5.5. The assumption that Q_λ is independent of spin

Table 5.6: Magnitude of measured matrix elements in ^{224}Ra, extracted from the GOSIA analysis. Error bars represent 1σ while limits are 3σ.

Matrix elements [efm$^\lambda$]		$B(E\lambda)\downarrow$ [W.u.]	Q_λ [efm$^\lambda$]
$\langle 0^+ \| \| E1 \| \| 1^- \rangle$	< 0.018	$< 1.5 \times 10^{-3}$	< 0.02
$\langle 2^+ \| \| E1 \| \| 1^- \rangle$	< 0.03	$< 3 \times 10^{-3}$	< 0.019
$\langle 2^+ \| \| E1 \| \| 3^- \rangle$	0.026 ± 0.005	$3.9^{+1.7}_{-1.4} \times 10^{-5}$	$3.0 \pm 0.6 \times 10^{-3}$
$\langle 4^+ \| \| E1 \| \| 5^- \rangle$	0.028 ± 0.009	$3.0^{+2}_{-1.6} \times 10^{-5}$	$2.6 \pm 0.8 \times 10^{-3}$
$\langle 6^+ \| \| E1 \| \| 7^- \rangle$	< 0.10	$< 3 \times 10^{-4}$	< 0.10
$\langle 0^+ \| \| E2 \| \| 2^+ \rangle$	199 ± 3	98 ± 3	632 ± 10
$\langle 2^+ \| \| E2 \| \| 4^+ \rangle$	315 ± 6	137 ± 5	623 ± 11
$\langle 4^+ \| \| E2 \| \| 6^+ \rangle$	405 ± 15	156 ± 12	630 ± 20
$\langle 6^+ \| \| E2 \| \| 8^+ \rangle$	500 ± 60	180 ± 60	660 ± 80
$\langle 1^- \| \| E2 \| \| 3^- \rangle$	230 ± 11	93 ± 9	540 ± 30
$\langle 3^- \| \| E2 \| \| 5^- \rangle$	410 ± 60	190 ± 60	710 ± 110
$\langle 0^+ \| \| E2 \| \| 2^+_\gamma \rangle$	23 ± 4	1.3 ± 0.5	73 ± 12
$\langle 0^+ \| \| E3 \| \| 3^- \rangle$	940 ± 40	42 ± 3	2520 ± 90
$\langle 2^+ \| \| E3 \| \| 1^- \rangle$	1370 ± 140	210 ± 40	3200 ± 300
$\langle 2^+ \| \| E3 \| \| 3^- \rangle$	< 4000	< 600	< 8000
$\langle 2^+ \| \| E3 \| \| 5^- \rangle$	1410 ± 19	61 ± 17	2400 ± 300

fits well to the data, especially in the case of quadrupole deformation, where the transition, or intrinsic, quadrupole moments, measured up to $I^\pi_i = 8^+$, are consistent with a weighted average of $Q_2 = 624(10)$ efm^2. However, the quadrupole moment calculated from $\langle 3^- \| \| E2 \| \| 5^- \rangle$ implies a drop in collectivity for the odd-spin, negative-parity states. The large uncertainty on this value, and the lack of more data points, may not be enough to draw definitive conclusions on the differences between the odd- and even-spin structures, however, a similar feature is seen in the neighbouring ^{226}Ra [3].

The octupole moments, Q_3, shown in the bottom panel of Fig. 5.5, also follow the prediction of the rigid-rotor model. This may imply that the odd-spin, negative-parity states are coupled rotationally to the ground-band, even-spin states (see Section 6.1).

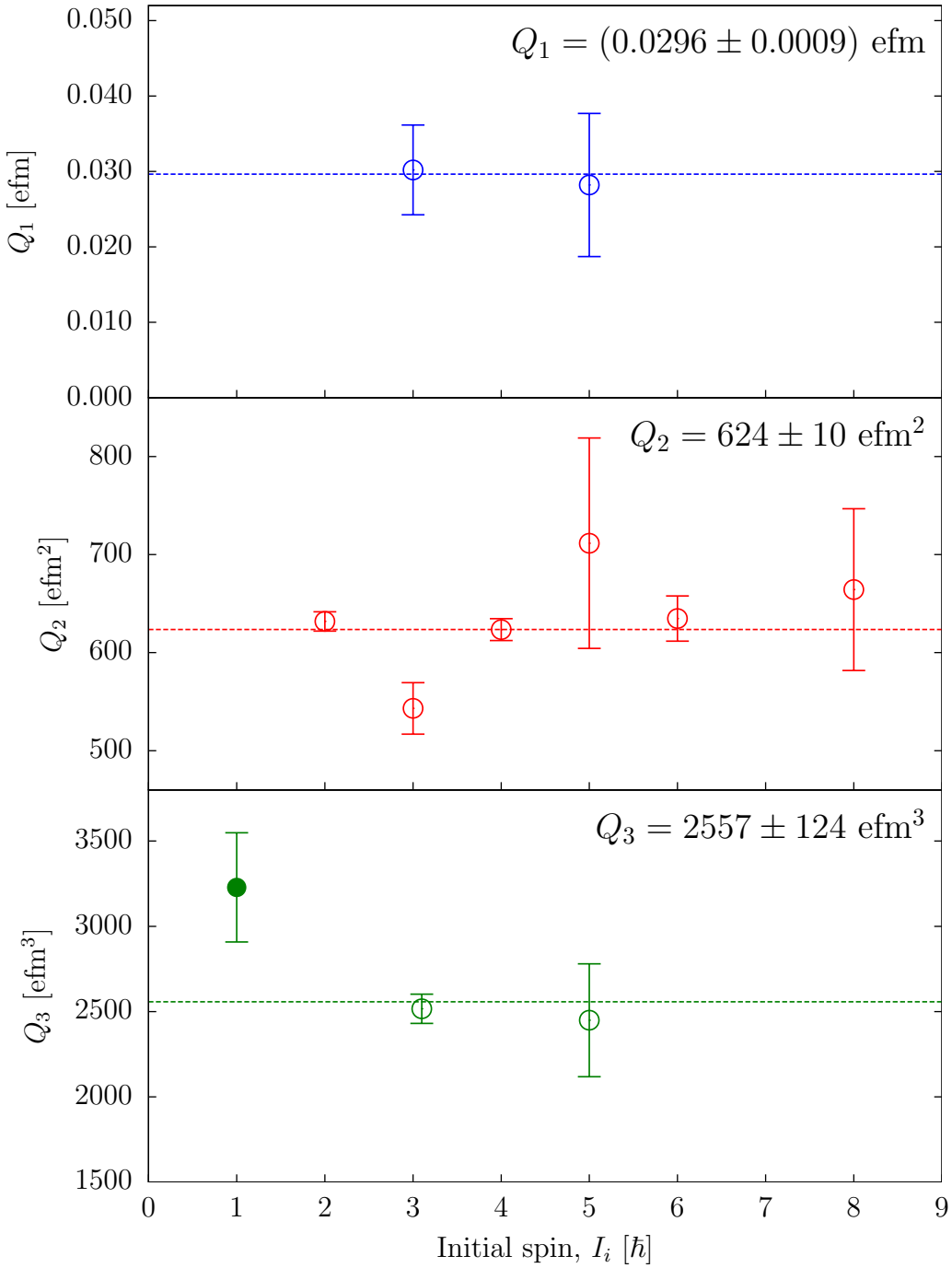

Figure 5.5: Same as Figure 5.4, but showing transition moments in ^{224}Ra. Values calculated from unstretched $E3$ matrix elements, i.e. $\langle I_i^{-\pi} \pm 1||E3||I_i^{\pi}\rangle$, are represented by filled circles.

Chapter 6

Discussion

The results presented in the previous chapter, Tables 5.5 and 5.6, show that sensitivity to the $E3$ matrix elements can be achieved using Coulomb excitation of post-accelerated radioactive ion beams (RIB). This sensitivity is demonstrated in a GOSIA simulation of the ^{224}Ra experiment (see Figure 6.1), where the $E3$ matrix elements are switched off and the resulting γ-ray yields are compared. The population of the odd-spin negative-parity states are shown to be strongly dependent on the octupole coupling, allowing for the determination of $B(E3; 3^- \rightarrow 0^+)$ with less than 10% precision.

To help interpret the multipole moments, it is useful to calculate the β_λ deformation parameters. These are evaluated numerically using Equations 1.3 to 1.6 (assuming $\beta_5, \beta_6 = 0$) and have been compared to neighbouring nuclei in Table 6.1, where the Q_λ values are calculated from $\langle 0^+ || E\lambda || \lambda^{(-1)^\lambda} \rangle$ in each case. These parameters do not differentiate between dynamic and static collectivity and therefore, supplementary information is required to distinguish these modes. A representation of the surfaces of the two nuclei of interest have been drawn according to Equation 1.2 in Figure 6.2.

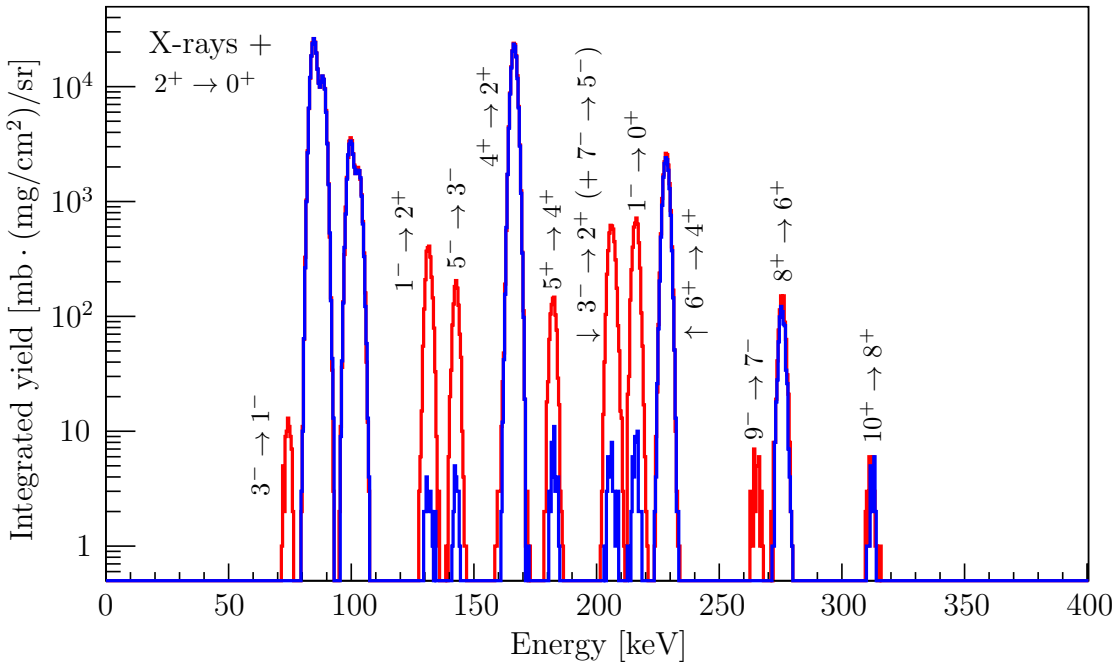

Figure 6.1: Comparison of simulated γ-ray yields in ^{224}Ra, experiment 2 (see Table 5.1), calculated using the measured matrix elements from Table 5.6 (red) and those same matrix elements, but with all $E3$ matrix elements equal to 0 efm^3 (blue).

6.1 Interpretation of Collectivity

Collective odd-spin negative-parity states can be either vibrational or rotational in nature. The former produces I^- states via the coupling of an octupole phonon to $(I-3)^+$ rotational states while the latter arise due to the rotation of an reflection-asymmetric charge distribution. For octupole-vibrations it is expected that all $E3$ matrix elements between states other than those coupled via an octupole phonon, i.e. $\langle (I-3)^+ || E3 || I^- \rangle$, vanish.

Information is available in part for ^{224}Ra, specifically the measurements of $\langle 2^+ || E3 || 1^- \rangle$ and $\langle 2^+ || E3 || 3^- \rangle$, which are both consistent with the rigid-rotor prediction, however, there is no sensitivity in either nucleus to matrix elements such as $\langle 1^- || E3 || 4^+ \rangle$ and $\langle 3^- || E3 || 6^+ \rangle$. This would require a much larger number of (Z, θ) combinations, or the observation of an $E3$-decay branch, which is unreasonable due to the negligible probability compared to $E1$ or $E2$ decay.

Table 6.1: Multipole moments, Q_λ, and deformation parameters, β_λ, in ^{220}Rn and ^{224}Ra, determined from this analysis. For comparison, values in neighbouring nuclei measured via Coulomb excitation are also included along with their references.

Nucleus	Q_2 [efm^2]	Q_3 [efm^3]	β_2	β_3	β_4	Refs.
^{208}Pb	179 ± 4	2100 ± 20	0.048	0.102	0.067	[100, 101]
^{220}Rn	434 ± 14	2180 ± 30	0.119	0.095	0.002[a]	—
^{224}Ra	632 ± 10	2520 ± 90	0.154	0.097	0.080[a]	—
^{226}Ra	717 ± 3	2890 ± 80	0.165	0.104	0.123	[3]
^{230}Th	900 ± 6	2140 ± 100	0.202	0.074	0.114	[98, 102]
^{232}Th	962 ± 5	1970 ± 100	0.211	0.070	0.192	[99, 103]
^{234}U	1047 ± 5	2060 ± 120	0.220	0.067	0.138	[98, 102]

a) Value of β_4 is taken from Ref. [13] and normalised to the measurement of ^{226}Ra.

Looking to the behaviour of the energy levels, specifically the relative alignment of the negative-parity states to the positive-parity rotational band it is possible to characterise the structure of the nucleus as a function of spin [22]. The energy displacement can be defined as

$$\delta E(I) = E(I^-) - \frac{1}{2}\left[E\left((I+1)^+\right) + E\left((I-1)^+\right)\right]. \tag{6.1}$$

In the limit of stable octupole deformation δE tends towards zero while the ratio of the rotational frequencies of the positive- and negative-parity bands becomes unity. At increasing spin, however, the sphericity driving pairing force is weakened by the Coriolis force allowing for a stabilisation of odd-even staggering for states coupled by an octupole phonon. To distinguish between this case and static octupole deformation, one needs to look to the relative alignment of the positive- and negative-parity bands, Δi_x. Alignment of an octupole phonon with the even-spin rotational band would give $\Delta i_x = 3\hbar$, whereas if the positive- and negative-parity states are part of the same rotational band, then the relative alignment will be zero.

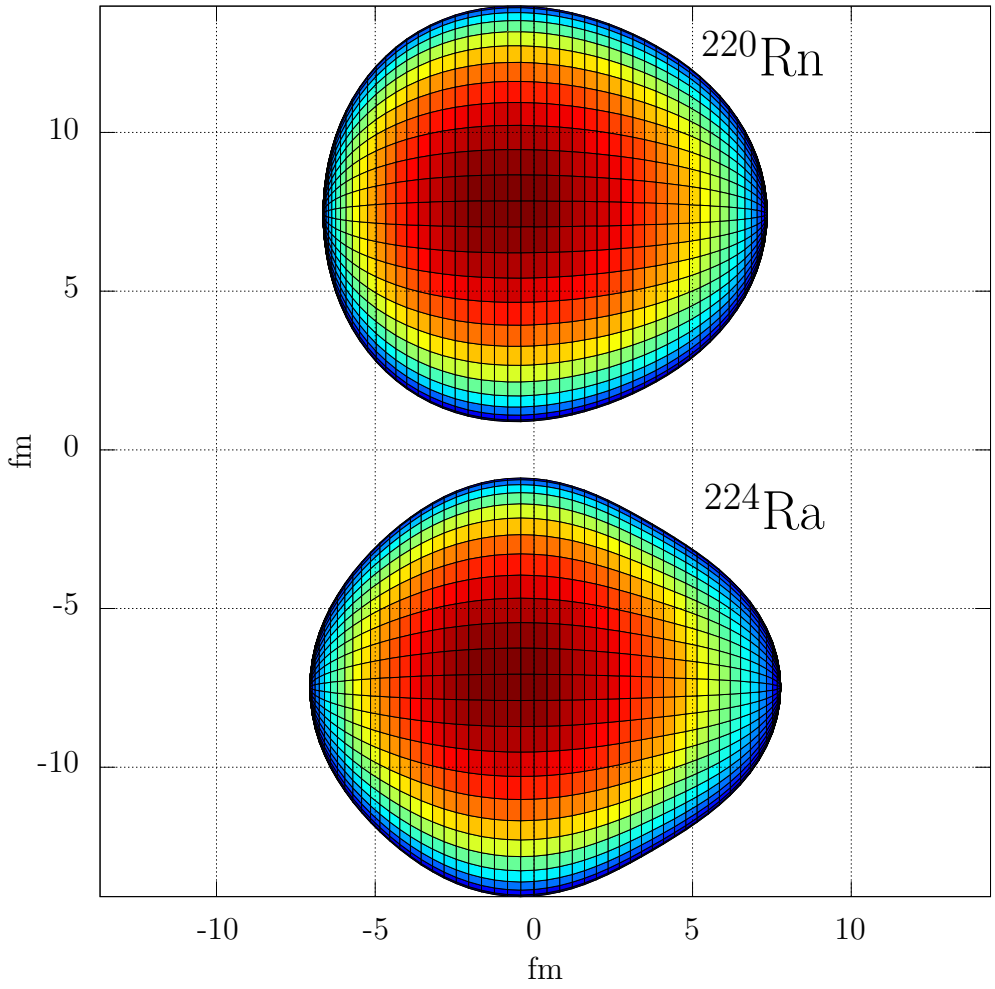

Figure 6.2: Representation of the nuclear surfaces of ^{220}Rn (top) and ^{224}Ra (bottom)

6.1.1 ^{220}Rn

At high angular momentum, $I \geq 10$, in the even-mass radon isotopes with $218 \leq A \leq 222$, the behaviour of δE (shown in Figure 6.3) is much like that of an octupole-rotor [104]. This behaviour can be attributed to a weakening of the pairing force as explained in Section 6.1, however, at low spin significant deviations are observed in δE indicating its low-spin vibrational structure. The relative alignment, Δi_x, for these nuclei are plotted in Figure 12 of Reference [104]. Each is consistent with the alignment of an octupole phonon across the range of rotational frequencies.

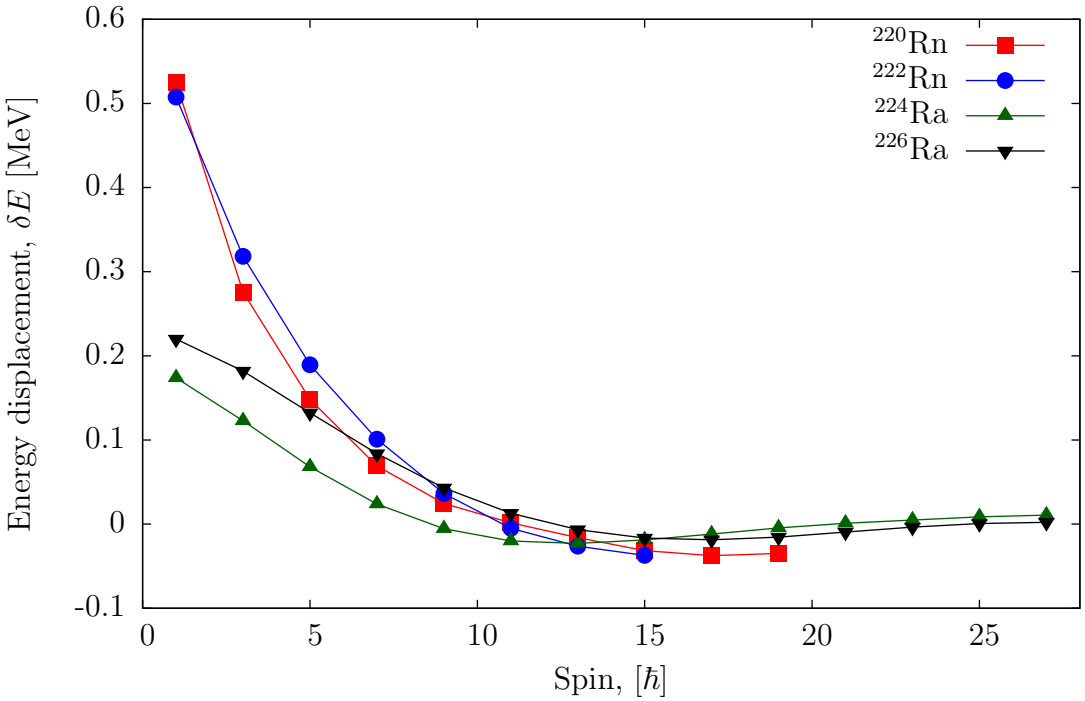

Figure 6.3: The energy displacement as a function of spin, $\delta E(I)$, between postive- and negative-parity states shown for isotopes of Rn and Ra.

This is collated with the measurement in this thesis to reinforce the assignment of the negative-parity states in ^{220}Rn as an octupole phonon coupled to the even-spin rotational band. The Q_3 in particular is similar to that in ^{230}Th and indeed ^{232}Th, which can both be interpreted in terms of octupole vibrations [105] although the intrinsic quadrupole moment varies significantly. The behaviour of the octupole 3^- states in these nuclei are proposed to be similar due to the high excitation energy and comparable electric-octupole moments, however, comparison of β_3 suggests that ^{220}Rn is likely to have a greater degree of octupole softness. Nevertheless, the mutual dependence of β_3 on the quadrupole deformation, β_2, cannot be ignored. As Figure 6.2 illustrates, the instantaneous surface shape at $(\beta_2, \beta_3, \beta_4)$ does not represent an enhanced pear-shape when compared to ^{224}Ra, even though the octupole deformation is similar.

As can be seen in Table 6.1, β_3 alone can be misleading since it does not account

for the differences between dynamic and static deformation. For example, ^{208}Pb is a doubly-magic nucleus, which is spherical in the ground state and its first excited 3^- state is of a vibrational nature. The β_3 is pronounced, and comparable to that of the octupole-deformed nucleus ^{226}Ra, yet there is no suggestion of a ground state deformation. The softness to the octupole degree of freedom, via a vibrational mode, may appear large, though the excitation energy of the 3^- state (2.6 MeV) rules out strong octupole correlations in the ground state.

6.1.2 ^{224}Ra

Considering the energy displacement, δE, plotted in Figure 6.3, ^{224}Ra approaches the limit of stable octupole deformation at $\sim 8\hbar$. At lower spin the deviation from this limit is much less significant than in the radon isotopes. The relative alignment of the positive- and negative-parity bands in ^{224}Ra, and indeed ^{222,226}Ra, (plotted in Figure 13 of Reference [104]), is less than $3\hbar$ for the whole range of rotational frequencies measured and drops to zero as the rotational frequency increases, showing a stabilisation of the deformation. The electric-octupole moment, Q_3, measured in this thesis is consistent with an enhancement of the octupole deformation. Although it remains $\simeq 13\%$ smaller than in ^{226}Ra, the level energy arguments coupled with this enhancement supports the interpretation of static octupole deformation in these nuclei.

The variation of the octupole deformation parameter, β_3, is smaller ($\simeq 8\%$ to ^{226}Ra and even less to ^{220}Rn), however, the interpretation of this parameter requires more careful consideration, such as the effect of the quadrupole deformation, β_2, and whether the deformation is dynamic or static. The role of this quadrupole-octupole coupling in the deformation is apparent in Figure 6.2. Although the β_3 in ^{224}Ra is similar to that in ^{220}Rn, the larger quadrupole deformation, β_2, enhances the reflection-asymmetric pear shape to a greater degree.

6.2 Theoretical Predictions

One of the first theoretical suggestions that nuclei can become stable about a non-zero equilibrium value of octupole deformation came from a microscopic-macroscopic interpretation [11]. Since then, self-consistent mean-field theory has advanced and predicted stable octupole minima in many nuclei while the electric-octupole moments are alternatively interpreted in the cluster-model approach.

6.2.1 Mean-field approach

Self-consistent mean-field Hartree-Fock-Bogoliubov (HF-Bogoliubov or HFB) calculations utilising the Skyrme SIII interaction [106] in ^{222}Ra were the first such calculations to predict a deformed minima with $Q_3 \neq 0$ in the actinide region. Calculations using the HF+BCS method and the Gogny interaction [107, 108] have been used to obtain the excitation energy of 1^- states in Ra isotopes along with $B(E1; 1^- \rightarrow 0^+)$ and $B(E3; 3^- \rightarrow 0^+)$ values and appear to have some success.

An extensive review of octupole excitations was performed more recently by Robledo and Bertsch [109] where they predict the $B(E3)$ values with several variants of the Gogny interaction in the HFB mean-field theory on a global level. Presented in Figure 6.4 are some of these predictions using the Gogny interaction for the isotopic chains of Rn and Ra nuclei around $N \sim 134$. Discrepancies are apparent between the two different parameterisations showing improvement in the calculations is necessary. The trend in the Ra isotopes suggests a peak at $A = 224$, which is not observed since the measured $B(E3; 3^- \rightarrow 0^+)$ for ^{224}Ra of 42(3) W.u. in this work is smaller than the 54(3) W.u. in ^{226}Ra.

The small dipole moments in ^{224}Ra have been explained as a cancellation of the microscopic shell effects and the collective $E1$ moment. It has been shown, in the radium isotopes in particular, that this balance is maximised around $A = 224$ with shell effects becoming more dominant in heavier nuclei where larger negative dipole

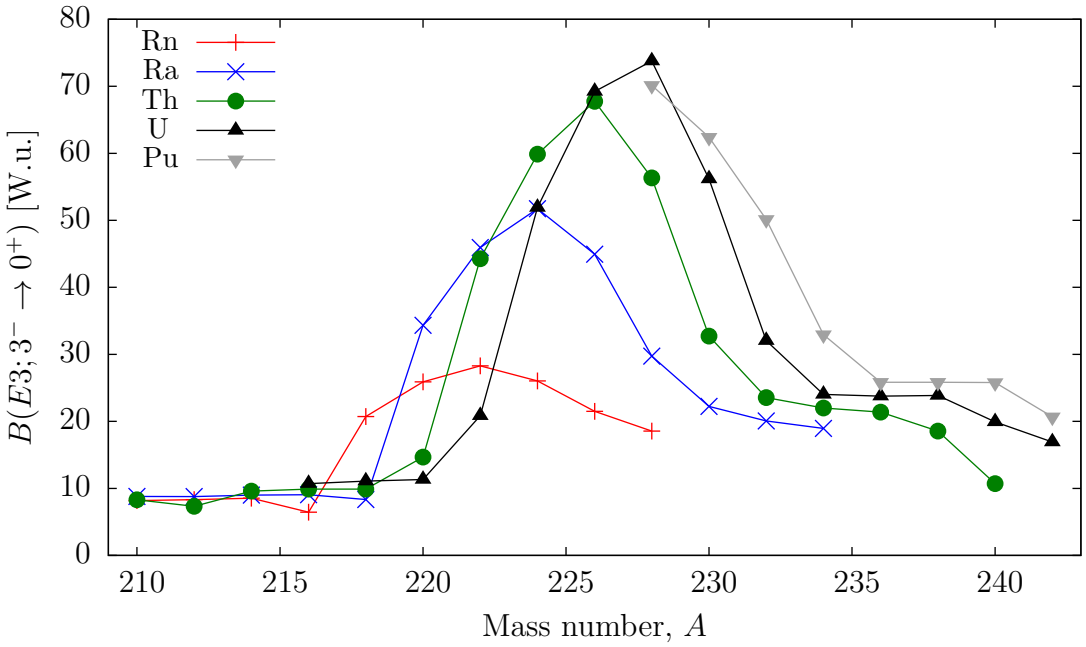

Figure 6.4: Systematics of $B(E3)$ values in even-even nuclei using the generator-coordinate extension (GCM) of the Hartree-Fock-Bogoliubov (HFB) self-consistent mean field theory with the D1M parameterisation of the Gogny force.

moments are expected [110]. Importantly, the experimentally observed trends in $B(E1; 1^- \rightarrow 0^+)$, nonetheless insensitive to the sign, can be reproduced within the mean-field approach using the Gogny force [111].

6.2.2 Cluster models

Buck et al. [112] used a cluster model with an effective charge or an amputated wave function to reproduce the $E2$ and $E3$ matrix elements in ^{226}Ra obtained by Wollersheim et al. [3]. Using a Pb-core and a ^{14}C cluster, the model fits well to the measured $E2$, $E3$ and $E4$ moments, but not to the $E1$ moments. The same thing is apparent in the other isotopes for which calculations were performed, ^{222,224}Ra, and isn't fully overcome. The authors suggest that a pure cluster-core picture is perhaps too idealistic and nucleon transfer between the core and cluster, or a superposition of different cluster-core combinations, would "smear-out" the effective charge to mass

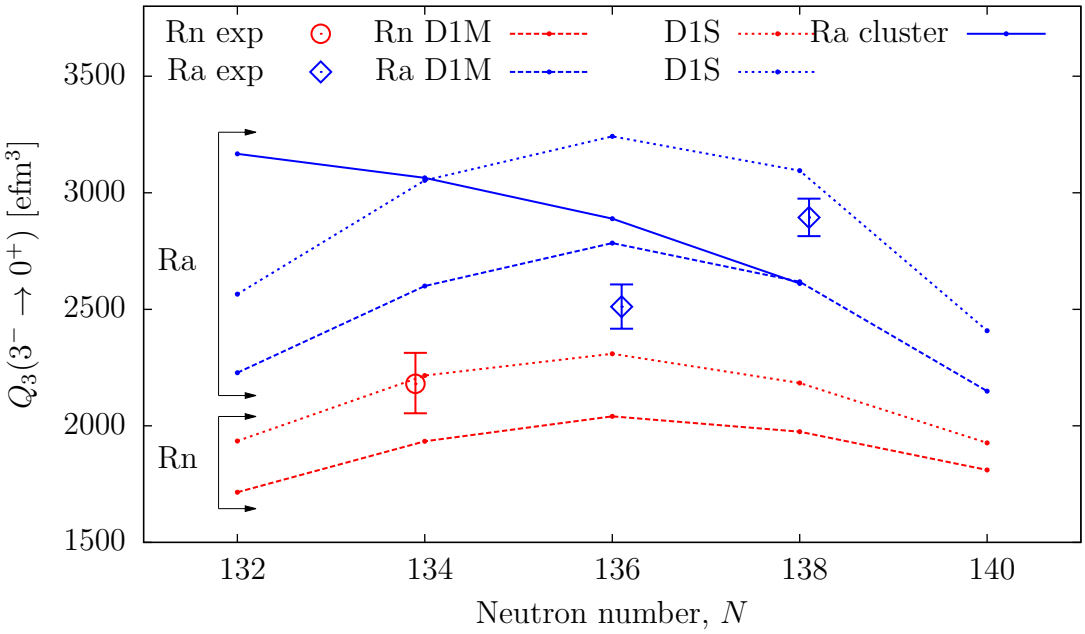

Figure 6.5: Comparison of experimental $Q_3(3^- \rightarrow 0^+)$ from Table 6.1 for Rn($Z = 86$) and Ra($Z = 88$), with predictions from two different models overlaid. The solid lines join the cluster model predictions of Shneidman et. al [113]. The dashed lines connect points predicted by the mean-field calculations using the generator-coordinate extension (GCM) of the HFB theory with Gogny forces by Robledo and Bertsch [109]. Two parameterisations are compared, D1M and D1S.

ratio of the two bodies. The $E1$ operator is sensitive to this effect but there is no method of calculating these effects within this model.

A more recent cluster model [113] also fails to reproduce the small D_0, but does predict $Q_{30}(3^- \rightarrow 0^+) = 2889$ efm^3 to reasonable agreement with the measurement presented in this thesis (2520 ± 90 efm^3). The values for the radium (and thorium) isotopic chain(s), however, indicate an increase in the electric-octupole moment with decreasing mass number, a trend bucked by the experimental data (see Figure 6.5).

6.3 Summary

For the first time, the $B(E3; 3^- \rightarrow 0^+)$ value has been determined in radioactive actinide nuclei (with the exception of the long-lived ^{226}Ra) at the same time as

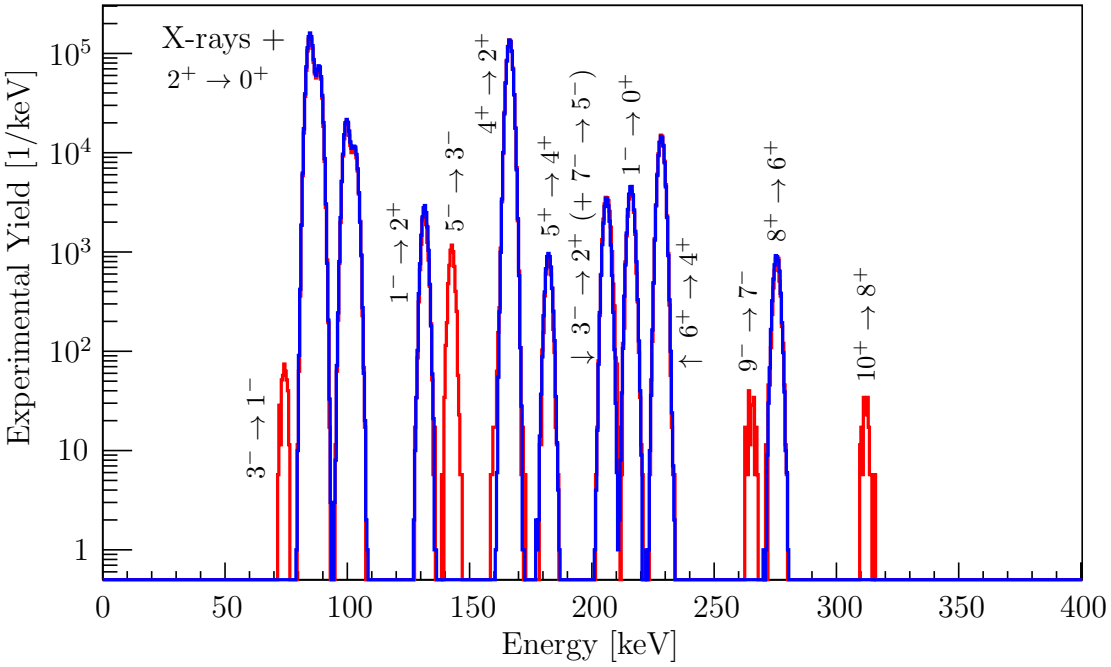

Figure 6.6: Comparison of simulated γ-ray yields in ^{224}Ra, experiment 2 (see Table 5.1), calculated using the measured matrix elements from Table 5.6 (red) and the measured experimental yields from Table B.2 (blue). The $5^+ \rightarrow 4^+$ transition is unobserved experimentally due to the large Compton background. The simulated yields are normalised to the $4^+ \rightarrow 2^+$ transition.

demonstrating the ability to measure $E3$ matrix elements to less than 10% precision with Radioactive Ion Beams (RIBs).

The GOSIA analysis relies on the simulation and comparison of γ-ray yields following Coulomb excitation to fit the electromagnetic matrix elements connecting excited states in the nucleus. Figure 6.6 shows the comparison of the simulated γ-ray spectrum using the final results in ^{224}Ra and the experimentally observed yields. The comparison is remarkable, demonstrating that the process is well defined and that the fitted matrix elements are reliable.

It has been shown that the electric-octupole moments, Q_3, are enhanced as expected for nuclei exhibiting octupole collectivity, however, there is not sufficient information from the experiment here alone to interpret fully the mode of this collectivity, be it dynamic vibrations or static deformation. Previous interpretations of ^{220}Rn as an octupole-vibrational nucleus and ^{224}Ra as octupole-deformed are drawn

on and the new measurements are used to support these suggestions. Comparisons to theoretical mean-field approaches and cluster models are also made. While there is some success in both, the most well matched predictions come from the GCM extension of the Hartree-Fock-Bogoliubov theory [109]. The predicted trend of $Q_3(3^- \rightarrow 0^+)$ values, plotted in Figure 6.5, do not reproduce experimental observations, although more data along the isotopic chains of Rn and Ra are required. What is apparent is the deviation of the cluster model from the experimental values as mass number decreases.

6.3.1 Electric-Dipole Moment (EDM)

The search for a permanent electric-dipole moment in atoms has gained momentum in heavy odd-mass reflection-asymmetric nuclei [114, 115]. This is because of an enhancement of the nuclear-Schiff moment [116] when parity doublets, observed in odd-mass radium and thorium isotopes around $N \sim 137$, become almost degenerate, i.e. the energy difference $|E(I^-) - E(I^+)|$ is minimised [117]. The Schiff moment is also dependent on the strength of the interaction between the states forming the parity doublet, something which has the potential and is proposed [118, 119] to be measured in a similar way to the even isotopes studied in this thesis. Thus, a large $E3$ matrix element coupling the degenerate states will also enhance the Schiff moment and since this induces the atomic EDM, the sensitivity over non-octupole systems such as ^{199}Hg can be improved by a factor of 100-1000 [120].

Strong quadrupole-octupole deformation is a requirement to observe such enhancements in the nuclear-Schiff moment [114]. A weakening of the quadrupole-octupole collectivity in radon isotopes, observed in this thesis for ^{220}Rn, coupled with the requirement of near-degenerate parity doublets, so far unobserved in the proposed candidates ^{221,223}Rn [114], may disfavour their candidacy for atomic EDM measurements. The radium isotopes, however do exhibit strong potentially static

reflection-asymmetry, while the observed parity splitting in ^{225}Ra is just 55 keV and is therefore a strong candidate for the atomic EDM search [115, 121, 122].

6.4 Outlook

To constrain the nuclear models making predictions of octupole collectivity, a single data point is not sufficient. This is proven with the calculations of the radium isotopic-chain where the peak $B(E3; 3^- \rightarrow 0^+)$ is expected at $A = 224$, but has now been shown not to be the case with the new measurements in this thesis. Extending the measurements to further Ra isotopes will clarify the appropriateness of the models discussed and provide new input to refine such models. Specifically the already proposed ^{222}Ra [123] plus ^{228}Ra should be studied to determine the experimental trend of $B(E3)$ values.

It is also feasible, and proposed [123], to measure 222Rn and extend the knowledge of the radon isotopes, especially since there is so far only one data point, that of ^{220}Rn from this thesis. The strongest octupole correlations are predicted by the HFB calculation to be in the uranium isotopes, specifically $^{226-230}$U, a region already known to exhibit octupole behaviour [124], where the $B(E3; 3^- \rightarrow 0^-)$ values are calculated to be $\sim$ 70 W.u. [125]. Studying $E3$ transitions in these nuclei requires major advancements in RIB technology and may be possible at the yet-to-be-completed FRIB facility at Michigan State University, US [126].

Extending the current measurements to odd-mass nuclei [118, 119] is key for input to the EDM search. The first part of this experimental campaign has already been performed with Coulomb excitation of ^{221}Rn at REX-ISOLDE [127] and γ-ray transitions have been observed for the first time in this nucleus. A proposal to extend the study of octupole collectivity at REX-ISOLDE to the region around $Z \sim 56$ and $N \sim 88$, utilising the principles of the current work, has been accepted [128].

Appendices

Appendix A

Kinematic approximations

Presented below are a set of approximations used to calculate the kinematics of the scattering process in Coulomb excitation. Since the experiment was inverse kinematics, calculating the laboratory angles of the collision partners was more difficult and assumptions and simplifications had to be used. Below is a list of parameters consistently used in the following equations:

A_P Mass of the scattered projectile nucleus $[u]$

A_T Mass of the recoiling target nucleus $[u]$

E_b Incoming beam energy [A.MeV]

$E_{P,T}$ Energy of the scattered projectile/target nucleus after exit from the target [MeV]

Q_{CE} The Q-value of the reaction, or the excitation energy of the nucleus [MeV]

$\tau = A_P/A_T$; $\tau_p = A_P/A_T$

$\theta_{P,T}$ Scattering angle in the laboratory frame for the projectile/target

E^P_loss Energy loss of the projectile at incident energy, E_b, in the target material [MeV/(cm^2)]

$\overline{E^{P,T}_\mathrm{loss}}$ Average energy loss of the projectile/target in the target material [MeV/(cm^2)]

Projectile energy

It is assumed that the target nuclei is at rest before the collision and so the centre of mass energy is equal to that of the incoming projectile energy. An approximation of the Q-value had to be used, however, in sub-barrier Coulomb excitation, this is usually quite small and in this case is less than 1% of the centre of mass energy. Energy loss through the target also had to be approximated, since the exact interaction point within a target of thickness t (MeV/(cm^2)), is not known. Here, an additional parameter, d or depth, is introduced to allow a certain amount of optimisation of the overall Doppler correction, however, this is an arbitrary solution since the true depth cannot be ascertained.

In the case where the projectile is identified in the CD detector, it is possible to use the measured energy directly. However, since the experiments in this thesis rely on the detection of a target recoil, it is necessary to calculate the projectile energy from the measured recoil energy, E_T:

$$E_P = A_P \cdot E_\mathrm{b} - dt \cdot \overline{E^P_\mathrm{loss}} - (1-d)\, t \cdot \cos(\theta_P) \cdot \overline{E^T_\mathrm{loss}} - E_T. \tag{A.1}$$

Of course, the energy loss is dependent on the energy of the beam, but for the purposes of simplifying the calculations, and average is calculated using SRIM [79] with the assumption that an average beam energy can be represented as $\overline{E_P} = E_P - 0.5t \cdot E^P_\mathrm{loss}$. For the purposes of calculating the average recoil energy loss, $\overline{E^T_\mathrm{loss}}$, a neutral beam of target species nuclei are assumed to pass through the target material with an average energy of $\overline{E_T} = 0.5\overline{E_P}$.

Appendix B

Experimental Yields

This Appendix tabulates the experimental yields from the experiments performed in this thesis. All intensities presented are efficiency corrected and their uncertainties include errors from background subtraction and efficiency correction, added quadratically to the statistically uncertainty.

Table B.1: Efficiency corrected, γ-ray yields in ^{220}Rn for each observed transition in the experiments tabulated in Table 5.1 plus the "total statistics", p-γ data.

Experiment No.	Transition	Energy [keV]	Intensity	Error
1	$2^+ \rightarrow 0^+$	241.0	2828	109
	$4^+ \rightarrow 2^+$	292.7	354	25
2	$2^+ \rightarrow 0^+$	241.0	4281	157
	$4^+ \rightarrow 2^+$	292.7	321	25

Table B.1: – Continued

Experiment No.	Transition	Energy [keV]	Intensity	Error
3	$2^+ \rightarrow 0^+$	241.0	42883	1427
	$4^+ \rightarrow 2^+$	292.7	5193	185
	$5^- \rightarrow 4^+$	318.2	85	16
	$6^+ \rightarrow 4^+$	340.2	338	27
	$3^- \rightarrow 2^+$	422.0	123	18
	$1^- \rightarrow 0^+$	645.4	70	15
	$2^+_\gamma \rightarrow 2^+$	696.9	236	26
	$2^+_\gamma \rightarrow 0^+$	937.8	73	21
4	$2^+ \rightarrow 0^+$	241.0	66178	2194
	$4^+ \rightarrow 2^+$	292.7	5359	191
	$5^- \rightarrow 4^+$	318.2	118	22
	$6^+ \rightarrow 4^+$	340.2	202	25
	$3^- \rightarrow 2^+$	422.0	213	25
	$1^- \rightarrow 0^+$	645.4	78	17
	$2^+_\gamma \rightarrow 2^+$	696.9	213	24
	$2^+_\gamma \rightarrow 0^+$	937.8	75	27
5	$2^+ \rightarrow 0^+$	241.0	19546	660
	$4^+ \rightarrow 2^+$	292.7	1053	50
	$6^+ \rightarrow 4^+$	340.2	25	13
	$3^- \rightarrow 2^+$	422.0	94	14
	$2^+_\gamma \rightarrow 2^+$	696.9	40	12

Table B.1: – Continued

Experiment No.	Transition	Energy [keV]	Intensity	Error
6	$2^+ \rightarrow 0^+$	241.0	22565	760
	$4^+ \rightarrow 2^+$	292.7	774	41
	$6^+ \rightarrow 4^+$	340.2	18	10
	$3^- \rightarrow 2^+$	422.0	122	15
	$2^+_\gamma \rightarrow 2^+$	696.9	78	18
p-γ	$2^+ \rightarrow 0^+$	241.0	589000	19000
	$4^+ \rightarrow 2^+$	292.7	45800	1500
	$5^- \rightarrow 4^+$	318.2	800	70
	$6^+ \rightarrow 4^+$	340.2	2330	110
	$1^- \rightarrow 2^+$	404.2	140	60
	$3^- \rightarrow 2^+$	422.0	1900	100
	$1^- \rightarrow 0^+$	645.4	540	60
	$2^+_\gamma \rightarrow 2^+$	696.9	1940	110
	$2^+_\gamma \rightarrow 0^+$	937.8	920	80
	unplaced	836(2)	300	60

Table B.2: Efficiency corrected, γ-ray yields in ^{224}Ra for each observed transition in the experiments tabulated in Table 5.1 plus the "total statistics", p-γ data. Note that the 205.9 keV and 207.7 keV transitions are part of an unresolved doublet.

Experiment No.	Transition	Energy [keV]	Intensity	Error
1	$2^+ \rightarrow 0^+$	84.4	2773	293
	$1^- \rightarrow 2^+$	131.6	142	34
	$4^+ \rightarrow 2^+$	166.4	6914	207
	$5^- \rightarrow 4^+$	182.3	67	22
	$3^- \rightarrow 2^+$	205.9	177	24
	$7^- \rightarrow 5^-$	207.6		
	$1^- \rightarrow 0^+$	216.0	213	23
	$6^+ \rightarrow 4^+$	228.5	1397	68
	$8^+ \rightarrow 6^+$	275.7	125	27
2	$2^+ \rightarrow 0^+$	84.4	4351	449
	$1^- \rightarrow 2^+$	131.6	120	48
	$4^+ \rightarrow 2^+$	166.4	5695	177
	$5^- \rightarrow 4^+$	182.3	41	18
	$3^- \rightarrow 2^+$	205.9	150	25
	$7^- \rightarrow 5^-$	207.6		
	$1^- \rightarrow 0^+$	216.0	198	24
	$6^+ \rightarrow 4^+$	228.5	639	45
	$8^+ \rightarrow 6^+$	275.7	42	30

Table B.2: – Continued

Experiment No.	Transition	Energy [keV]	Intensity	Error
3	$2^+ \rightarrow 0^+$	84.4	869	133
	$1^- \rightarrow 2^+$	131.6	59	17
	$4^+ \rightarrow 2^+$	166.4	2443	85
	$3^- \rightarrow 2^+$	205.9	59	17
	$7^- \rightarrow 5^-$	207.6		
	$1^- \rightarrow 0^+$	216.0	73	13
	$6^+ \rightarrow 4^+$	228.5	549	34
	$8^+ \rightarrow 6^+$	275.7	52	17
4	$2^+ \rightarrow 0^+$	84.4	1231	176
	$1^- \rightarrow 2^+$	131.6	58	18
	$4^+ \rightarrow 2^+$	166.4	2074	75
	$5^- \rightarrow 4^+$	182.3	39	11
	$3^- \rightarrow 2^+$	205.9	62	19
	$7^- \rightarrow 5^-$	207.6		
	$1^- \rightarrow 0^+$	216.0	52	11
	$6^+ \rightarrow 4^+$	228.5	269	25
	$8^+ \rightarrow 6^+$	275.7	30	22

Table B.2: – Continued

Experiment No.	Transition	Energy [keV]	Intensity	Error
5	$2^+ \rightarrow 0^+$	84.4	5002	440
	$1^- \rightarrow 2^+$	131.6	179	35
	$5^- \rightarrow 3^-$	142.0	58	24
	$4^+ \rightarrow 2^+$	166.4	6014	185
	$5^- \rightarrow 4^+$	182.3	34	13
	$3^- \rightarrow 2^+$	205.9	289	27
	$7^- \rightarrow 5^-$	207.6		
	$1^- \rightarrow 0^+$	216.0	332	26
	$6^+ \rightarrow 4^+$	228.5	556	35
	$8^+ \rightarrow 6^+$	275.7	34	19
	$2^+_\gamma \rightarrow 2^+$	881.1	29	9
6	$2^+ \rightarrow 0^+$	84.4	6789	596
	$1^- \rightarrow 2^+$	131.6	98	40
	$4^+ \rightarrow 2^+$	166.4	4537	147
	$5^- \rightarrow 4^+$	182.3	27	30
	$3^- \rightarrow 2^+$	205.9	314	31
	$7^- \rightarrow 5^-$	207.6		
	$1^- \rightarrow 0^+$	216.0	199	25
	$6^+ \rightarrow 4^+$	228.5	234	26

Table B.2: – Continued

Experiment No.	Transition	Energy [keV]	Intensity	Error
p-γ	$2^+ \rightarrow 0^+$	84.4	53000	3000
	$1^- \rightarrow 2^+$	131.6	1460	130
	$5^- \rightarrow 3^-$	142.0	440	100
	$4^+ \rightarrow 2^+$	166.4	81500	1900
	$5^- \rightarrow 4^+$	182.3	780	90
	$3^- \rightarrow 2^+$	205.9	2490	170
	$7^- \rightarrow 5^-$	207.6	380	150
	$1^- \rightarrow 0^+$	216.0	3030	120
	$6^+ \rightarrow 4^+$	228.5	13600	400
	$9^- \rightarrow 7^-$	265.3	180	60
	$8^+ \rightarrow 6^+$	275.7	1260	90
	$10^+ \rightarrow 8^+$	312.6	90	50
	$2^+_\gamma \rightarrow 2^+$	881.1	410	80
	$2^+_\gamma \rightarrow 0^+$	965.5	360	90

Bibliography

[1] P. A. Butler and W. Nazarewicz, Rev. Mod. Phys. **68**, 349 (1996). 1, 11

[2] P. Möller and J. Nix, Nuclear Physics A **361**, 117 (1981). 1, 11

[3] H. J. Wollersheim et al., Nuclear Physics A **556**, 261 (1993). 2, 4, 11, 60, 72, 73, 78, 82, 87

[4] T. Czosnyka, D. Cline, and C. Y. Wu, Bull. Am. Phys. Soc. **28** (1983). 2, 19

[5] G. A. Leander and Y. S. Chen, Phys. Rev. C **37**, 2744 (1988). 3

[6] A. Bohr and B. Mottelson, *Nuclear Structure: Nuclear deformations*, Nuclear Structure, W. A. Benjamin, 1969. 4, 52

[7] F. Asaro, F. Stephens, and I. Perlman, Phys. Rev. **92**, 1495 (1953). 6, 55

[8] F. Stephens, F. Asaro, and I. Perlman, Phys. Rev. **96**, 1568 (1954). 6

[9] F. S. Stephens, F. Asaro, and I. Perlman, Phys. Rev. **100**, 1543 (1955). 6

[10] R. Chasman, Physics Letters B **96**, 7 (1980). 6, 8

[11] A. Gyurkovich, A. Sobiczewski, B. Nerlo-Pomorska, and K. Pomorski, Physics Letters B **105**, 95 (1981). 86

[12] G. Leander et al., Nuclear Physics A **388**, 452 (1982). 8, 11

[13] W. Nazarewicz et al., Nuclear Physics A **429**, 269 (1984). 6, 11, 73, 82

[14] I. Ahmad and P. A. Butler, Annual Review of Nuclear and Particle Science **43**, 71 (1993). 7

[15] P.D. Cottle and D.A. Bromley, Physics Letters B **182**, 129 (1986). 8

[16] R. K. Sheline, Physics Letters B **166**, 269 (1986). 8

[17] J. Fernández-Niello, H. Puchta, F. Riess, and W. Trautmann, Nuclear Physics A **391**, 221 (1982). 8

[18] D. Ward et al., Nuclear Physics A **406**, 591 (1983). 8

[19] J. F. Smith et al., Phys. Rev. Lett. **75**, 1050 (1995).

[20] J. F. C. Cocks et al., Phys. Rev. Lett. **78**, 2920 (1997). 8, 49, 55, 62

[21] W. Nazarewicz, G. Leander, and J. Dudek, Nuclear Physics A **467**, 437 (1987). 8

[22] W. Nazarewicz and P. Olanders, Nuclear Physics A **441**, 420 (1985). 8, 82

[23] R. W. Ibbotson et al., Nuclear Physics A **619**, 213 (1997). 8, 11, 60

[24] V. Strutinsky, Journal of Nuclear Energy (1954) **4**, 523 (1957). 8

[25] A. Bohr and B. R. Mottelson, Nuclear Physics **4**, 529 (1957). 8, 9
A. Bohr and B. R. Mottelson, Nuclear Physics **9**, 687 (1958-1959).

[26] P. A. Butler and W. Nazarewicz, Nuclear Physics A **533**, 249 (1991). 9

[27] G. Leander, W. Nazarewicz, G. Bertsch, and J. Dudek, Nuclear Physics A **453**, 58 (1986). 9

[28] R. J. Poynter et al., Physics Letters B **232**, 447 (1989). 9, 55

[29] M. Marten-Tölle et al., Zeitschrift für Physik A Hadrons and Nuclei **336**, 27 (1990). 9, 55

[30] T. Kibédi and R. H. Spear, Atomic Data and Nuclear Data Tables **80**, 35 (2002). 10

[31] R. Ibbotson et al., Phys. Rev. Lett. **71**, 1990 (1993). 11, 60

[32] G. Leander and R. Sheline, Nuclear Physics A **413**, 375 (1984). 11

[33] I. Ragnarsson, Physics Letters B **130**, 353 (1983). 11

[34] R. K. Sheline and G. A. Leander, Phys. Rev. Lett. **51**, 359 (1983). 11

[35] R. K. Sheline, A. K. Jain, and K. Jain, Phys. Rev. C **38**, 2952 (1988). 11

[36] R. J. Poynter et al., Journal of Physics G: Nuclear and Particle Physics **15**, 449 (1989). 11, 49

[37] I. Ahmad et al., Nuclear Physics A **576**, 246 (1994). 11

[38] R. K. Sheline and I. Ragnarsson, Phys. Rev. C **43**, 1476 (1991). 11
R. K. Sheline and I. Ragnarsson, Phys. Rev. C **44**, 2886 (1991).
M. Hussonnois, J. F. Le Du, L. Brillard, and G. Ardisson, Phys. Rev. C **44**, 2884 (1991).

[39] A. Sandulescu and W. Greiner, Reports on Progress in Physics **55**, 1423 (1992).

[40] M. Hussonnois and G. Ardisson, Zeitschrift für Physik A Hadrons and Nuclei **349**, 311 (1994). 11

[41] J. Pakarinen et al., In-beam electron spectroscopy at hie-isolde, Technical Report CERN-INTC-2010-040. INTC-I-107, CERN, Geneva, 2010. 12

[42] A. Wuosmaa, J. Schiffer, B. Back, C. Lister, and K. Rehm, Nuclear Instruments and Methods in Physics Research Section A: Accelerators, Spectrometers, Detectors and Associated Equipment **580**, 1290 (2007). 12

[43] S. J. Freeman et al., Letter of Intent to the ISOLDE and Neutron Time-of-Flight Experiments Committee for experiments with HIE-ISOLDE: A HELIcal Orbit Spectrometer (HELIOS) for HIE-ISOLDE, Technical Report CERN-INTC-2010-031. INTC-I-099, CERN, Geneva, 2010. 12

[44] K. Alder, A. Bohr, T. Huus, B. Mottelson, and A. Winther, Rev. Mod. Phys. **28**, 432 (1956). 13, 15

K. Alder, A. Bohr, T. Huus, B. Mottelson, and A. Winther, Rev. Mod. Phys. **30**, 353 (1958).

[45] L. Biedenharn and P. Brussaard, *Coulomb excitation*, Oxford library of the physical sciences, Clarendon Press, 1965. 18

[46] K. Alder and A. Winther, *Electromagnetic excitation: theory of Coulomb excitation with heavy ions*, North-Holland Pub. Co., 1975.

[47] D. Cline, Annual Review of Nuclear and Particle Science **36**, 683 (1986). 13, 51

[48] K. Alder and A. Winther, Mat. Fys. Medd. Dan. Vid. Selsk. **32**, 209 (1960). 18

[49] D. Cline et al., *Gosia User Manual for Simulation and Analysis of Coulomb Excitation Experiments*, Gosia Steering Committee, 2012. 18, 19, 60, 63, 64, 67

[50] A. Winther and J. de Boer, A Computer Program for Multiple Coulomb Excitation, in *Coulomb Excitation*, edited by K. Alder and A. Winther, Perspectives in Physics, pages 303–374, Academic Press Inc., 1966. 19

[51] A. E. Kavka, *Coulomb excitation: analytical methods and experimental results on even selenium nuclei*, PhD thesis, Uppsala University, Disciplinary Domain of Science and Technology, 1989. 21

[52] F. Bosch and H. Spehl, Zeitschrift für Physik A Hadrons and Nuclei **280**, 329 (1977). 21

[53] R. Brenn, H. Spehl, A. Weckherlin, H. A. Doubt, and G. van Middelkoop, Zeitschrift für Physik A Hadrons and Nuclei **281**, 219 (1977). 21

[54] E. Kugler, Hyperfine Interactions **129**, 23 (2000), 10.1023/A:1012603025802. 23

[55] L. Penescu, R. Catherall, J. Lettry, and T. Stora, Review of Scientific Instruments **81**, 02A906 (2010). 23

[56] T. Giles et al., Nuclear Instruments and Methods in Physics Research Section B: Beam Interactions with Materials and Atoms **204**, 497 (2003), 14th International Conference on Electromagnetic Isotope Separators and Techniques Related to their Applications. 23

[57] D. Habs et al., Nuclear Physics A **616**, 29 (1997). 25

[58] D. Habs et al., Nuclear Instruments and Methods in Physics Research Section B: Beam Interactions with Materials and Atoms **139**, 128 (1998).

[59] D. Habs et al., Hyperfine Interactions **129**, 43 (2000).

[60] O. Kester et al., Nuclear Instruments and Methods in Physics Research Section B: Beam Interactions with Materials and Atoms **204**, 20 (2003), 14th International Conference on Electromagnetic Isotope Separators and Techniques Related to their Applications. 27

[61] J. Cederkall et al., Nuclear Physics A **746**, 17 (2004), Proceedings of the Sixth International Conference on Radioactive Nuclear Beams (RNB6). 27

[62] D. Voulot et al., Nuclear Instruments and Methods in Physics Research Section B: Beam Interactions with Materials and Atoms **266**, 4103 (2008), Proceedings

of the XVth International Conference on Electromagnetic Isotope Separators and Techniques Related to their Applications.

[63] P. V. Duppen and K. Riisager, Journal of Physics G: Nuclear and Particle Physics **38**, 024005 (2011). 25

[64] F. Ames, J. Cederkäll, T. Sieber, and F. J. C. Wenander, *The REX-ISOLDE Facility: Design and Commissioning Report*, CERN, Geneva, 2005. 25, 26, 69

[65] F. Ames et al., Nuclear Instruments and Methods in Physics Research Section A: Accelerators, Spectrometers, Detectors and Associated Equipment **538**, 17 (2005). 26

[66] B. Wolf et al., Nuclear Instruments and Methods in Physics Research Section B: Beam Interactions with Materials and Atoms **204**, 428 (2003), ¡ce:title¿14th International Conference on Electromagnetic Isotope Separators and Techniques Related to their Applications¡/ce:title¿. 26

[67] F. Wenander, Nuclear Physics A **701**, 528 (2002), 5th International Conference on Radioactive Nuclear Beams.

[68] B. H. Wolf et al., Review of Scientific Instruments **73**, 682 (2002). 26

[69] A. Gustafsson, A. Herlert, and F. Wenander, Nuclear Instruments and Methods in Physics Research Section A: Accelerators, Spectrometers, Detectors and Associated Equipment **626–627**, 8 (2011). 27

[70] T. Sieber et al., Nuclear Physics A **701**, 656 (2002), 5th International Conference on Radioactive Nuclear Beams. 27

[71] J. Eberth et al., Progress in Particle and Nuclear Physics **46**, 389 (2001). 29, 30

[72] P. Reiter et al., Nuclear Physics A **701**, 209 (2002), 5th International Conference on Radioactive Nuclear Beams. 29

[73] Isolde web page [online]. 29

[74] J. Van De Walle et al., EPJ (2012). 30, 41, 43

[75] J. Tuli, Evaluated Nuclear Structure Data File (ENSDF), 2012, National Nuclear Data Center, Brookhaven National Laboratory. 31

[76] T. Williams and C. Kelley, Gnuplot v4.6, `http://www.gnuplot.info/`, 2012. 31

[77] I. Wiedenhöver, *Topfit*, Institut für Kernphysik der Universität zu Köln, 2008, `http://www.ikp.uni-koeln.de/misc/doc/tf_manual.ps`. 31

[78] D. Bazin, O. Tarasov, M. Lewitowicz, and O. Sorlin, Nuclear Instruments and Methods in Physics Research Section A: Accelerators, Spectrometers, Detectors and Associated Equipment **482**, 307 (2002). 37

[79] J. F. Ziegler, M. Ziegler, and J. Biersack, Nuclear Instruments and Methods in Physics Research Section B: Beam Interactions with Materials and Atoms **268**, 1818 (2010), 19th International Conference on Ion Beam Analysis. 37, 62, 94

[80] C. F. Liang, P. Paris, E. Ruchowska, and C. Briancon, Journal of Physics G: Nuclear and Particle Physics **15**, L31 (1989). 49, 51, 62

[81] D. G. Burke et al., Zeitschrift für Physik A Hadrons and Nuclei **333**, 131 (1989). 49

[82] R. J. Walen, Comptes Rendus **255**, 1604 (1962). 49

[83] W. Kurcewicz et al., Nuclear Physics A **289**, 1 (1977). 49, 55

[84] E. Browne and J. Tuli, Nuclear Data Sheets **112**, 1115 (2011). 49

[85] J. Gerl et al., Physics Letters B **120**, 83 (1983). 51, 52

[86] G. Alaga, K. Alder, A. Bohr, and B. Mottelson, K. Dan. Vidensk. Selsk. Mat.-Fys. Medd. **29** (1955). 52, 58

[87] W. Kurcewicz, E. Ruchowska, N. Kaffrell, T. Björnstad, and G. Nyman, Nuclear Physics A **356**, 15 (1981). 55, 56

[88] A. Artna-Cohen, Nuclear Data Sheets **80**, 227 (1997). 55, 58, 62

[89] R. B. Firestone, C. M. Baglin, and S. Chu, *Table of isotopes*, volume 4, Wiley, The University of Michigan, 8 edition, 1999. 55

[90] D. Cline, Nuclear Physics A **557**, 615 (1993). 60

[91] R. E. Bell, S. Bjornholm, and J. C. Severiens, Kgl. Danske Vid. Selsk. Mat.-Fys. Medd. **12**, 32 (1960). 62, 77

[92] W. R. Neal and H. W. Kraner, Phys. Rev. **137**, B1164 (1965). 62, 77

[93] H. Ton, W. Beens, S. Roodbergen, and J. Blok, Nuclear Physics A **155**, 235 (1970). 62

[94] G. Breit, R. L. Gluckstern, and J. E. Russell, Phys. Rev. **103**, 727 (1956). 65

[95] D. Cline and P. Lesser, Nuclear Instruments and Methods **82**, 291 (1970). 67

[96] P. Lesser, *Measurement of Static Electric Quadrupole Moments in* ^{56}Fe, ^{58}Ni *and* ^{60}Ni, PhD thesis, University of Rochester, Rochester, NY, US, 1971. 67

[97] N. Amzal et al., Nuclear Physics A **734**, 465 (2004). 68

[98] F. K. McGowan et al., Phys. Rev. C **10**, 1146 (1974). 77, 82

[99] F. McGowan and W. Milner, Nuclear Physics A **562**, 241 (1993). 77, 82

[100] D. Goutte et al., Phys. Rev. Lett. **45**, 1618 (1980). 82

[101] J. Heisenberg, J. Lichtenstadt, C. N. Papanicolas, and J. S. McCarthy, Phys. Rev. C **25**, 2292 (1982). 82

[102] C. E. Bemis et al., Phys. Rev. C **8**, 1466 (1973). 82

[103] C. Baktash and J. X. Saladin, Phys. Rev. C **10**, 1136 (1974). 82

[104] J. Cocks et al., Nuclear Physics A **645**, 61 (1999). 83, 85

[105] K. Neergård and P. Vogel, Nuclear Physics A **149**, 217 (1970). 84

[106] P. Bonche, P. Heenen, H. Flocard, and D. Vautherin, Physics Letters B **175**, 387 (1986). 86

[107] L. Robledo, J. Egido, J. Berger, and M. Girod, Physics Letters B **187**, 223 (1987). 86

[108] J. Egido and L. Robledo, Nuclear Physics A **524**, 65 (1991). 86

[109] L. M. Robledo and G. F. Bertsch, Phys. Rev. C **84**, 054302 (2011). 86, 88, 90

[110] J. Egido and L. Robledo, Nuclear Physics A **494**, 85 (1989). 87

[111] L. M. Robledo, M. Baldo, P. Schuck, and X. Viñas, Phys. Rev. C **81**, 034315 (2010). 87

[112] B. Buck, A. Merchant, and S. Perez, Nuclear Physics A **617**, 195 (1997). 87

[113] T. M. Shneidman, G. G. Adamian, N. V. Antonenko, R. V. Jolos, and W. Scheid, Phys. Rev. C **67**, 014313 (2003). 88

[114] N. Auerbach, Journal of Physics G: Nuclear and Particle Physics **35**, 014040 (2008). 90

[115] J. Ellis, J. Lee, and A. Pilaftsis, Journal of High Energy Physics **2011**, 1 (2011). 90, 91

[116] L. I. Schiff, Phys. Rev. **132**, 2194 (1963). 90

[117] J. Engel, J. L. Friar, and A. C. Hayes, Phys. Rev. C **61**, 035502 (2000). 90

[118] P. A. Butler et al., Measurements of octupole collectivity in odd-mass Rn and Ra nuclei using Coulomb excitation, Technical Report CERN-INTC-2011-008. INTC-P-244-ADD-1, CERN, Geneva, 2011. 90, 91

[119] P. A. Butler et al., Measurements of octupole collectivity in odd-mass Rn, Fr and Ra isotopes, Technical Report CERN-INTC-2010-022. INTC-I-091, CERN, Geneva, 2010. 90, 91

[120] M. V. Romalis, W. C. Griffith, J. P. Jacobs, and E. N. Fortson, Phys. Rev. Lett. **86**, 2505 (2001). 90

[121] J. Engel, M. Bender, J. Dobaczewski, J. H. d. Jesus, and P. Olbratowski, Phys. Rev. C **68**, 025501 (2003). 91

[122] J. Dobaczewski and J. Engel, Phys. Rev. Lett. **94**, 232502 (2005). 91

[123] P. A. Butler et al., Measurements of octupole collectivity in ^{220,222}Rn and ^{222,224}Ra using Coulomb excitation, Technical Report CERN-INTC-2008-021. INTC-P-244, CERN, Geneva, 2008. 91

[124] P. T. Greenlees et al., Journal of Physics G: Nuclear and Particle Physics **24**, L63 (1998). 91

[125] L. M. Robledo and R. R. Rodríguez-Guzmán, Journal of Physics G: Nuclear and Particle Physics **39**, 105103 (2012). 91

[126] FRIB [online]. 91

[127] G. G. O'Neill et al., To be published . 91

[128] M. Scheck et al., Determination of the $B(E3, 0^+ \rightarrow 3^-)$ strength in the octupole correlated nucleus ^{144}Ba using Coulomb excitation, Technical Report CERN-INTC-2011-039. INTC-P-305, CERN, Geneva, 2011. 91